12-3-2009

Nanoscopic Investigation of Surface Morphology of Neural Growth Cones and Indium Containing Group-III Nitrides

Göksel Durkaya
Georgia State University

NANOSCOPIC INVESTIGATION OF SURFACE MORPHOLOGY OF NEURAL GROWTH CONES AND INDIUM CONTAINING GROUP-III NITRIDES

by

GÖKSEL DURKAYA

Under the Direction of Nikolaus Dietz

ABSTRACT

This research focuses on the nanoscopic investigation of the three-dimensional surface morphology of the neural growth cones from the snail Helisoma trivolvis, and InN and InGaN semiconductor material systems using Atomic Force Microscopy (AFM). In the analysis of the growth cones, the results obtained from AFM experiments have been used to construct a 3D architecture model for filopodia. The filopodia from B5 and B19 neurons have exhibited different tapering mechanisms. The volumetric analysis has been used to estimate free Ca^{2+} concentration in the filopodium. The Phase Contrast Microscopy (PCM) images of the growth cones have been corrected to thickness provided by AFM in order to analyze the spatial refractive index variations in the growth cone. AFM experiments have been carried out on InN

and InGaN epilayers. Ternary InGaN alloys are promising for device applications tunable from ultraviolet (E_g^{GaN}=3.4 eV) to near-infrared (E_g^{InN}=0.7 eV). The real-time optical characteristics and ex-situ material properties of InGaN epilayers have been analyzed and compared to the surface morphological properties in order to investigate the relation between the growth conditions and overall physical properties. The effects of composition, group V/III molar ratio and temperature on the InGaN material characteristics have been studied and the growth of high quality indium-rich InGaN epilayers are demonstrated.

INDEX WORDS: Atomic force microscopy, Neuron, Growth cone, Filopodium, InN, InGaN

NANOSCOPIC INVESTIGATION OF SURFACE MORPHOLOGY OF NEURAL GROWTH CONES AND INDIUM CONTAINING GROUP-III NITRIDES

by

GÖKSEL DURKAYA

A Dissertation Submitted in Partial Fulfillment of the Requirements for the Degree of

Doctor of Philosophy

in the College of Arts and Sciences

Georgia State University

2010

NANOSCOPIC INVESTIGATION OF SURFACE MORPHOLOGY OF

NEURAL GROWTH CONES AND INDIUM CONTAINING GROUP-III NITRIDES

by

GÖKSEL DURKAYA

Committee Chair: Nikolaus Dietz

Committee: Vincent Rehder

Brian D. Thoms

A. G. Unil Perera

Vadym Apalkov

Douglas Gies

Electronic Version Approved:

Office of Graduate Studies

College of Arts and Sciences

Georgia State University

May 2010

To my wife, Meral

For her love, support and sacrifices …

ACKNOWLEDGMENTS

I would like to express my deepest gratitude to my advisor Professor Nikolaus Dietz. His expertise in academic research and academic writing was indispensible for the completion of this dissertation. It would not have been possible for me to achieve results in this challenging research topic without his guidance and insightful suggestions. He taught me how to execute the academic research from the approach to the interpretation and how to communicate the results with the scientific community to extend the knowledge in the field. I was extremely fortunate to have the privilege to work in his distinguished research group.

I owe special thanks to Professor Vincent Rehder for his continuous guidance and precious suggestions on the nanoscopic investigation of the neural growth cones. His expertise in Neuroscience has brought this research effort to a conclusion. I would also like to thank his research group for the productive collaboration. I would like to extend my special thanks to Professor Ian T. Ferguson and his research group at Georgia Institute of Technology for the productive collaboration. His contribution was an integral component in making up this dissertation.

I would like to thank other committee members, Professors A. G. Unil Perera, Brian Thoms, Douglas Gies, and Vadym Apalkov, for participating in the dissertation committee and providing helpful comments and suggestions.

Last but not least, I am grateful to the Molecular Basis of Disease program for the fellowship support and the access to the core research facility of the Biology department.

TABLE OF CONTENTS

LIST OF TABLES

LIST OF FIGURES

Chapter 1

1. Introduction to surface morphology analysis in material characterization

Nanoscopic investigation of surface morphological properties of materials is of crucial importance to explore the component parts and their relations to the macroscopic physical materials properties. In fact, the functional correlations between nano-scale and macro-scale properties may lead to nano-scale engineered materials with multi-functional properties.

This research focuses on the nanoscopic investigation of three-dimensional surface morphology of the neural growth cones from the snail Helisoma trivolvis, and InN and InGaN semiconductor systems using atomic force microscopy. The analysis methods are different for these material systems with different physical properties.

1.1 Surface morphological analysis of neural growth cones

Neurons are complex cellular structures specialized in intercellular communication throughout the nervous system. They are often very complex and polarized structures, receiving information from other neurons on their input side, the dendrites, and communicating with neurons at their often distant output regions, the axon terminal. The latter are typically located at the end of a long axon. During the development and the regeneration of the nervous system, the tips of axons and dendrites, often collectively called neurites, are tipped by highly motile sensory structures known as growth cones. These growth cones are responsible for the establishment of the correct connectivity in the nervous system and do so by surveying the environment and 'reading' local environmental guidance cues to locate an appropriate synaptic partner[1]. Function

and morphology of the growth cones are correlative; so, the shape and structure of the growth cones provide information about their functions.

The major cytoskeletal components of growth cones are microtubules and actin-filaments. There are three structural domains in a growth cone as classified by cytoskeletal organization and functionality (see Figure 1.1). The central domain (C-domain) is the thick, microtubule rich, central region containing organelles and transport vesicles. The transition zone (T-zone) is the transition region from axon microtubule bundles to a meshwork of filamentous actin. The peripheral zone (P-domain) is actin rich and the most dynamic domain of the growth cone. The P-domain contains the lamellipodium (veil), thin, sheet-like protrusions, and filopodia, fine, finger-like extensions, which are the most distal and the most dynamic components of the growth cone. The extension mechanism of growth cones is based on both filopodia and lamellipodia.

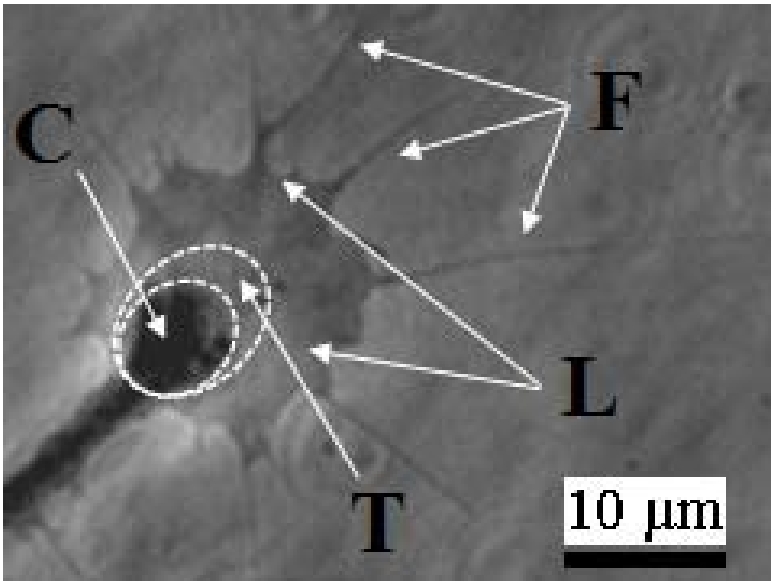

Figure 1.1 Structural domains of a growth cone. Letters C, T, F, and L stand for C-domain, T-zone, filopodium, and lamellipodium respectively.

In biological and biomedical research, microscopic analysis techniques are essential to study the static and the dynamic properties of complex systems. Earlier applications of microscopy in biological research concentrated on optical microscopy[2], while newer microscopic techniques include electron transmission/reflectance microscopy and atomic force microscopy variations[3]. Optical microscopy techniques enable the visualization of large biological structures such as cells and bacteria[4-6]. As a consequence of limitations introduced by optical diffraction, the study of morphological details smaller than 100 nm has not been possible, although contrast enhancement methods have been practiced[2,7]. In addition, the use of fluorescence microscopy has provided the capability of looking inside the cells and distinguishing individual intracellular structures at high spatial resolution[8]. None of these optical techniques are informative on the third dimension, as images obtained on 3-dimensional structures are compressed into 2-dimensions resulting in loss of information. The information on the third dimension, however, is absolutely necessary to elucidate the real-life characteristics of biological structures. Whereas confocal microscopy has closed the gap and provides 3-renderings of biological structures using fluorescent dyes, direct quantification of the nano-scale topography of structures in the third dimension is possible by Atomic Force Microscopy (AFM) [9].

A powerful tool to analyze the cytoskeletal components of the growth cones is ImmunoFluorescence Microscopy (IFM). This microscopy technique is based on the specificity of antibody-antigen reaction so that cytoskeletal components such as microtubules and F-actin can be labeled using specific fluorescent ligand complexes and the fluorescent antibodies emit radiation at different wavelengths. So, IFM is an invasive technique which requires staining procedures of the specimen prior to imaging. IFM has successfully been employed to analyze the

microtubule and actin organization in the growth cones[10-12]. In order to analyze real characteristics of the growth cones, non-invasive microscopy approaches are required.

Phase Contrast Microscopy (PCM)[7] is a non-invasive tool which requires no additional sample preparation prior to imaging. The PCM offers direct quantification while IFM provides an indirect way since the spatial intensity variations in an IFM image is the map of fluorophores rather than the target complexes they are attached to. So, the quantification in IFM is limited to the antigen-antibody reaction. On the other hand, in PCM, the light interacts with the matter itself in terms of refractive index variations. These refractive index variations together with the thickness through which the light interaction takes place construct the PCM image. Because of this reason, PCM, when combined with AFM, can be used to quantify the refractive index variations in the growth cone. This is of importance to investigate cytoskeletal material organization of the growth cones using light interaction with the cytoskeletal components of the growth cones.

While light travels through a medium, the transmitted light carries information about optical properties of the medium depending on the origin of the interaction. PCM is one of the contrast enhancement methods used in optical microscopy utilizing the phase lag of light transmitted through a medium. The contrast of a PCM image is the transformation of the phase lag into visible light intensity. The interaction between light and matter in PCM microscopy is illustrated in Figure 1.2. The phase variations are different at the different regions of the biological structure. This is because of the different light propagation speeds exhibiting Optical Path Difference (OPD) variations. The OPD is the product of the refractive index and specimen thickness along the path in which the radiation interacts with the matter.

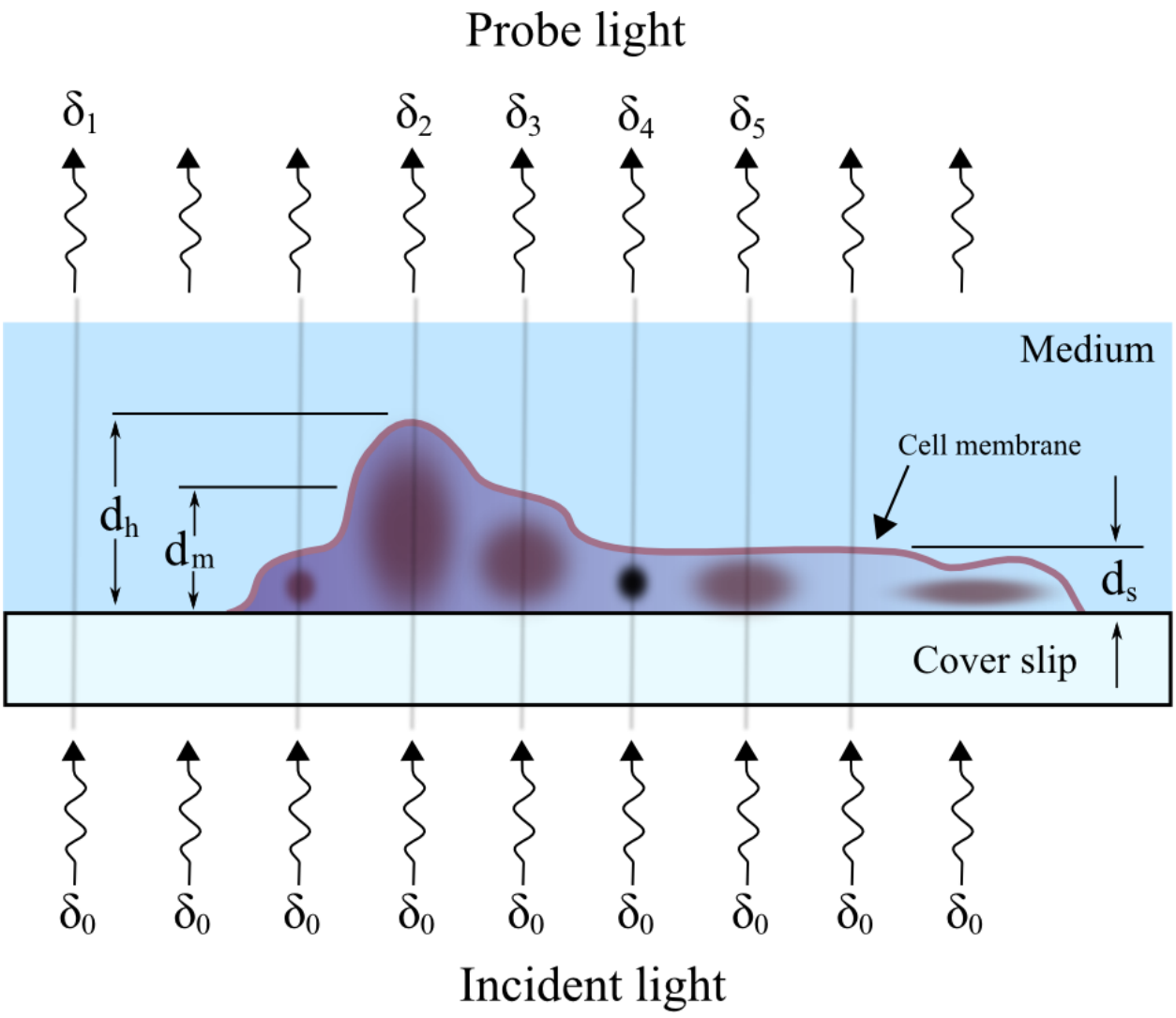

Figure 1.2. Phase contrast microscopy operation on a biological structure.

In Figure 1.2, the phase of the probe light experiencing different conditions such as refractive index and thickness are denoted by different subscripts. The contrast variations in the figure correspond to refractive index variations. $\boldsymbol{\delta_0}$ is the phase of the incident light. $\boldsymbol{\delta_1}$ is the phase of the light interacting with the cover slip and medium and, thus, is used as the reference for the PCM image. $\boldsymbol{\delta_2}$ and $\boldsymbol{\delta_3}$ are the phases of the lights interacting within the different thicknesses, $\mathbf{d_h}$ and $\mathbf{d_m}$, respectively. The corresponding PCM intensity would be different for both as long as the materials are of the same type and density along their interaction paths. $\boldsymbol{\delta_4}$

and δ_5 are the phases of the lights interacting within the same thickness d_S. Assuming the materials are not of the same type and density along their interaction paths, the corresponding PCM intensity would be different for both, although they have the same thicknesses of interaction. Therefore, thickness is the essential component to analyze the refractive index variations which might relate to different material type as well as material density variations.

The optical phase shift relation for the light passing through a biological structure in a medium can be written as

$$\delta = \frac{2 \cdot \pi}{\lambda} \cdot \left(n_{specimen} - n_{medium} \right) \cdot d \tag{1.1}$$

where δ is the phase shift, λ is the wavelength of the light, $n_{specimen}$ and n_{medium} are the optical refractive index of the specimen and the medium, respectively, and **d** is the thickness of the specimen. In the equation, δ refers to the differential change in the phase between the shifts introduced by cover slip-medium-cell and cover slip-medium due to the differential refractive index ($n_{specimen}$ - n_{medium}). Consequently, changes in δ are only due to the biological structure probed. In Figure 2, δ refers to the difference between δ_i (i=2,3,4,5) and δ_1. Using Equation 1, the differential refractive index can be analyzed by acquiring the phase, δ, from PCM and the thickness, **d**, from AFM. However, the following assumptions are necessary:

- *The functional dependence of the phase shift to wavelength is negligible. In PCM, visible wavelengths (Halogen lamp light source) are utilized in which the growth*

cones are quite transparent. Therefore, no significant spectral absorption feature is present. Also, the interaction between molecular energy levels and light is negligible.

- *The membrane thickness is constant over the growth cone. So, the membrane effect on the phase shift is a constant offset, which does not superimpose on the phase shift by the growth cone.*
- *The variation of refractive index is uniform along the path in which the light interacts with the growth cone.*
- *The depth of the medium is much larger than the thickness of the biological structure probed.*

The calculated differential refractive index using the approach above is quantitative with an unknown offset. This offset contains the refractive index of the medium, the PCM image contrast, and the membrane contribution. The refractive index of the medium depends on the solution type, concentration, and depth in the dish. The PCM image contrast depends on the instrumental parameters such as, focus, incident light intensity, and scattering within the optical path including the sample itself. However, the quantitative measurement of the internal refractive index is possible by quantification of these contributions on the offset. This calibration can be done by calibrating the PCM instrument and the medium by considering all possible effective components.

The PCM analysis together with the AFM results is promising for the non-invasive and the quantitative measurement of the cytoskeletal refractive index distribution. The variations in the refractive index in biological structures are mainly due to the variations in concentration and material type. Consequently, using a combined PCM-AFM approach, the number of molecules

and the cytoskeletal composition can be mapped over a biological structure. Furthermore, this information is essential to advance the nanomechanical analysis of biological events.

1.2 Surface morphological analysis of InGaN semiconductor alloys

Ternary $In_{1-x}Ga_xN$ alloys are of significant interest for the development of advanced optoelectronics[13] and high–efficient photovoltaic [14-16] device applications, due to their unique physical properties such as, direct band-gap, high carrier mobility, and strong chemical bonding[17]. The optical band gap in the $In_{1-x}Ga_xN$ alloy system can be tuned from Ultra-Violet (UV) (E_g^{GaN} =3.4 eV) to Near-Infra Red (NIR) (E_g^{InN} =0.7 eV [18,19]). Consequently, devices based on compositional controlled $In_{1-x}Ga_xN$ heterostructures have the potential to operate in a wide spectral range spanning over more than 80% of the solar spectrum and whole visible spectrum. The potential operation area of $In_{1-x}Ga_xN$ based devices is illustrated in Figure 1.3. At higher gallium compositions (x>0.5), the band-gap of this alloy system can be tuned within the visible spectrum, which for example is of interest for solid-state lightning applications. For instance, potential monolithic integrated Red-Green-Blue (RGB) LED chips can generate white light with tailored color points. $In_{1-x}Ga_xN$ alloys with higher indium compositions (x<0.5), are of interest for device components to be employed in optoelectronic communication applications. A further application utilizing the complete composition range is the development of high-efficiency monolithic multi-junction solar cells, which are capable of utilizing a large amount of solar irradiance (see Figure 1.3).

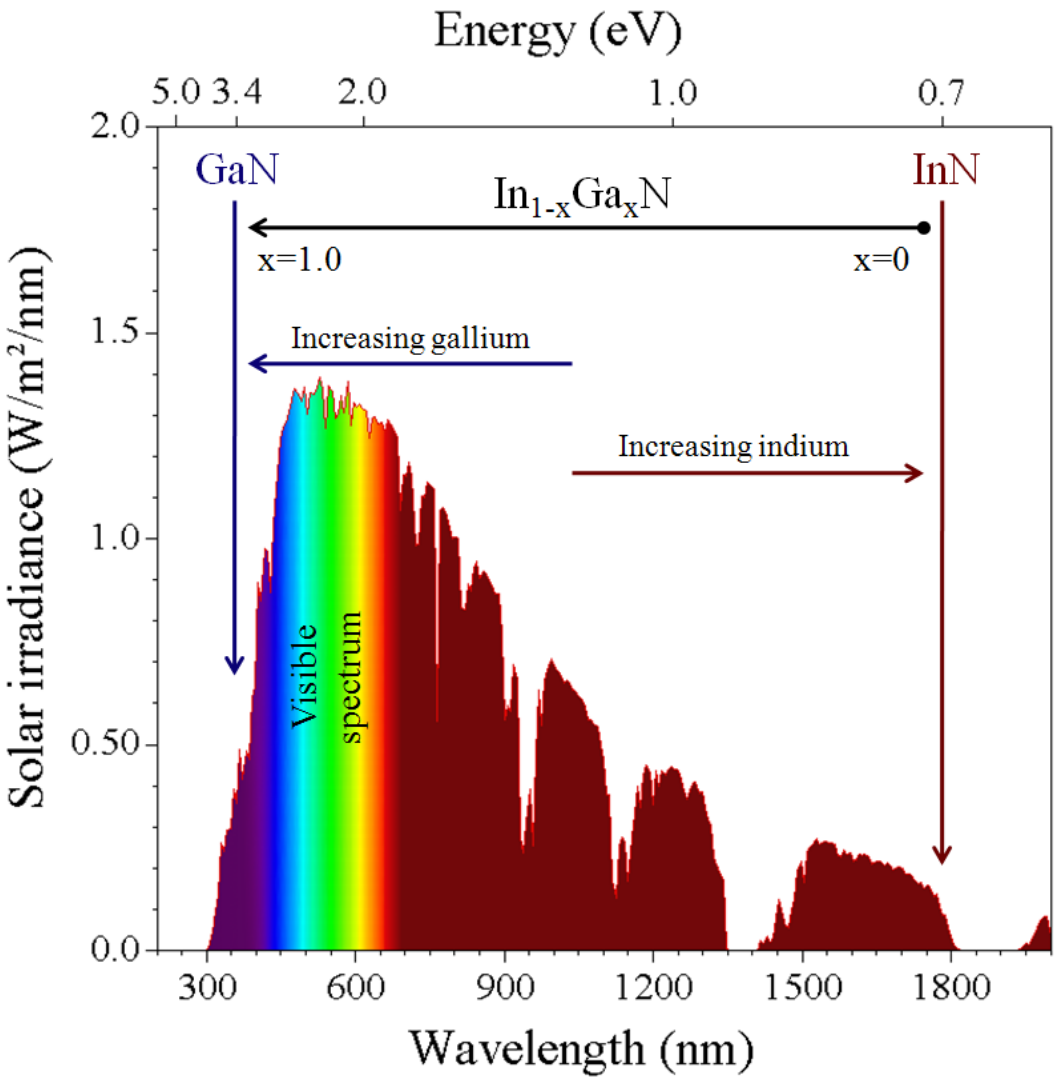

Figure 1.3 Potential band gap tuning of ternary $In_{1-x}Ga_xN$ alloys and solar spectrum at sea-level[21].

However, the growth of the $In_{1-x}Ga_xN$ alloys and heterostructures is challenging due to the large differences between thermodynamic and physical properties of the two binaries GaN and InN. Two of the main differences are

i) the lattice constants of InN (c=5.7034Å) and GaN (c=5.1250Å)[31], and

ii) InN has a much lower disassociation temperature compared to that of GaN.

The lattice mismatch between InN and GaN along c-axis is about 11%. This large lattice mismatch induces lattice strain[22], which may result in a potential solid-phase miscibility gap in the ternary $In_{1-x}Ga_xN$ system[23] or microscopic compositional inhomogeneities[25-29]. In addition, the lattice mismatch in GaInN/GaN heterostructures induces piezoelectric fields at the interfaces, adding to the difficulty to grow compositionally stable InGaN epilayers

The large differences in the disassociation temperatures leads to a difference in the growth temperatures of several hundreds degrees Celsius between the two binaries GaN and InN, which is a huge challenge in the growth and stabilization of embedded ternary $In_{1-x}Ga_xN$ heterostructures. Presently, the most common employed growth techniques for $In_{1-x}Ga_xN$ epilayers and related heterostructures are low-pressure deposition techniques such as Plasma Assisted Molecular Beam Epitaxy (PAMBE)[30-32] and Metal-Organic Chemical Vapor Deposition (MOCVD)[33,34]. While both techniques are able to stabilize the growth surface by off-equilibrium means for one compositional $In_{1-x}Ga_xN$ alloy, the large difference in the growth temperatures between different $In_{1-x}Ga_xN$ remains an unsolved problem and requires approaches that can reduce or eliminate growth temperature gap.

A potential path to reduce the growth temperature gap in the $In_{1-x}Ga_xN$ system is to explore the pressure dependency of the growth temperatures and to analyze the surface stabilization of $In_{1-x}Ga_xN$ alloys as a function of total pressure above the growth surface[35]. This path leads to the development of High-Pressure Chemical Vapor Deposition (HPCVD), a growth technique that utilizes the nitrogen reactor pressure as an additional control parameter to stabilize the growth surface in order to suppress the thermal decomposition process of $In_{1-x}Ga_xN$ alloys at higher growth temperatures[36].

To analyze the effects of the growth parameters (growth temperatures, partial pressures of the constituents, total reactor pressure, precursors, etc.) on the structural, optical, electrical and surface morphological properties of $In_{1-x}Ga_xN$ epilayers, a variety of real-time and ex-situ characterization techniques have to be applied. The combination of real-time and ex-situ characterization techniques is critical, since the physical layer properties are strongly influenced by the layer nucleation and potential nonlinear layer growth behavior and only the real-time data provide information on the growth history.

Gaining insights in the correlations between atomic level growth surface processes and physical thin film properties requires diagnostic tools on the nano-scale level as well spatially integrating methods. Surface processes such as adsorption, desorption, and surface diffusion processes[37] govern interface morphology and affect the optical and electrical bulk layer properties[38]. These surface processes are directly related to process parameters (temperature, precursors, partial pressures, etc.) and control the growth chemistry at the surface. The growth chemistry determines the crystal defect chemistry and the evolution of surface morphology due to the different growth modes and/or the different growth kinetics. Analyzing the surface morphology at different stages of the growth provide therefore information about the surface growth chemistry and can be indirectly related to the process parameters. In the next step, the nano-scale surface morphology information have to be correlated to the macroscopic level structural, optical, and electrical properties in order to improve the knowledge about the growth process and the physical properties of $In_{1-x}Ga_xN$ alloys.

The surface morphology analysis may also reveal correlations on how the lattice mismatch between growth template (substrate) and growing $In_{1-x}Ga_xN$ epilayers influence the material quality. Lattice strain and/or interfacial induced piezoelectric strain effect the growth

surface chemistry, resulting in surface morphological modifications leading to a different surface roughnesses and grain size/area distributions. These modifications may exhibit local variations at the growth surface, requiring investigations at different length scales such as, micrometers and millimeters. These investigations provide critical pieces of information on how the local surface morphological variations relate to the overall physical material characteristics.

Since most growth processes due not a allow real-time access to study the surface morphology evolution on a nano-scale during the thin-film growth process, a correlation has to be found between ex-situ surface morphology analysis data and real-time macroscopic optical surface topography characterization tools, such as laser light scattering (LLS)[36]. Also, since the growth surface chemistry depends on the growth mode, the formation of different surface facets - due to island growth, grain boundaries, etc. – may lead to different growth processing windows for the facets with less stable surface regions. Such unstable surface regions can also be introduces by lattice strain, when growing on lattice mismatch substrates. Therefore, the correlation between real-time surface topography characterization results and ex-situ nano-scale surface morphology analysis may reveal information on how the substrate template induced lattice strain affects the surface chemistry and the surface stability.

An important growth parameter is the temperature at the growth surface, which controls the surface kinetics of the adatoms during deposition. Analyzing the surface topography as a function of growth temperature reveals therefore information about the growth modes, a knowledge that can be integrated with the real-time observations to grow engineered nanostructures using constant or graded growth temperature profiles.

A further important aspect of this thesis is the correlation of the electrical properties of the $In_{1-x}Ga_xN$ epilayers with the surface morphology studies. The surface grain area and grain

provides only a snapshot at the end of the film growth process. However the grain density and grain area morphology is related to the amount of extended defects and point defect chemistry, which in turn relates the number of defect states and scattering centers, affection the carrier concentration and carrier mobility in the layer. A decreased grain area might result in an increase in free carrier concentration as the carrier mobility decreases due to the grain boundary potentials. Since the grain density is a result of increased crystalline strain, surface morphological analysis provides useful information linking the electrical and the structural properties of the $In_{1-x}Ga_xN$ layers.

1.3 Main tools to analyze surface morphology at nano-scale

Analyzing organic or inorganic surface topographies/morphologies at a nano-scale level requires combining the most appropriate microscopy technique available with the specific physical properties of the object under investigation. The criteria to select a suitable microscopy technique can be summarized as:

- required image resolution - or spatial resolution
- what is probed: topographical, electrical, optical, or magnetic properties
- invasive / noninvasive analysis?
- is specimen destructed - either in the preparation stage or during the probing process?
- static or dynamic systems (real-time)?
- physical properties of the specimen: conductivity, softness, elasticity, and microscopy environment; vacuum, liquid, variable temperature, and pressure

One of the first approaches to investigate nano-scale structural properties of materials is the electron microscopy, which utilizes an accelerated electron with a wavelength in the order of atomic distances. The wavelength of electrons moving with the speed v is given by[39]

$$\lambda = \sqrt{1 - \frac{v^2}{c^2}} \frac{h}{m \cdot v} \tag{1.2}$$

where λ is the wavelength of the matter, c is the speed of light, h is the Planck's constant, and m is the mass of the electron. According to the formulation, the wavelength of the electrons can be adjusted to values that allow a lateral resolution down to a few nanometers (nm's).

Over the last seventy years of development, a variety of electron microscopy techniques has been developed. Scanning Electron Microscopy (SEM) and Transmission Electron Microscopy (TEM) are extensively used in scientific research for high-resolution surface and cross-section analysis. However, most electron microscopy techniques are invasive and/or destructive, need an ultra-high vacuum environment, and they provide very limited information on the z-scale.

Other microscopy methods that can achieve nano-scale resolution are Scanning Probe Microscopy (SPM) techniques: Near-Field Scanning Optical Microscopy (NSOM), Scanning Tunneling Microscopy (STM), Atomic Force Microscopy (AFM), and variations thereof. NSOM undergoes spatial resolution enhancement by probe-matter distance and evanescent field interaction. This method provides crucial information about structural and optical properties in addition to topography information when integrated to other SPM techniques. STM was the first microscopy technique that achieved atomic scale resolution (10^{-10} m). The principle of an STM is based on utilization of feedback that is provided by tunneling current between tip and sample. An

operation limitation for STM is reached when the tunneling current between tip and sample vanishes or becomes too small, a phenomenon encountered in dielectrics and other insulating materials.

AFM is another atomic scale resolution SPM technique, where - as in STM – a feedback control signal is used to map the surface topographies of the specimen. The feedback control mechanism is provided by the attractive (noncontact mode) or repulsive (contact mode) forces between a tip and the sample. AFM can be applied to any type of material such as, conducting, non-conducting, hard, soft, dry or in liquid. Further details of these methods are given in the following three subsections.

1.3.1 Near-field scanning optical microscopy (NSOM)

The first optical microscopy approach using near field ($<\lambda$) behavior of radiation was first proposed by Synge[40] in 1928. In 1984, the applications of near-field microscopy using visible wavelengths were demonstrated[41,42]. Near-field scanning optical microscopy takes advantage of low physical dimensions to increase the spatial resolution by breaking the diffraction limit (~ 200-250 nm).

In NSOM, an optical fiber of very small aperture size ($<\lambda$) is brought close ($<<\lambda$) to the surface of interest. In near field approach, the resolution of NSOM image is limited to the aperture size of the optical fiber but not to the wavelength of the illumination. Therefore, fine details as low as 20 nm [43] can be resolved. The different operational modes of NSOM are shown in Figure 1.4.

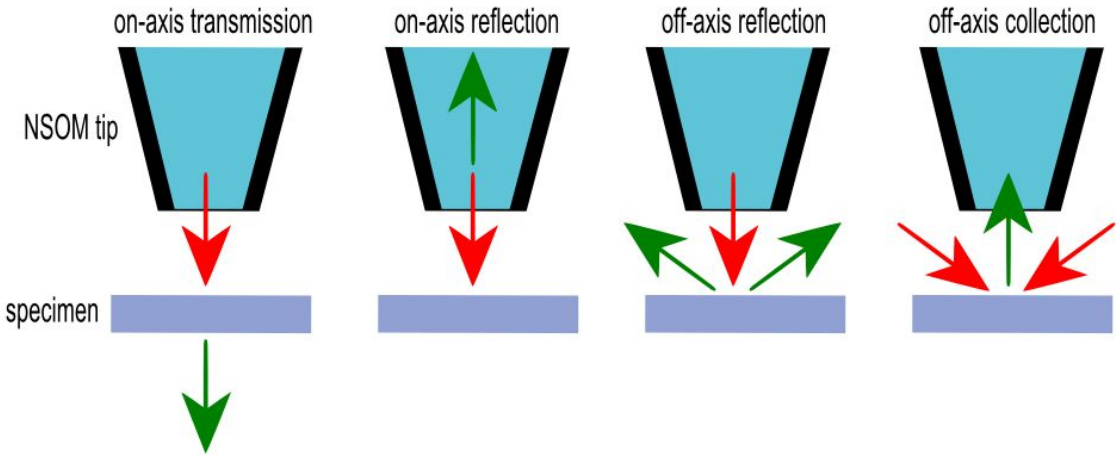

Figure 1.4 Near-field scanning optical microscopy (NSOM) operational modes.

There are different techniques to control the separation between NSOM tip and surface. The most common approaches to engage the NSOM tip to the surface can be summarized as;

- Optical interferometry: This method is based on the investigation of the diffraction of incident and reflected radiation.
- STM feedback: The tip-sample distance is controlled by using tunneling current. Therefore, this method is limited to applications in conducting samples only.
- AFM feedback: The feedback for z-positioning is provided from the interaction with surface forces. Two techniques for force feedback are common: 1) The lateral force feedback using an optical fiber attached to a quartz tuning fork, 2) The normal force feedback using a bent optical fiber with a reflective surface or cantilever with hollow tip.

Whatever the surface engagement technique is, NSOM combined with another SPM technique provides more than topography information. So, NSOM can be used to investigate the optical properties such as,

- dielectric function at surface
- wavelength dependent reflection and transmission
- modulation of light polarization
- optical spectroscopy analysis (Raman, IR, Fluorescence, Absorption)

1.3.2 Scanning Tunneling Microscopy (STM)

In 1931, was Ernst Ruska and Max Knoll introduced the first application of electron microscopy and demonstrated higher resolution than any other microscopy technique available at that time. In 1982, a new application of electrons in microscopy was introduced by Binnig and Rohrer[54 -44]. This new technique called Scanning Tunneling Microscopy (STM) relied on quantum mechanical phenomena, tunneling current, instead of wavelike particle behavior. With this new technique, Binnig-Rohrer shared Nobel Prize in physics with Ernst Ruska in 1986.

The operation principle of an STM is based on a sharp conducting cantilever that is brought closer to a voltage biased conducting surface, until a tunneling current can be established. This tunneling current is used as a feedback signal for mapping surface topography as the STM tip scans over the surface. The basic principle of an STM is depicted in Fig. 1.5. An STM can be operated in two different modes, constant height, and constant current modes. In constant height mode, after the tunneling current is obtained, the STM tip is scanned over plane while the changes in the tunneling current are monitored. This mode is favorable for height speed acquisition; however, it requires flat surfaces to eliminate the possibility of tip crashing to the surface. The information obtained in constant height mode is the map of tunneling current over surface. In constant current mode, after the tunneling current is obtained, the STM tip is scanned

over the surface as the tunneling current is kept constant. The surface topographical changes at surface induce changes in tunneling current since tip-surface distance is manipulated. The tunneling current is readjusted to the current set point by the motion of the z-servo. The motion of the piezoelectric z-servo provides a surface topography map.

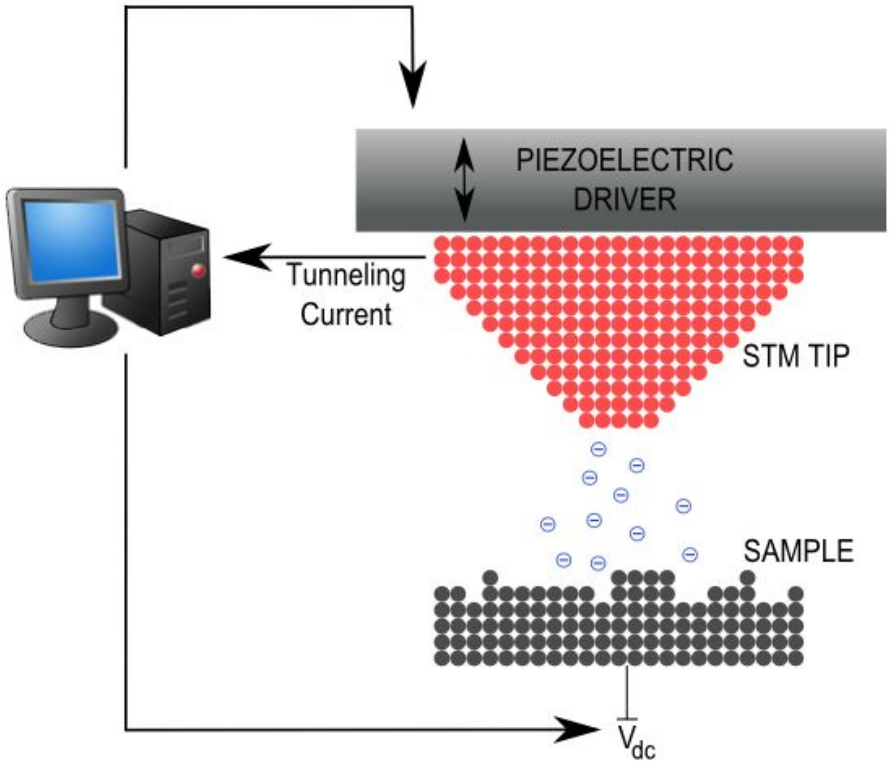

Figure 1.5 Principle of a scanning tunneling microscopy (STM).

In STM operation, the STM tip and the sample can be assumed as two metal plates separated by a very small distance behaving as a potential barrier. In the classic mechanical approach, electrons having energy less than the barrier potential are not allowed to pass other side. However, in the quantum mechanical approach, the probability of finding electrons within or beyond the barrier is finite since the probability function penetrates into potential barrier as a decaying exponential function. If the barrier width is small enough, the wavefunction does not collapse completely and results in presence of a tunneling current beyond the potential barrier.

The quantum mechanical description of STM operation can be done by assuming the separation between tip and sample behaves as a rectangular infinite potential barrier of width z. The solution of the wavefunction 0 (at surface) to z (at tip) is[45]

$$\Psi(z) = \Psi(0) \cdot e^{-\sqrt{2 \cdot m \cdot (\Phi - E)}/\hbar}, \tag{1.3}$$

where Φ is workfunction relating to barrier height and E is the energy of electrons to tunnel. The workfunction Φ is superposition of tip and sample contribution. The solution involves a negative real exponential indicating wavefunction decays exponentially since Φ>E. However, in other regions (<0 and >z), the solutions are harmonic and, thus, the tunneling electrons penetrate through the tip creating an electrical current. Therefore, the tunneling current can be detected only if is the STM tip conductive. The probability of finding electrons beyond the barrier is[45]

$$P(z) = \left|\Psi(z)\right|^2 = \left|\Psi(0)\right|^2 \cdot e^{-2 \cdot \sqrt{2 \cdot m \cdot (\Phi - E)}/\hbar}. \tag{1.4}$$

The tunneling current is proportional to the number of charges, which would be present probabilistically beyond the barrier. Assuming the tunneling current is due to the electrons having energy near the Fermi level[46], the tunneling current *I* can be written as

$$I \propto I_o \left|\Psi(z)\right|^2 = I_o \cdot \left|\Psi(0)\right|^2 \cdot e^{-2 \cdot \sqrt{2 \cdot m \cdot (\Phi - E)}/\hbar}, \tag{1.5}$$

where I_o is the electrical current if the STM tip and sample are in contact.

1.3.3 Atomic Force Microscopy (AFM)

Atomic Force Microscopy (AFM) [7] is a scanning microscopy technique that is capable of imaging three-dimensional surface topography with atomic resolution. AFM utilizes surface forces (Van der Waals, electrostatic, magnetic, chemical forces) as feedback signal with the aim

of keeping the tip-sample interaction force constant. Therefore, the sample doesn't have to be conductive as required in STM. The fundamental principle of an AFM is illustrated in Figure 1.6.

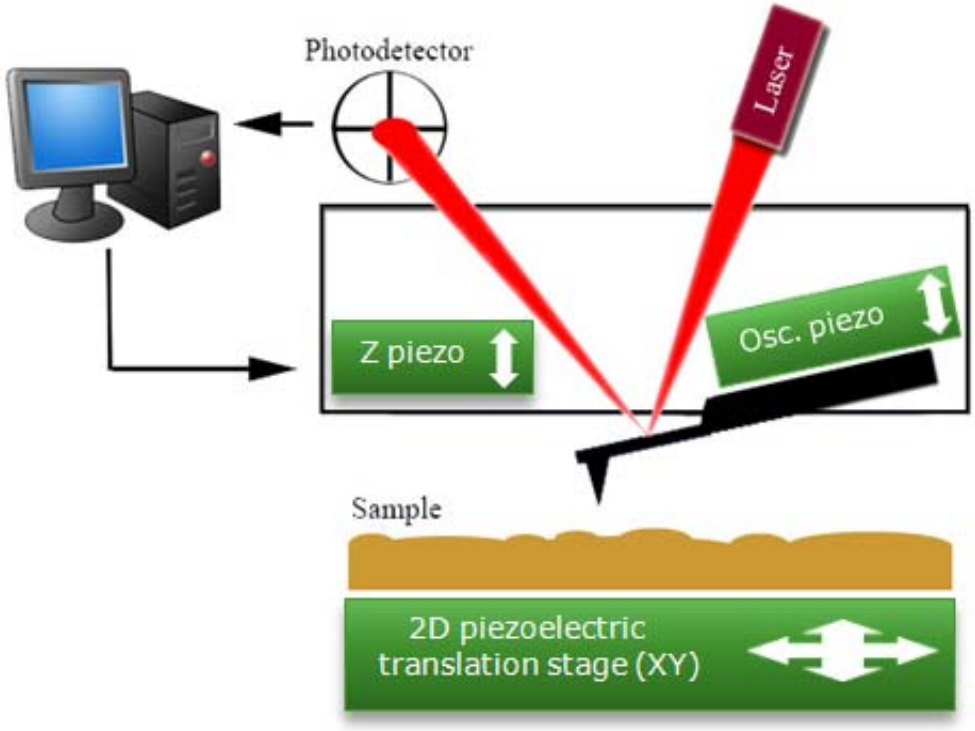

Figure 1.6 Principle of an Atomic Force Microscopy (AFM) in laser beam deflection mode.

A sharp tip mounted on a cantilever scans over the surface while the cantilever oscillates at resonance frequency. The deviation of oscillation frequency/amplitude from a set-point value provides a feedback signal that adjusts the tip-surface distance via a piezoelectric driver (Z-piezo) at every point. The changes in the position of the piezoelectric driver correspond to the surface topography, since the extension and retraction of piezoelectric crystal can be quantified as a function of applied voltage.

Besides surface topographical analysis, AFM can be used to investigate the mechanical surface properties such as softness and elasticity, using phase lag and amplitude information of the cantilever oscillation.

Although there are several different methods to measure the cantilever deflection, the laser beam deflection method is the most common used approach (see Figure 1.6). In this method, a laser beam is projected onto the back of a cantilever tip and the reflected beam is analyzed by a quadrant photo-detector. The four signals from each quadrant in the photo-detector used to generate differentials that can be related to the normal forces and lateral forces between cantilever tip and the sample. Whatever the origin of the surface forces are, AFM has five essential components:

- A sharp tip mounted on a cantilever. The spatial resolution of an AFM is given by the sharpness of the cantilever tip.
- A proper method to control the vibrational motion/oscillation of the cantilever.
- A feedback unit that drives piezoelectric z-servo by comparing the detected and set motion components of the cantilever.
- A high-resolution scanning stage.
- An electronic controller unit and a computer for data acquisition and monitoring.

AFM experiments can be performed in three modes, contact mode, non-contact mode and tapping mode. The modes differ by the nature of force interaction between cantilever and surface. In terminology “contact” doesn’t necessarily mean that the cantilever touches surface and “non-contact” that it doesn’t. In this very low force and dimension regime, they are just a measure of how close the tip is to the surface. Figure 1.7 shows the three different modes of AFM operation with respect to typical surface force curve.

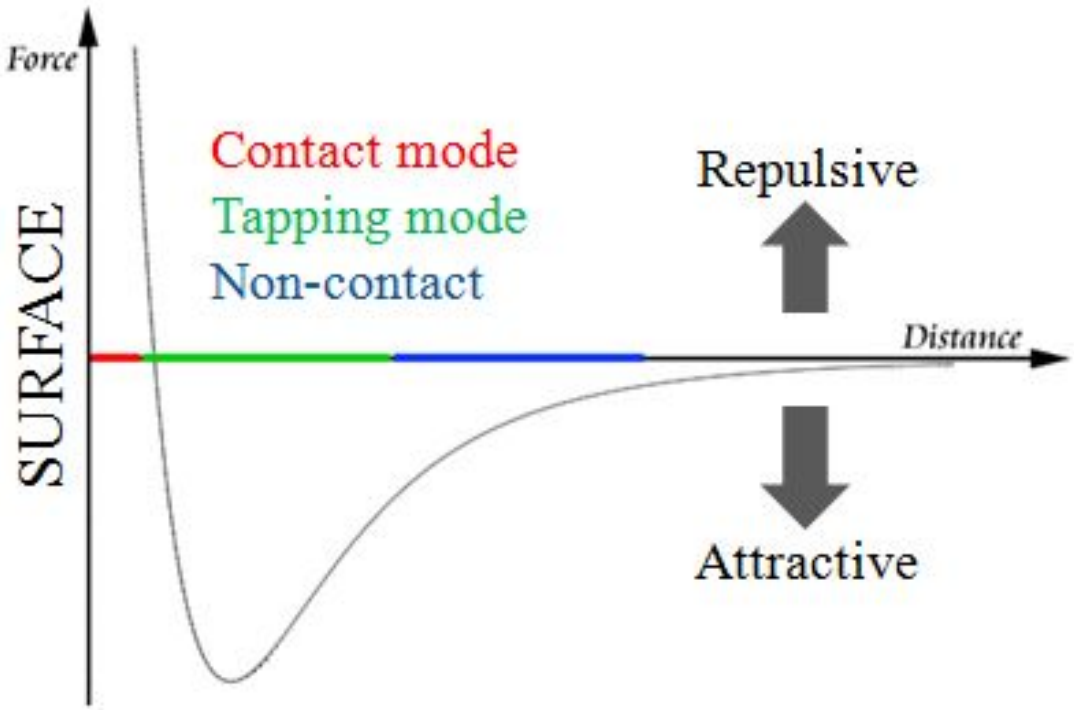

Figure 1.7 Atomic force microscopy operational modes on a typical Force-distance curve.

In contact mode, the repulsive forces between tip and the surface are utilized. The total tip-surface force is the sum of both large range van der Waals (vdW) and short range chemical interactions. For distances below 2Å, the chemical interaction is dominated by the Pauli repulsion and starts to balance the attractive van der Waals force. AFM images taken at small tip-surface distances, where the total tip-surface force is repulsive (the van der Waals interaction is smaller than the short range atomic repulsion, are said to be formed during the contact mode.

In a non-contact AFM mode (nc-AFM), the probe tip on the cantilever is not in contact with the sample, and long-range interaction forces, e.g. van der Waals, electrostatic, and magnetic force can also be probed. Unlike to the contact mode, the nc-AFM mode is sensitive to the force gradient, rather than the interaction forces between the tip and the sample surface.

To establish the feedback control signal, the cantilever is driven to oscillate at its resonance frequency by means of a piezoelectric element. The changes in the resonant frequency as a result of tip-sample interaction are measured and analyzed. The force gradient $F' = -\partial F_z/\partial z$ results in a modification of the effective spring constant of the cantilever.

$$k_{eff} = k - F' \tag{1.6}$$

where k is the spring constant of cantilever in the absence of tip-surface force interaction. An attractive tip-surface interaction with ($F' > 0$) will therefore soften the effective spring constant ($k_{eff} < k$), whereas a repulsive tip-surface force interaction ($F' < 0$) will strengthen the effective spring constant ($k_{eff} > k$). The change of the effective spring constant, in turn, produces a shift in the resonant frequency ω of the cantilever according to

$$\omega = \left(\frac{k_{eff}}{m}\right)^{1/2} = \left[\frac{(k - F')}{m}\right]^{1/2} = \left(\frac{k}{m}\right)^{1/2}\left(1 - \frac{F'}{k}\right)^{1/2} = \omega_0 \cdot \left(1 - \frac{F'}{k}\right)^{1/2} \tag{1.7}$$

where m is the effective mass and ω_o is the resonance frequency of the cantilever in the absence of force gradient. If F' is small relative to k then Eqn. (1.7) can be approximated by

$$\omega \approx \omega_0 \cdot \left(1 - \frac{F'}{2 \cdot k}\right) \tag{1.8}$$

Therefore,

$$\frac{\Delta\omega}{\omega_0} \approx -\frac{F'}{2 \cdot k} \tag{1.9}$$

an attractive force with ($F' > 0$) will lead to a decrease of the resonant frequency ($\omega < \omega_o$), whereas a repulsive force ($F' < 0$) will lead to an increase ($\omega > \omega_o$).

In tapping mode atomic force microscopy (T-AFM) - which is similar to nc-AFM - the cantilever tip is brought closer to the sample so that the bottom of it just barely hits, or "taps", the sample. The cantilever's oscillation amplitude changes in response to tip-to-sample spacing. An image representing surface topography is obtained by monitoring these changes. Soft samples are best handled by using T-AFM instead of contact or non-contact AFM. T-AFM is less likely to damage the sample than contact AFM because it eliminates lateral forces (e.g. friction) between the tip and the sample. In general, T-AFM is more effective than nc-AFM for imaging larger scan sizes that may include greater variation in sample topography and also for biological imaging where cantilever induced lateral forces can yield significant manipulative effects by other AFM modes, c-AFM and nc-AFM.

AFM has the capability of imaging surfaces of insulating samples such as, biological samples. Furthermore, it can image in different physiological conditions such as conditional media. In this research, AFM has been selected as the most appropriate microscopy tool to study the nano-scale surface morphological properties of neural growth cones, and InN and InGaN semiconductor material systems.

1.4 Research objectives

Nano-scale surface morphology characterization tools become increasingly important, as they provide the missing correlation links between microscopic structures and macroscopic physical properties. The imaging capability of Scanning Probe Microscopy (SPM) techniques at atomic scale has expanded the term microscopy beyond the traditional use of an "optical microscope", which was limited by observing the interaction between electromagnetic radiation with matter - in reflection or transmission. Scanning microscopic probes can utilize various

interaction forces between probe tip and specimen surface, enabling nano-scale interaction forces with imaging capabilities. The Atomic Force Microscopy (AFM) technique is the most dominant SPM technique, which delivers topography mapping of surfaces with atomic resolution while revealing information on the physical surface properties such as softness and elasticity. The AFM can be operated at various environments such as vacuum, air or in liquids. In this thesis, the AFM technique is utilized for the surface morphology characterization of organic and inorganic materials.

The AFM studies on organic surface structures focused on the topological characterizations of growth cones from chemically fixed Helisoma trivolvis B19 and B5 neurons, which widths and heights are below the optical diffraction limits. The surface morphology data are correlated to the structural properties of the neural growth cones. The objective of these studies is to correlate the surface topography information with phase-sensitive optical images in order to investigate cytoskeletal organization of the growth cones and its relation to the nanomechanical properties.

The AFM surface morphological studies on $In_{1-x}Ga_xN$ compound semiconductor epilayers aim to provide correlations between processing parameters with layer nucleation and growth dynamics. AFM surface topography analysis data (grain area/size and root mean square surface roughness) are correlated to the macroscopic structural, electrical and optical properties in order to improve material quality. These relations link the atomic scale structural properties to the overall physical properties of the $In_{1-x}Ga_xN$ epilayers.

Chapter 2

2. Surface morphology studies on neural growth cones

Neural growth cones are highly dynamic sensory structures located at the tip of neurites. During the development and regeneration of the nervous system, growth cones are responsible for guiding and extending neuronal processes to their targets in a process termed neuronal pathfinding[1]. Optical microscopy imaging techniques have been used to study the behaviour and morphology of growth cones for more than a century. However, traditional optical microscopes are limited by diffraction to a resolution of a few hundred nanometers, making it impossible to resolve morphological details smaller than 100nm. The recent advances in fluorescence microscopy have enabled new techniques providing a size-resolution better than 100nm. These techniques are based on using laser modes of different geometries, photoactivation and localization of energy states and structural illumination with image processing[47]. Although these fluorescence microscopy approaches may achieve size resolution better than the optical diffraction limit, the observations are made on the fluorescent markers, not on the structure itself. Therefore, optical microscopy approaches are still of crucial importance for non-invasive investigation of biological structures.

In optical microscopy, contrast enhancement methods, such as Phase Contrast Microscopy (PCM) and Differential Interference Contrast (DIC) microscopy, have been developed and used to image filopodia with a diameter close to 100nm [2]. These imaging methods provide a two-dimensional projection of the topography of a growth cone, but they do not provide information about the third dimension, which is the height information - or the z-axis.

However, to gain insight in the true morphology of any biological structure, techniques and/or concepts have to be developed to obtain/reconstruct the missing third dimension. Direct quantification of the nano-scale information on the third dimension are made possible by Atomic Force Microscopy (AFM)[7] and are used here to provide a detailed 3-D description of neuronal growth cones, and particularly of their filopodia.

There have been several reports on AFM studies on biological structures demonstrating the capabilities of AFM to characterize the topographic structures of biological objects with a nano-scale resolution[48-51]. The AFM investigations of nerve cells have been performed on living and chemically fixed nerve cells[52-63]. Some of these studies focused on comparing AFM topographic images with optical microscopy[58,59,62,63] and electron microscopy[53] images. While these reports provide valuable 3-D information on growth cones of several neuronal cell types[52,56,59,61,63], high resolution AFM information on the fine morphological details of Helisoma growth cones were still lacking. Such data are crucial for a better understanding of the biological and structural properties of growth cones, as they act as a model system of neuronal development and regeneration.

In this thesis, we investigated the three-dimensional morphology of two different types of growth cones from chemically fixed B19 and B5 neurons from the buccal ganglion of Helisoma trivolvis. A combination of PCM and AFM is used to obtain and reconstruct the three-dimensional architecture of filopodia, and to build a geometric model that would be useful for future modelling studies of signalling events in growth cones. Moreover, we demonstrate for a B19 growth cone that the combined analysis of PCM and AFM images allow to estimate a thickness normalized phase contrast image for more detailed insights in compositional and structural variations inside of growth cones.

2.1 Experimental methods

Preparation of Cell Cultures of Identified Neurons

Identified B5 and B19 neurons from the buccal ganglion of snail Helisoma trivolvis were individually removed and plated on polylysine (MW, 70-150 K; 0.25mg/mL, Sigma, St. Louis, MO)-coated, glass coverslip-bottomed cell culture dishes (Falcon 1008, 35 mm). These neurons were grown in 2 mL of conditioned medium per dish. Conditioned medium was made by incubating Helisoma brains (two brains per 1 mL) for 3-4 days in diluted Leibovitz L-15 medium (Invitrogen, Carlsbad, CA, USA). The diluted Leibovitz L-15 medium had a final concentration of 40 mM NaCl, 1.7 mM KCl, 1.5 mM MgCl2, 4.1 mM CaCl2, 5 mM HEPES, 50 µg/mL gentamycin, and 0.15 mg/mL glutamine in distilled water, and pH was adjusted to 7.3-7.4. Neurons were used 24-48 hr after plating in order to obtain mature growth cones.

Neuronal Fixation

Neurons were fixed at room temperature for 15 minutes with a solution containing 4% paraformaldehyde and 0.1% glutamaldehyde dissolved in Helisoma saline (pH=7.3-7.4). Then, dishes were rinsed twice with Helisoma saline for 5 minutes each. The final wash was replaced with Helisoma saline before imaging.

Optical Microscopy Imaging and Data Analysis

Neurons were viewed under a 100X oil immersion objective on a Sedival microscope (Jena, Germany). Images were captured by a CCD C72 camera (MIT Dage, Michigan City, IN, USA) and digitized on a frame grabber (Scion LG-3, Scanalytics, Fairfax, VA).

AFM Imaging and Data Analysis

AFM experiments were carried out by using a di MultiMode V microscope (Veeco Instruments) equipped with a Nanoscope V controller. The probes used for experiments were triangular cantilevers, which were made of Si_3N_4 and had Au reflective coating to maximize reflected laser intensity in liquid. Probes had a nominal resonance frequency of 11 kHz and a nominal force constant of 0.02 N/m. The typical tip curvature radius was less than 20 nm. In AFM operation in liquid, the observed peak position of resonance frequency of the cantilever was around 8 kHz. Tapping mode was used in AFM experiments and scanning speed was kept at less than 15 μm/seconds.

Optical phase-contrast images of cells and growth cones of interest were initially obtained by using phase-contrast microscopy. These images were later used to identify regions of interest imaged/analyzed by AFM. 26 filopodia from three B19 growth cones and 28 filopodia from six B5 growth cones were used in this study. The filopodium heights were measured from the cover-slip surface to the maximum height in both scanning directions. The filopodium widths were determined from the Full Width Half Maximum (FWHM) of the filopodium height profile analysis to minimize the effect of 'shadowing', which is caused due to sample softness and/or scan speed. Error values of the height and width measurements from AFM data were determined in the performed scan speed range as error percentage and had values of $\mp$ 3nm and $\mp$ 10nm, respectively. All mathematical calculations were done correspondingly and the 'standard error of the mean (SEM) error bars are indicated in the figures.

Geometric Modeling of Filopodia

The motivation for the geometric modeling is to describe the overall shape of filopodia in order to determine whether the filopodia structures differ between growth cones of different neuron types. Given that the filopodial diameter decreases from base to tip, we included this filopodial tapering behavior in the model. Figure 2.1 shows the model considerations used here. Although the real tapering behavior of individual filopodium height and width is not expected to be exactly linear, we assume in our model a linear tapering behavior to reduce the complexity and limiting variations to a first order differential. Another assumption is that the chemical fixation process of neurons does not affect the topographical profiles of filopodia.

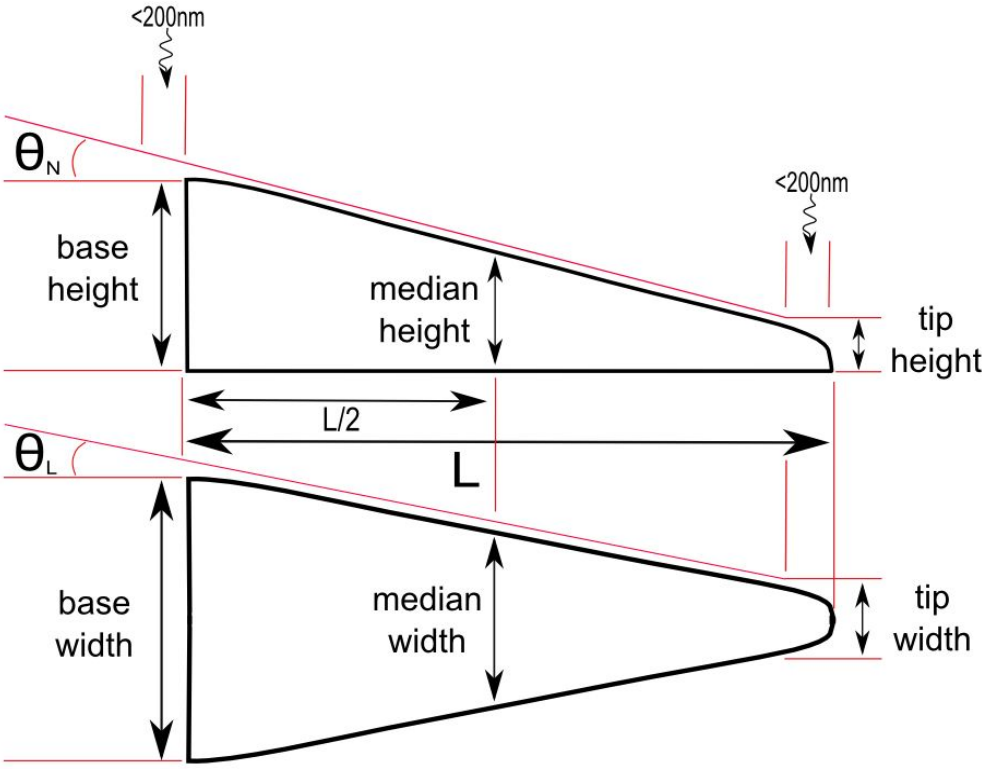

Figure 2.1 Schematic view of the geometrical model of a filopodium. θ_N is the normal tapering angle to parameterize the change in the height profile for different lengths. θ_L is the lateral tapering angle.

In the experimental data, three anchor points at different parts of a filopodium were chosen and analyzed: the base point was determined as a point within 200nm from where the

filopodium emerged from the lamellopodium; the tip point was any point at the farthest 200nm zone of the filopodium, and the median point was determined as half of the total length of a filopodium. The height and width data measured at these anchor points were analyzed independently to obtain the tapering information. The slope of the best linear fit of height and half of width gave tangents of the normal tapering angle θ_N and the lateral tapering angle $\theta_{L,}$ respectively.

Volumetric Analysis

The total volume of a filopodium was calculated with the geometrical simplification that a filopodium was approximated to a truncated cone of elliptical cross-section and uniformly decreasing area. The best fit lines to height and width at three points were used to calculate the area at the base (the region where the filopodium exits the lamellipodium and at the tip of the filopodium. Then, the total volume was calculated by integrating the basal area weighted by the product of the best fit lines to the upper limit of the tip.

2.2 Results

Growth cones are comprised of three domains, which are classified by cytoskeletal organization and functionality (Figure 2.2). The central domain (C-domain) is a thick, microtubule rich, central region containing organelles and transport vesicles. The transition zone (T-zone) is a region between the central domain and the flat peripheral domain (P-domain). The P-domain is actin rich and the most dynamic region of the growth cone. It is made up of lamellipodium (or veil) comprised of thin, sheet-like protrusions, and the filopodia, which are thin, finger-like extensions that are highly motile and act as sensory structures ahead of the

growth cone proper. In Figure 2.2, C-domain, T-zone, P-domain, filopodia and lamellipodium are shown and labeled by letters C, T, F, and L respectively.

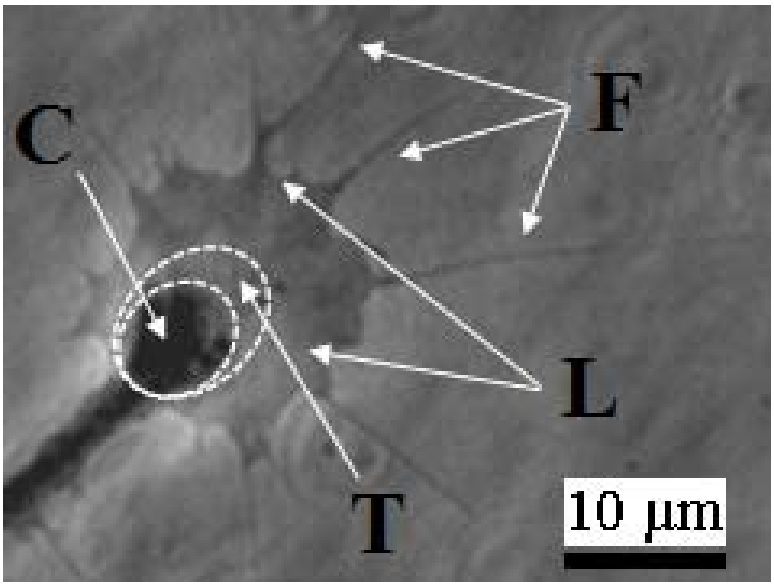

Figure 2.2 Structural domains of a growth cone. Letters C, T, F, and L stand for C-domain, T-zone, filopodium, and lamellipodium respectively.

The 3-D topography of growth cones was measured by AFM. A typical AFM image for a representative B19 growth cone is shown in Figure 2.3.a. Figure 2.3.b shows two height profiles through a growth cone along the axis of growth cone advance (arrow 1, profile 1) and perpendicular to it (arrow 2, profile 2). Note, that the neurite is approximately 200nm high and that the central domain is the highest point on the growth cone, reaching about 700 nm. From the central domain, the z-profile decreases towards the transition zone and from there to the P-domain which has a height of about 100nm. The statistical data analysis for the B19 growth cones investigated in this study is summarized in Table 2.1.

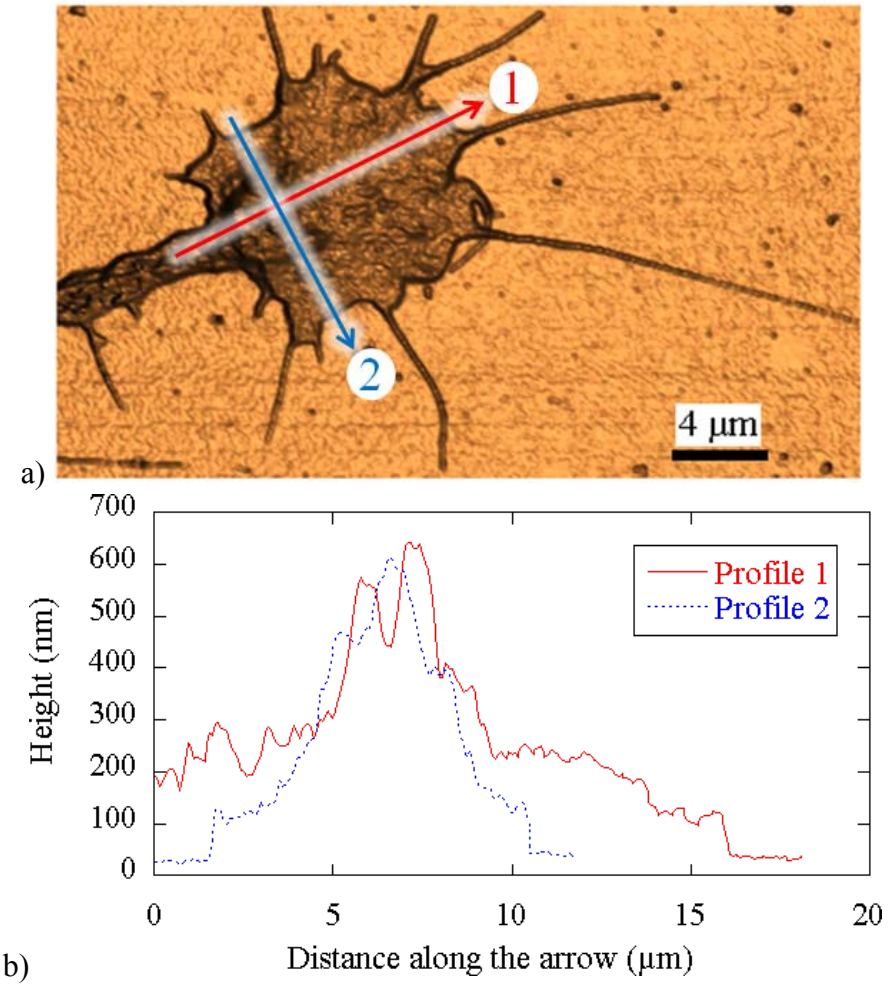

Figure 2.3. a) 3D AFM image of a growth cone of a chemically fixed B19 neuron. b) Height profiles calculated from (a) along profile lines 1 and 2.

The AFM analysis for a growth cone from a B5 neuron is depicted in Figure 2.4. The z-profiles starting on the substrate and extending into the C-domain indicate that the P-domain at its leading edge has a height of approximately 70nm. The lamellipodium has a width of less than 800 nm and from there, the height profile rises through the T-zone into the C-domain. At the very end of lamellipodia, narrow ridges are observed that rise above the height of the lamellipodium. The height of these ridges is very similar for B5 and B19 growth cones. Quantification of data obtained from all growth cones is summarized in Table 2.1.

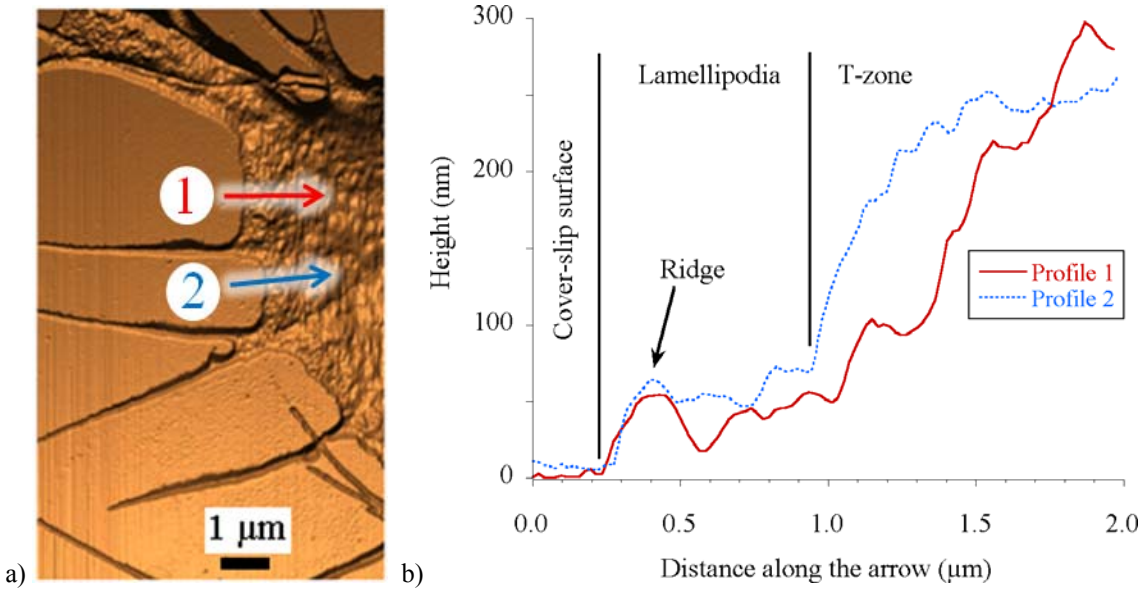

Figure 2.4. a) AFM image of the leading edge of a growth cone of neuron B5 showing filopodia, lamellipodia and T-zone. b) Line height profiles extracted from the regions shown by arrows.

In the next step, the topographic structure of filopodia was analyzed in more detail. High-resolution AFM images and height profiles of representative filopodia from growth cones of a B5 and a B19 neuron are shown in Fig.2.5.a and Fig.2.5.b, respectively. Note, that the z-profiles taken at the tip, at half length and at the base of each filopodium clearly indicate that filopodia are thickest at their base, where they emerge from the lamellopodium, and taper towards their tip. The average heights of filopodia at half-length and the arithmetic average of the observations at the three anchor point are both on the order of ~70nm for B19 and B5 growth cones.

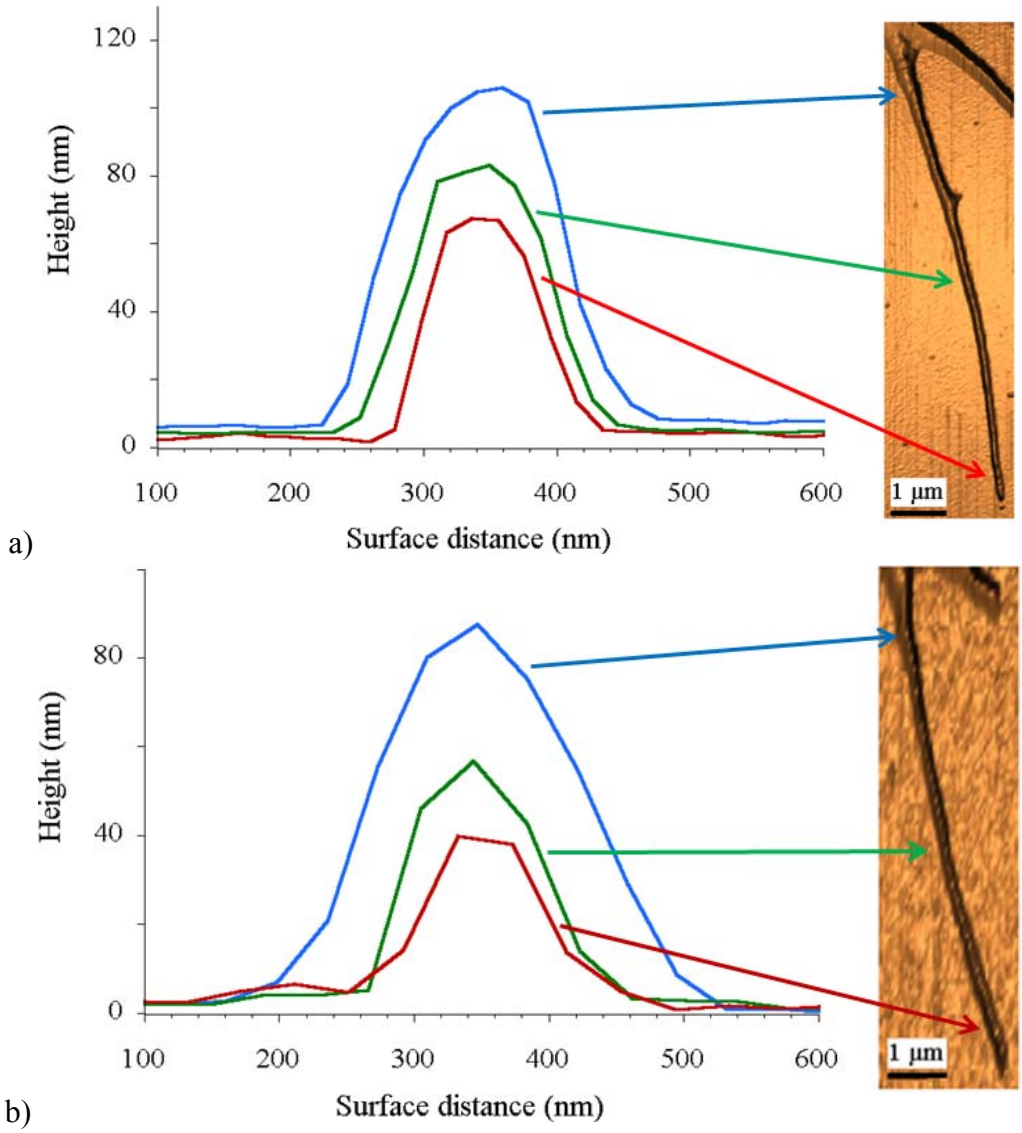

Figure 2.5. Height profiles at different locations along the length of filopodia from representative growth cones of a) B5 and b) B19 neurons. The measurement locations are indicated by arrows in the corresponding AFM images on the right.

From the observation that the height profiles of the filopodia undergo a tapering along their length, the filopodial tapering mechanism/behavior was analyzed by plotting the normal and lateral tapering angles versus the length for the B5 and B19 filopodia (see Figure 2.6). As

depicted in Fig. 2.6a, the best curve fit analysis showed that the normal tapering angle curve can be approximated by a inverse square root behavior:

$$\Theta_N\big|_{B5} \;:\; \frac{1}{\sqrt{\textit{filopodium length}}} \tag{2.1}$$

with R=0.82 for B5 growth cones and by a inverse behavior:

$$\Theta_N\big|_{B19} \;:\; \frac{1}{\textit{filopodium length}} \tag{2.2}$$

for B19 filopodia.

The lateral tapering angle versus filopodial length for B19 and B5 neurons are shown in Figure 2.6.b. The best curve fit analysis for lateral tapering angle reveals the same proportionality as found for the normal tapering angle, but with different radii. For the B5 growth cones the lateral tapering angle is inverse square root proportional to the *filopodium length* with R=0.66, and for the B19 growth cones the lateral tapering angle is inverse proportional to the *filopodium length* with R=0.77. For short filopodia, the tapering in B19 filopodia is steeper compared to that of B5 filopodia. However, for longer filopodial lengths, the effects of tapering become less pronounced.

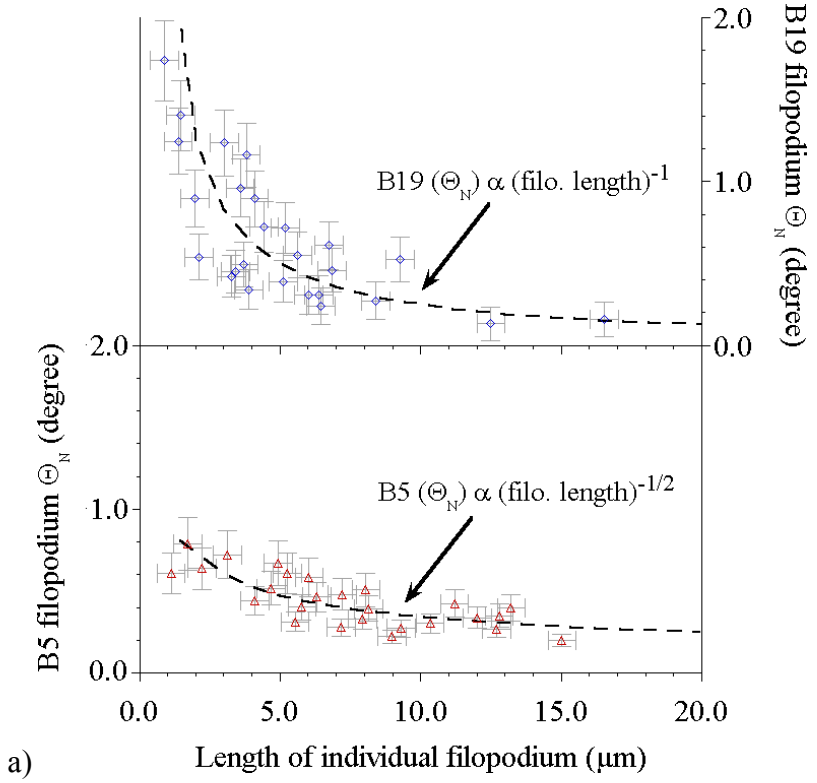

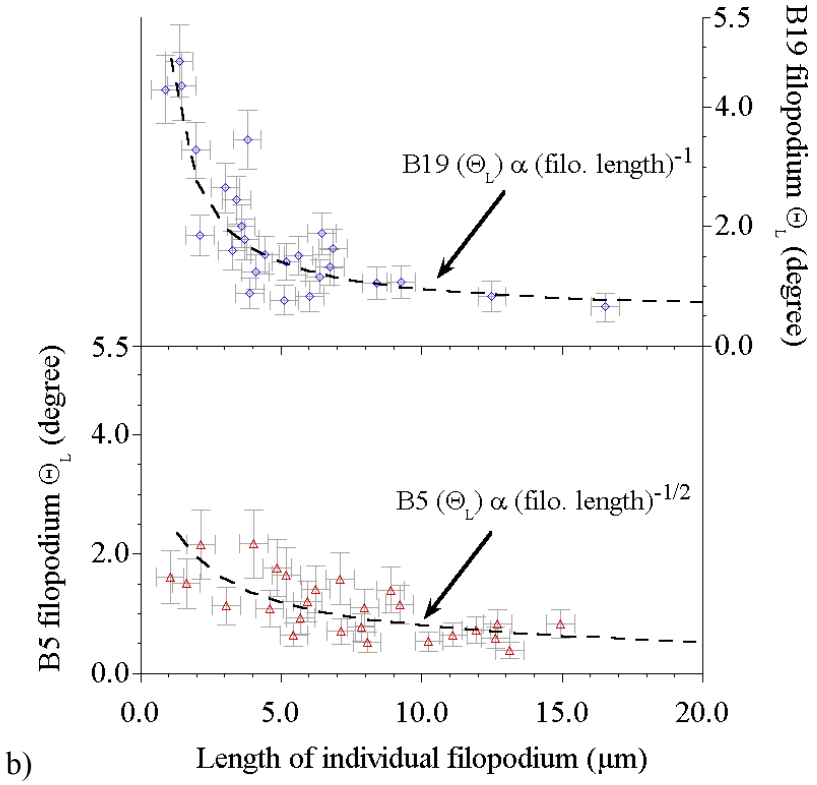

Figure 2.6 a) Normal tapering angle and b) Lateral tapering angle versus length of growth cone filopodia of B5 and B19 neurons.

Table 2.1 a) Summary of the AFM results obtained from different domains of the growth cones of B19 and B5 neurons. Filopodial dimensions are measured at their base, tip and at filopodial half length.

	Neuron B19			Neuron B5		
Observation	Average height ± SEM (nm)	Average width ± SEM (nm)	Number of observations (n)	Average height ± SEM (nm)	Average width ± SEM (nm)	Number of observations (n)
Filopodium base	102 ± 7	199 ± 24	26	101 ± 5	254 ± 46	28
Filopodium median	70 ± 6	139 ± 20	26	78 ± 3	177 ± 42	28
Filopodium tip	55 ± 4	111 ± 16	26	53 ± 2	143 ± 34	28
Lamellipodia	83 ± 6		36	70 ± 4		38
Lamellipodial ridge height	98 ± 3		17	96 ± 3		19
C-domain	446 ± 15		16	469 ± 12		18
Filopodium volume / length	11 ± 2 attoliter/µm			16 ± 2 attoliter/µm		

In order to investigate further the morphology of growth cones of Helisoma B5 and B19 neurons in detail, we started out comparing phase contrast microscopy and AFM images of identified growth cones. The Phase Contrast Microscope (PCM) utilizes specimen induced phase lags instead of intensity attenuation of electromagnetic radiation. The Optical Path Differences (OPD) causing phase lags are products of refractive index and thickness of specimen – relative to the surrounding medium. For instance, two specimens with large differences in thickness may result in the same OPD if the thinner specimen has a larger refractive index, so that products of individual refractive index and thickness of each are the same. Furthermore, two specimens of the same thickness may result in a large difference in OPD if their refractive indices are

different. In order to decouple refractive index and thickness, an independent measurement of either the refractive index or the thickness is required. Here, we use the thickness information obtained from the AFM imaging to calculate the refractive indices of specimens imaged by PCM. To do so, we assume that the refractive index value is constant over the thickness, which is a zero-order approximation and may have to be revised in a more detailed model. In the propagation of electromagnetic (EM) waves across interfaces, the phase shift relation can be expressed as

$$\delta' - \delta_0 = \frac{2\pi}{\lambda} \cdot (n_{sample} - n_{medium}) \cdot d \tag{2.3}$$

where $\delta' - \delta_0$ is the induced phase shift , λ is the wavelength of light, n_{sample} and n_{medium} are the optical refractive index of specimen and medium, respectively, d is the thickness of the specimen. The phase contrast in the PCM images is proportional to the induced phase shift. Using the thickness values d obtained from AFM measurements, we can define a thickness normalized phase contrast for each PCM image pixel and compute normalized phase contrast images (NPCI), which are proportional to

$$\frac{\delta' - \delta_0}{\mathrm{d}} = \frac{2\pi}{\lambda} \cdot (n_{sample} - n_{medium}) \tag{2.4}$$

As mentioned above, the assumptions made in this analysis are:

a) *Wavelength dependence of phase lag is negligible,*
b) *Membrane thickness over the growth cone is constant, so that the introduced phase lag amounts to a constant offset, and*

c) Variation of refractive index is uniform along the direction of observation (z-direction).

d) The depth of the medium is much larger than the thickness of the biological structure.

In order to analyze and compare the obtained PCM and AFM images, an image registration was performed in feature-based mode[50] where the physical growth cone boundary was used as the feature reference. After registering the images, we obtained the refractive index difference map of a B19 growth cone by dividing the phase contrast image (Figure 2.7.a) by the AFM image (Figure 2.7.b) on a pixel by pixel basis. Note, that the difference in the refractive index values for each pixel is the average value over the propagation distance of light through the specimen. The calculated differences in the refractive indices are contrast coded and represented in the image shown in Figure 2.7.c. The z-scale ranges from white to black, representing an increase in the refractive index difference towards black. The refractive index difference is a qualitative measure, since the PCM images are contrast based. The local variations in the differences of the refractive indices are related to the constituents in the medium and density of intracellular medium - both defining an average dielectric function of the medium that interacts with the electromagnetic field.

As mentioned above, the PCM image is a function of change in refractive index and thickness of the medium. Using the thickness information obtained from the AFM image, we can compute an image of 'refractive index differences' per thickness unit, where the image contrast is in first order directly related to the constituents and density of the medium. This approach significantly improves the contrast of local variations in T-zone and P-domain of the B19 growth cone.

Considering only the contrast information in the PCM images, the central domain of the B19 growth cone shows the largest phase contrast, whereas the phase contrast in the lamellipodium is small. This contrast is mainly due to differences in thickness of the medium, which is highest in the central domain and lowest in the lamellipodium. After normalization of the phase contrast for growth cone thickness, the C-domain shows a higher refractive index difference than the P-domain. This result can likely be explained by the fact that the C-domain contains both microtubules and f-actin, which together have a higher refractive index value than F-actin by itself, which serves as the main cytoskeletal component in the P-domain. After correction for height, the filopodial ‘ridges’ that run under the lamellipodium, are shown more clearly, indicating they have a higher refractive index compared to the surrounding lamellipodia.

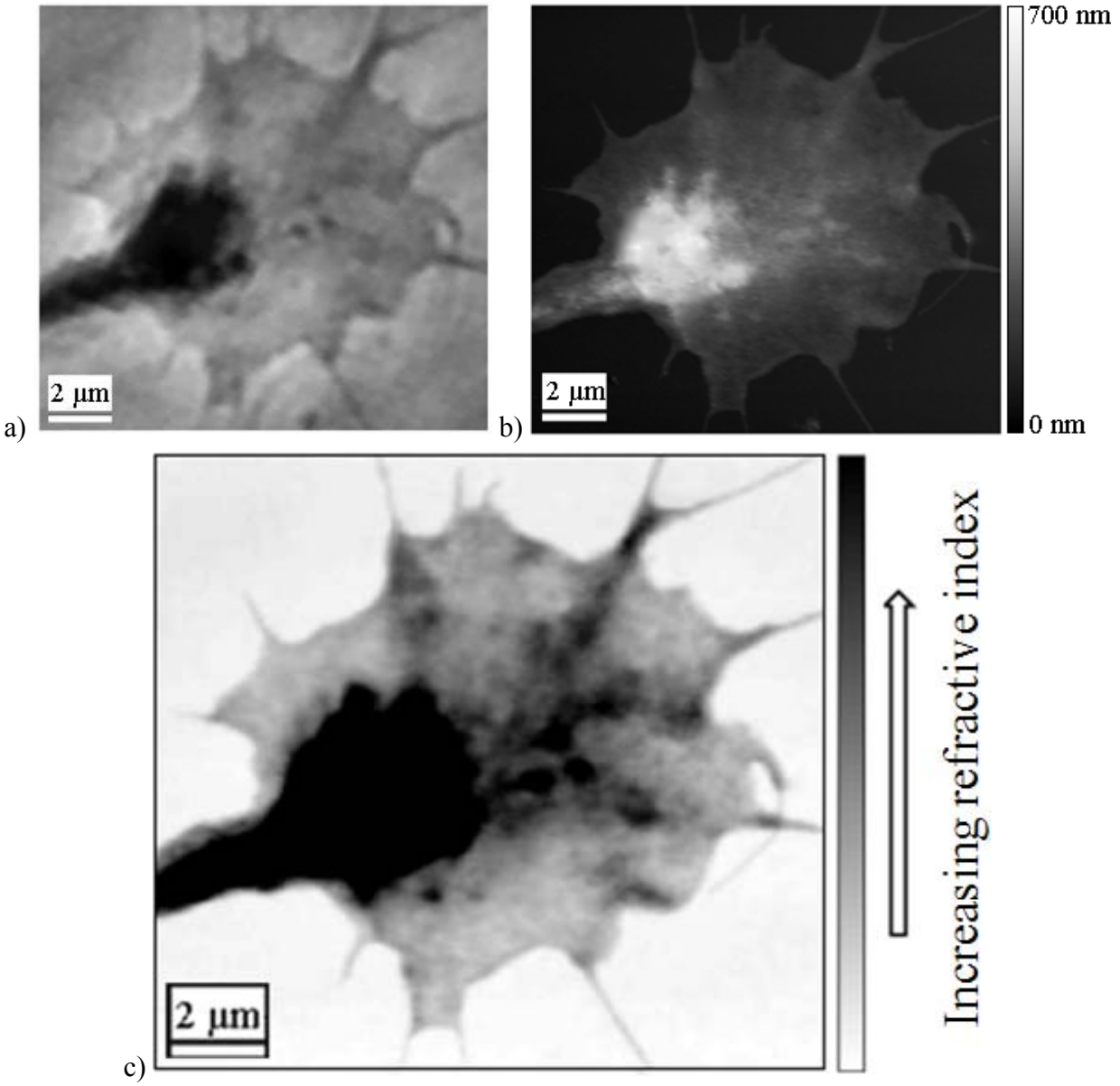

Figure 2.7. a) PCM, b) AFM , and c) refractive index difference images of a B19 growth cone.

Volumetric analysis:

After reconstructing the topographical structure of filopodia, the associated volumes of the B5 and B19 filopodia can be estimated by using volume model considerations described in the 'Experimental methods' section. The volume data obtained for filopodia were then used to calculate the total filopodium volume as a function of length. The average volume change per

length for B19 and B5 filopodia was found to be 11 ± 2 attoliter/µm and 16 ± 2 attoliter/µm, respectively. Given the very small volume of the filopodia, the question of interest is whether an estimate for the total number of free Ca ions in such a structure can be given?

The average volume change per unit length was used to estimate the absolute number of free Ca^{2+} ions as a function of filopodial length. The relations found are given in Equations 2.5 and 2.6 for B5 and B19 filopodia, respectively.

$$Number\ of\ Ca^{2+} = Filo.\ Ca^{2+} Molarity\ (\mu M) \cdot Filo.\ Length\ (\mu m) \cdot 9.6 \cdot (\mu M^{-1} \cdot \mu m^{-1}) \quad (2.5)$$

$$Number\ of\ Ca^{2+} = Filo.\ Ca^{2+} Molarity\ (\mu M) \cdot Filo.\ Length\ (\mu m) \cdot 6.6 \cdot (\mu M^{-1} \cdot \mu m^{-1}) \quad (2.6)$$

Calcium serves as an important second messenger in cells and changes in its concentration are used for diverse signalling purposes. The calcium concentration in filopodia is controlled by mechanisms that allow Ca^{2+} to enter the cytosol via influx through Ca^{2+} channels and by pumps and ion exchangers that reverse the entry of Ca^{2+}. To determine the effect of Ca^{2+} influx to the overall Ca^{2+} concentration, we calculated the number of Ca^{2+} ions necessary to double or triple the free Ca^{2+} concentration in a filopodium.

The calculations suggest that the number of free Ca^{2+} contained in both types of filopodia is quite low. For instance, a B5 filopodium with a length of 10 µm would only need about 10 Ca^{2+} ions to maintain an assumed free Ca^{2+} concentration of 100 nM. For a B19 filopodium of the same length 7 Ca^{2+} ions are needed to maintain a molar calcium concentration of 100 nM. The direct relation between the molar concentration and the number of Ca^{2+} ions suggests that, for a B5 filopodium, 20 ions would double the concentration as 30 ions would triple. For a B19 filopodium, 14 and 21 ions would double and triple the concentration, respectively. At assumed

conditions, a B19 filopodium requires 11 additional ions to triple the free calcium concentration while B5 filopodium requires 20. So, B19 filopodia require a smaller increase in the number of free Ca^{2+} ions than B5 filopodia to double or triple their free calcium concentration.

The efficacy with which Ca^{2+} ions entering a given cell volume will change the intracellular calcium concentration depends on several variables. For a very thin and elongated structure, such as a filopodium, the surface area is an important factor that will affect changes in the intracellular Ca concentration. Therefore, we next calculated the total surface area for B5 and B19 filopodia and assumed a constant density of calcium channels over surface area, with one Ca channel per μm^2. Figure 2.8 shows the results of these calculations for B5 and B19 filopodia. In both types of filopodia, the total number of Ca channels increases linearly with filopodium length.

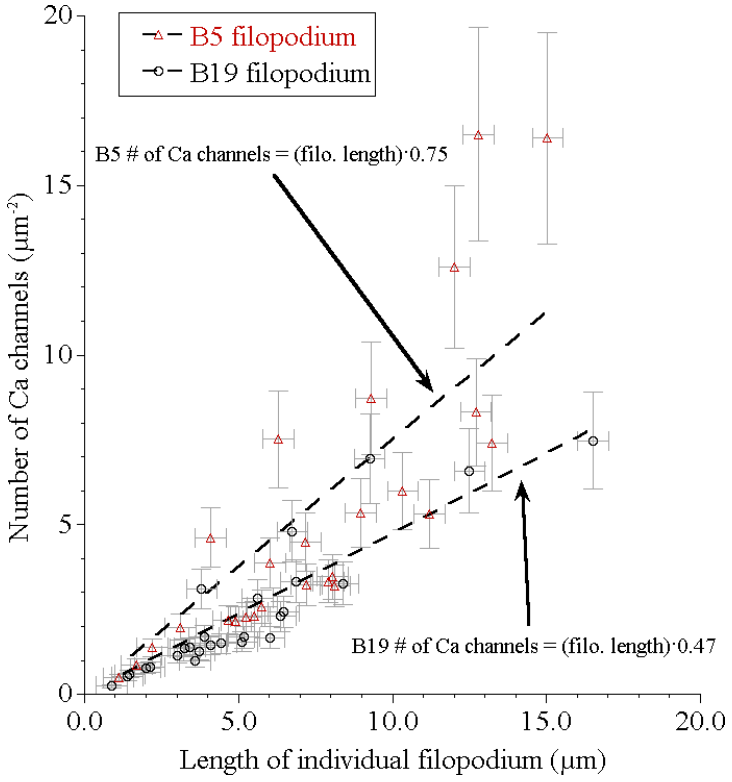

Figure 2.8 Calculated number of Ca^{2+} channels of B5 and B19 filopodia as a function of filopodium length. The surface Ca channel density was assumed to be 1 per μm^2.

This linear behavior indicates that the ratio of number of Ca channels to the individual filopodium length is a constant. This constant is 0.75 μm^{-1} and 0.47 μm^{-1} for B5 and B19 filopodia and directly related to the total surface area increase with increasing filopodium length. In the next step, we used the equations 2.5 and 2.6 to calculate the resulting free Ca concentration. In both equations, the concentration is a function of the ratio of number of Ca ions to the individual filopodium length divided by neuron specific multiplier which is 9.6 $\mu M^{-1} \cdot \mu m^{-1}$ for a B5 filopodium and 6.6 $\mu M^{-1} \cdot \mu m^{-1}$ for a B19 filopodium. Evaluating these equations together with the findings from the surface area analyses, we observed that the filopodial Ca concentration stayed constant for a constant number of Ca influx per channel. For instance, assuming 2 Ca ions influx per channel, the resulting free Ca concentration would be 160 nM and 140 nM for B5 and B19 filopodia, respectively. In Figure 2.9, the free Ca concentration is shown for changing number of Ca ions flowing per channel with the assumption of 1 per μm^2 surface channel density.

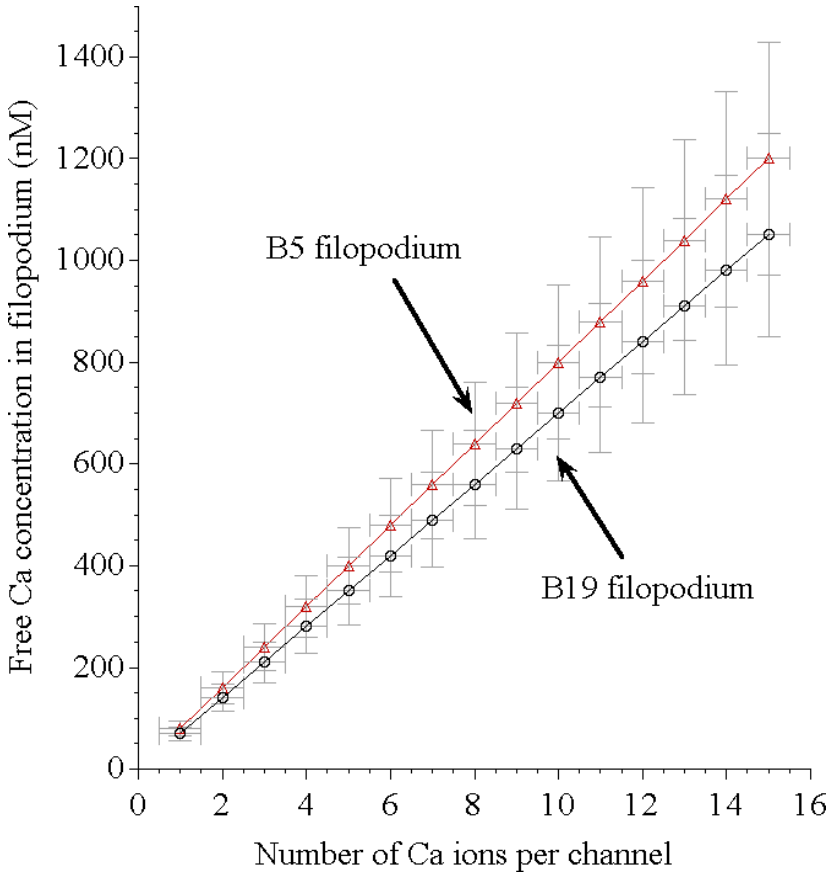

Figure 2.9 Free Ca concentration for B5 and B19 filopodia as a function of number of Ca ions per channel. The surface Ca channel density was assumed to be 1 per μm^2

2.3 Discussion

Surface topographical analysis on B19 and B5 neurons

The measurements of topographical details of growth cones showed that growth cones are highest at their C-domain and the height profile from there decreases towards the P-domain. No significant differences were observed between the average heights of the C-domain for fixed B5 and B19 neurons. However, the average heights of lamellopodia of B5 and B19 were found to differ. On average, B19 lamellopodia were about 10nm higher than those of B5 lamellopodia. Ridges of similar heights were located at the very ends of lamellopodia in both types of growth

cones. The average height of filopodia measured at the filopodial half length, as well as the arithmetic average of observations at the three anchor point are both on the order of ~70nm for B19 and B5 growth cones. These results are in good agreement with reports from filopodia of fixed hippocampal neurons and glia (68 ± 8nm)[52] , as well as from filopodia of fixed Aplysia neurons (73 ± 11nm)[59,61]. Although our height measurements of filopodia are in agreement with those reported in literature, our finding that filopodia do not have a constant diameter along their length suggests that the filopodial height and width can be better described considering their tapering behavior.

Filopodial tapering

According to the topographical analysis of filopodia, a tapering of the filopodia in height and width is observed for both B5 and B19 neurons. A simplified geometric model was constructed, which suggests that the tapering mechanisms in B5 and B19 neurons can be approximated to be propotional to $(filopodium\ length)^{-1/2}$ and $(filopodium\ length)^{-1}$, respectively. The correlation coefficients (R) were smaller in curve fitting analysis of lateral tapering compared to normal tapering. One potential reason for the smaller correlation coefficients for the lateral tapering might be the way how the filopodium width was determined. We used the full width half maximum of the filopodium height profile to measure the width, while the filopodium height was a direct measurement out of this profile. Filopodia of shorter lengths showed larger tapering angles compared to longer ones and this tapering behavior was different for B5 and B19 neurons. The tapering angle of B19 filopodia was steeper than in B5 filopodia with shorter filopodial lengths. At longer filopodial lengths, the difference between the tapering behaviours of B5 and B19 filopodia became less since both flattened rapidly. At present, the significance of

different filopodial tapering angles for the two neuronal types is not completely understood, nor the mechanisms by which they arise.

Evaluation of PCM images together with AFM images

Phase contrast microscopy (PCM) is a well established microscopy technique for imaging transparent biological structures with a size resolution of about 100 nm. Using a combination of PCM and AFM imaging a thickness normalized phase contrast image has been established, where the image contrast maps the refractive index variations in growth cones. The results of our analysis on a B19 growth cone indicated that the microtubules and F-actin located in the C-domain had higher refractive index than F-actin meshwork present in the P-domain of the growth cone. The filopodial 'ridges' that run under the lamellipodium show a larger refractive index change, suggesting a higher average dielectric function in this area - compared to the surrounding lamellipodia.

Volumetric analysis

The average filopodial volume was calculated for B19 and B5 filopodia and found to be on the orders of attoliters (10^{-18} liter). This very small volume constitutes a very confined biochemical environment in which signalling events elicited by contact of extracellular signaling molecules with receptors embedded at the filopodial tip are processed. We used this volumetric information to estimate how many free Ca^{2+} ions are required in a filopodium to maintain a calcium concentration of about 100nM typically found in resting cells. By using the average volume change per length, we estimated the number of Ca^{2+} ion as a function of filopodium length and filopodial Ca^{2+} molarity. One interesting finding was that the number of Ca^{2+} ions

contained in a filopodium is quite small for both types of filopodia. For instance, a B5 filopodium with a length of 10 μm would only need about 10 Ca^{2+} ions to maintain an assumed free Ca^{2+} concentration of 100 nM. For a B19 filopodium of the same length and Ca^{2+} concentration, this number would be about 7. Ignoring all other mechanisms supporting Ca^{2+} homeostasis in neurons, a 3-fold increase from 100-300nM in the free Ca^{2+} concentration would require the influx of about 20 Ca ions in B5 filopodia for a total of 30, while for B19 it would require an additional influx of 14 for a total of 21. So, tripling the concentration is possible in B19 by using about 2/3 of the Ca ions that would be required to triple the concentration in B5. Thus, 14 additional Ca^{2+} ions are required to triple the Ca^{2+} concentration in B19, compared to 10 required to double the concentration in B5 filopodia. Consequently, these low numbers of ions are of significant importance in Ca^{2+} signaling events in filopodia.

These numbers indicate, that relatively few Ca ions entering a filopodium are likely to result in significant changes in the free Ca concentration and would have strong signalling potential. Assuming a surface density of Ca channels at 1 μm^{-2}, the calculated number of Ca channels exhibited a linear dependency to filopodium length. In fact, these functional dependencies were different for B5 and B19 filopodia. Linearity of these dependencies suggested that, at any filopodial length, the Ca concentration would be the same for a constant ion inflow per channel and assuming all channels were active. Our analysis of changes in the Ca concentration resulting from different Ca ion counts in filopodia showed that very small changes in ion channel permeability would result in large changes in the free Ca^{2+} concentration in filopodia.

Chapter 3

3. Surface morphology studies on indium containing group III-nitrides

This chapter focuses on surface morphology studies of indium based group III-nitride semiconductors. The binary InN and ternary InGaN epilayers investigated have been grown by High-Pressure Chemical Vapor Deposition (HPCVD) technique, a growth method explored to study and optimize the processing conditions for InN and InGaN epilayers at elevated temperatures and pressures. In this chapter,

- *the basic properties of group III-Nitrides are provided, a brief history in the materials development is given, and the research objectives are formulated.*
- *the parameters and the capabilities of HPCVD growth system are detailed and the epitaxial thin film growth procedures are described.*
- *the effects of changing experimental parameters on surface morphology are reported.*
- *the correlation of results obtained from ex-situ characterization techniques to surface morphology studies is given.*

3.1 Properties of indium based group III-nitride semiconductors

The group III-nitride semiconductors have distinctive material properties that enable semiconductor optoelectronics devices to extend their operation into the areas where presently utilized material systems (e.g. the group III-As and Si) show severe limitations. Such application areas are for instance, blue/green Light Emitting Diodes (LED), UV/blue laser diodes, high-temperature electronics, spintronics, high-density optical data storage, and high-efficiency multi-junction photovoltaic energy conversion systems. Group III-nitride semiconductors are also suitable for device applications operating in extreme/harsh conditions such as, high temperature or high radiation background, which is a result of the stronger chemical bonding between group III atoms and nitrogen than that for conventional Si and III-V structures.

Group III-nitride compound semiconductor crystals and epilayers can either crystallize in wurtzite, zincblende or rocksalt structures[64]. The wurtzite crystal structure is a hexagonal system with $P6_3mc$ C_{6v}^4 point group symmetry. The sublattice is of type Hexagonal Close Pack (HCP) containing tetrahedrally configured group III elements and nitrogen atoms. The wurtzite crystal structure does not have inversion symmetry; thus, group III-nitrides exhibit piezoelectric properties. The zincblende crystal structure is a cubic crystal system and has $F\bar{4}3m$ T_d^2 point group symmetry. The zincblende crystal structure consists of two intersecting Face Centered Cubic (FCC) sublattices. The group III-nitrides of zincblende structure can be grown on substrates with cubic crystal structure such as, GaAs and Si. The rock-salt structure differs from zincblende in terms of the relative configurations in the lattice positions. Consequently, group III-nitride alloys with rock-salt crystal structure can only be synthesized at high pressures, [65] where the lattice positions are manipulated mechanically. Under conventional processing conditions such as low-pressure MOCVD or MBE, the stable crystal configuration for the group

III-nitrides is a wurtzite crystal structure, which is energetically favorable compared to the zincblende and rocksalt structures. However, the inclusion of zincblende and rocksalt phases into the wurtzite crystal structure has been observed and contributed to the number of structural defects in the material system[64].

The crystallographic defects play a major role for overall assessment of the physical properties and critically limit the efficiency of the device applications. Common types of defects in the group III-nitride structures include the extended defects such as, stacking faults, grain boundaries, etc., as well as point defects such as, vacancies, interstitials, antisides, impurities, etc. Structural crystal defects can be classified as:

- 0-dimensional: vacancies, interstitials, dopants
- 1-dimensional: line defects, dislocations
- 2-dimensional: stacking faults, grain boundaries
- 3-dimensional: precipitates and inclusions

One of the challenges in the growth of group III-nitride epilayers is the lack of close lattice-matched substrates with similar thermal expansion coefficients. One consequence of this problem is the lattice strain induced in the growing layer, which leads to the formation of stacking faults due to energy minimization by strain relaxation. Point defects are intrinsic, zero dimensional defects that affect the physical properties by disturbing the local symmetric structure due to an altered bond configuration. Point defects often contribute to an increased background doping and/or reduce the mobility of the free carriers in the semiconductor. The effect of the point defects on the optical and structural properties can be assessed by a variety of

characterization techniques such as absorption or Raman spectroscopy, photoluminescence, IR reflectance, etc., in terms of optical absorption centers and modifications in molecular vibrational states. In semiconductor materials, point defects, extended defects, doping, and impurities decrease the carrier mobility due to the increase in scattering centers for the carriers.

Growth chemistry is closely related to the inclusion of the structural defects. For instance, grain boundaries behave as extended defects as they grow. The amount of these grain boundaries depends on the grain areas which are determined by the growth chemistry at surface. The minimization of the inclusion of the structural defects can be achieved at the optimum growth conditions leading to the epitaxial thin film growth. The growth behavior during epitaxial growth is of importance in making up the overall physical properties of the layers.

Epitaxial growth is generally initiated by the formation of the individual islands and the advances by coalescence of the islands[66]. Epitaxial thin film growth can be categorized by three fundamental growth modes:

- *Frank-van der Merwe growth mechanism (2D) as illustrated in Figure 3.1.a in which the epilayers grow in a monolayer by monolayer mode.*
- *Volmer-Weber growth mechanism (3D) as illustrated in Figure 3.1.b in which growth is driven by individual 3D islands that subsequent coalesce and form a layer.*
- *Stranski-Krastanov growth mechanism (2D then 3D) as illustrated in Figure 3.1.c in which the growth initiates in a layer-by-layer growth mode and advances into an island growth mode for a layer thickness beyond a critical thickness The surface energy increase with the increased layer thickness determine this critical thickness* [211].

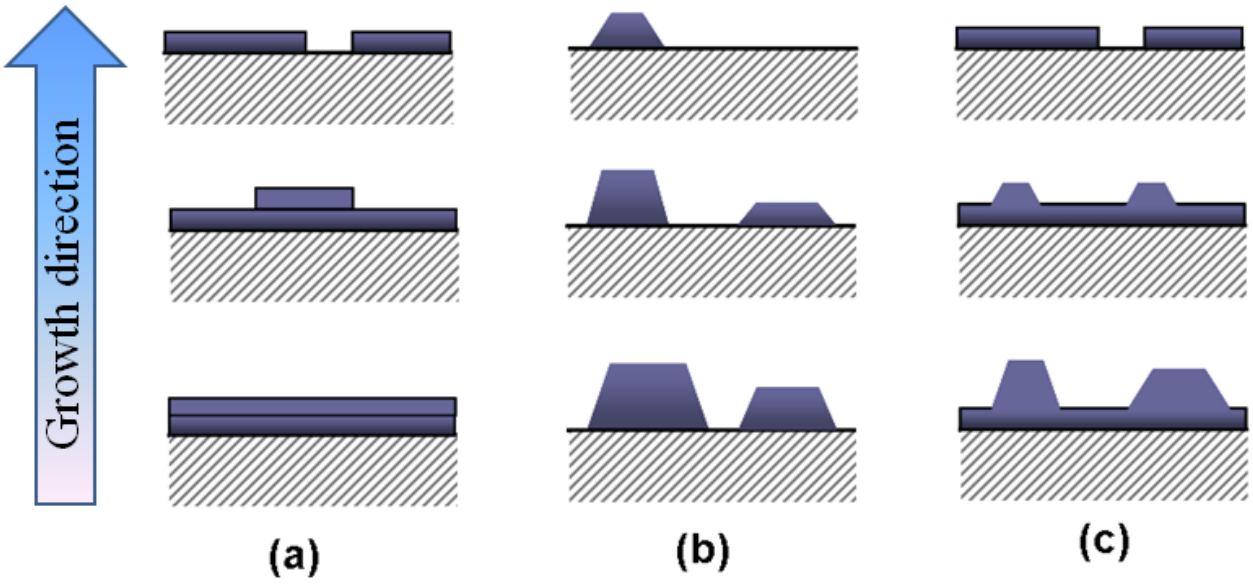

Figure 3.1 Epitaxial thin film growth modes: a) Frank-van der Merwe (layer by layer), b) Volmer-Weber (individual islands), and c) Stranski-Krastanov (layers then islands). (reproduced from Wikipedia)

3.1.1 Indium Nitride (InN) material system

Group III-nitride compound semiconductor alloys are important for opto-electronic devices operating in blue and ultraviolet (UV) region. Among group III-nitride alloys, the $Ga_{1-x}Al_xN$ material system is the most studied alloy system, covering a spectral range from 6.2eV (AlN) to 3.4 eV (GaN). The observation of the small band-gap of InN with 0.7eV [67-71] instead of previously reported 1.89 eV [72,73] dramatically increased the interest in InN and indium-rich $In_{1-x}Ga_xN$ due to the potential band-gap tuning to the Near-Infrared Regime (NIR). With this, quaternary group III-nitride alloys based on GaAlInN have potential to cover the spectral region from UV to NIR spanning whole the visible wavelength regime. The growth of high-quality quaternary alloys and heterostructures over all compositional range is crucial for the development of multitandem solar cells, advanced high-speed optoelectronic structures, monolithic integrated spectral tunable light sources, and high-efficiency photovoltaic converters

[74,75] operating in a wide spectral range [74,76]. Despite the significant progress made in recent years in the growth and the understanding for the binary group III-nitride systems (GaN, AlN, and InN), the formation of indium based ternary/quaternary alloys and the realization of their fundamental properties are still limited due to various factors. Some of these factors are

- *the high lattice mismatch between GaN-InN and AlN-InN, which leads to substantial lattice introduced strain as function of composition for ternary or quaternary alloys. The lattice mismatch in c-direction of the wurtzite crystal is 4% for GaN and AlN, 9.6% for GaN and InN, 13.6% for AlN and InN [77].*
- *The differences between the growth temperatures between the individual binary systems evoking different processing conditions - e.g. partial pressures, temperatures, etc. - for the growth and stabilization of the ternary or quaternary group III-nitride alloys.*

The synthesis of InN was first reported in 1938 for powder samples. The structural analysis revealed that InN has wurtzite crystal structure[78]. In 1972, the growth of InN films on sapphire and silicon substrates was reported[79]. The films were grown by RF sputtering and showed reasonably good electrical properties (Hall mobility 250 ± 50 cm^2/Vs, and n-type carrier concentration $5.8 \cdot 10^{18}$ cm^{-3}). The first study on surface morphology of InN was reported in 1984 [80]. This study analyzed the effects of surface conditions on the physical properties of the InN layers grown by RF sputtering. Another study reported in 1984 provided evidence for high carrier mobility in InN[81]. The first epitaxial growth of InN was demonstrated in 1990 on Sapphire (0001) substrates by Metal Organic Vapor Phase Epitaxy (MOVPE) and high film quality was achieved for the growth temperatures less than 500 ^oC[73]. In 2002, the band-gap of

InN was found to be 0.7eVfor MBE grown InN epilayers[82,83]. The magnetic properties for InN layers doped with Cr were reported in 2005 discussing the ferromagnetism[84,85] and its relation to n-type doping of the layers[84,86,87]. The thermoelectric properties of InN layers were investigated in 2005 and the first InN based thermoelectric devices were presented[85]. Theoretical studies investigating surface accumulation on InN layers were reported[88,89,90] employing ab-initio calculations based on Density Functional Theory (DFT) and Local Density Approximation (LDA) on the electronic structure[88]. An unusually low conduction band minimum at the zone center was reported to be responsible for surface donor states. Another study reported pinning due to the location of the Fermi level located above the valence band, was responsible for donor type states at surface[90].The experimental investigation of surface accumulation at InN/GaN and InN/AlN interfaces was published in 2005[91,92,93]. The results of this study revealed that the charge accumulation was more in InN/AlN interface than InN/GaN[91]. Capacitance-voltage measurements on MBE grown InN layers showed excessive amount of sheet charge which was attributed to the surface charge due to surface indium accumulation. Since 2000, another issue in InN layers has been the high level of n-type background doping[94]. In 2008, a study on the effects of hydrogen related donors on n-type doping of InN layers was published[95] which demonstrated H-type donors contributed to n-type doping of the layers. In the following table, the physical properties of unstrained InN are summarized.

Table 3.1 Summary of basic parameters of epitaxial InN films

Crystal structure and symmetry	Wurtzite C^4_{6v} ($P6_3mc$)	Cubic $\underline{F}4\ 3m$
Lattice constant, a_0(Å)	3.5377 [74]	
Lattice constant, c_0 (Å)	5.7037 [74]	4.986[101]
Effective mass (m_0)	0.07 [96], 0.11 [97,98], 0.12 [72]	0.066[102]
Mobility(cm^2/Vs) (Theoretical)	4400 [82]	
Mobility(cm^2/Vs) (Experimental)	3500 [83]	
Peak drift velocity (cm/s)	$5x10^{27}$ [73]	
Static dielectric constant	15.3 [99]	
High frequency dielectric constant	8.4 [75,100]	
Band gap (eV)	0.8 [68], 0.7 [71], 0.65 [70]	0.595[103], 0.65[104]

3.1.2 The ternary Indium-Gallium-Nitride (InGaN) alloy system

The ternary $In_{1-x}Ga_xN$ compositional alloy system spans between the two binary group III-nitride semiconductor alloys InN and GaN. The physical properties of $In_{1-x}Ga_xN$ alloys vary – e.g. nonlinearly – between those of InN and GaN semiconductors. The GaN compound semiconductor crystallizes also a wurtzite crystal structure, is chemically stable, and has a large heat capacity[105]. Its physical properties are uniquely suited for devices operating in extreme environmental conditions. The following table summarizes the physical properties of unstrained GaN.

Table 3.2 Summary of basic parameters of epitaxial GaN films

Crystal structure and symmetry	Wurtzite C^4_{6v} ($P6_3mc$)	Cubic $\underline{F}4\ 3m$
Lattice constant, a_0(Å)	3.189 [96]	
Lattice constant, c_0 (Å)	5.185 [96]	4.52[110]
Effective mass (m_0)	0.2 [82] m_o	0.13[110]
Mobility(cm^2/Vs) (Theoretical)	1000 [106]	
Mobility(cm^2/Vs) (Experimental)	900 [107]	
Peak drift velocity (cm/s)	$3x10^2$ [73]	
Static dielectric constant	15.3 [108]	9.7[110]
High frequency dielectric constant	5.3 [96]	5.3[110]
Band gap (eV)	3.47 [109]	3.2[111]

One of the earliest reports on the synthesis of GaN goes back to 1969, where the first GaN layers were grown by MOCVD.[112] Those epilayers showed a high free carrier concentrations - similar to what is presently observed in InN epilayers. In 1989, the p-type GaN layers were successfully grown by using a low temperature (LT) AlN buffer layer[113]. Since then, GaN based optoelectronics devices have been developed despite ongoing challenges to tackle in p-type GaN films such as low hole mobility, low hole concentration, and low resistivity ohmic contacts.

The binary InN has the potential to be active in NIR and visible region in its alloy with GaN after it was observed to have a band-gap value of 0.7 eV instead of previously believed 1.9

eV. The ternary $In_{1-x}Ga_xN$ alloys are promising material systems for the advanced optoelectronics[114] (i.e., fiber-optic communication) and high efficiency photovoltaic[115-117] (i.e., multi-junction solar cells) applications. The devices based on $Ga_{1-x}In_xN$ / $In_{1-x}Ga_xN$ heterostructures span a spectral range from UV (E_g^{GaN}=3.4 eV) to NIR (E_g^{InN}=0.7 eV).

However, the growth of $In_{1-x}Ga_xN$ alloys is challenging due to the lower thermal disassociation temperature of InN than GaN and the high lattice mismatch between them (~11%). The integration of higher concentrations indium in $Ga_{1-x}In_xN$ is a challenge in the presently employed low-pressure deposition techniques such as, molecular beam epitaxy (MBE)[118-120] and metal-organic chemical vapor deposition (MOCVD)[121,122] due to thermodynamic limitations such as, the difference between the processing temperatures and lattice mismatch. In order to take further steps on development of InGaN alloys, the compositional dependence of its physical parameters on composition has to be understood.

The physical parameters of the $In_{1-x}Ga_xN$ system (lattice parameters, band-gap, lattice vibrations etc.) depend on the composition, and they are calculated by interpolating the physical parameters of the base binaries InN and GaN. In order to develop successful $In_{1-x}Ga_xN$ based devices of precise tunability, understanding the compositional dependence of the band-gap is essential, which is given as

$$E_g^{In_{1-x}Ga_xN} = x \cdot E_g^{GaN} + (1-x) \cdot E_g^{InN} - b \cdot x \cdot (1-x) \qquad (3.1)$$

as function of composition x. The coefficient *b* in Equation 3.1 refers to the bowing parameter with the unit eV. Reports on the bowing parameter value range from 1eV to 6eV [123,124]. The current status of the band-gap dependence of $In_{1-x}Ga_xN$ on composition is illustrated in Figure

3.2. The large spread in the bowing parameter is an expected result due to the complexities in $In_{1-x}Ga_xN$ grown at different experimental conditions by different techniques. The complexities consist of crystalline lattice strain introduced by high lattice mismatch, compositional inhomogeneities, and phase separation. Consequently, the determination of the band-gap dependence on the composition is a difficult task and is still under investigation by several research groups worldwide.

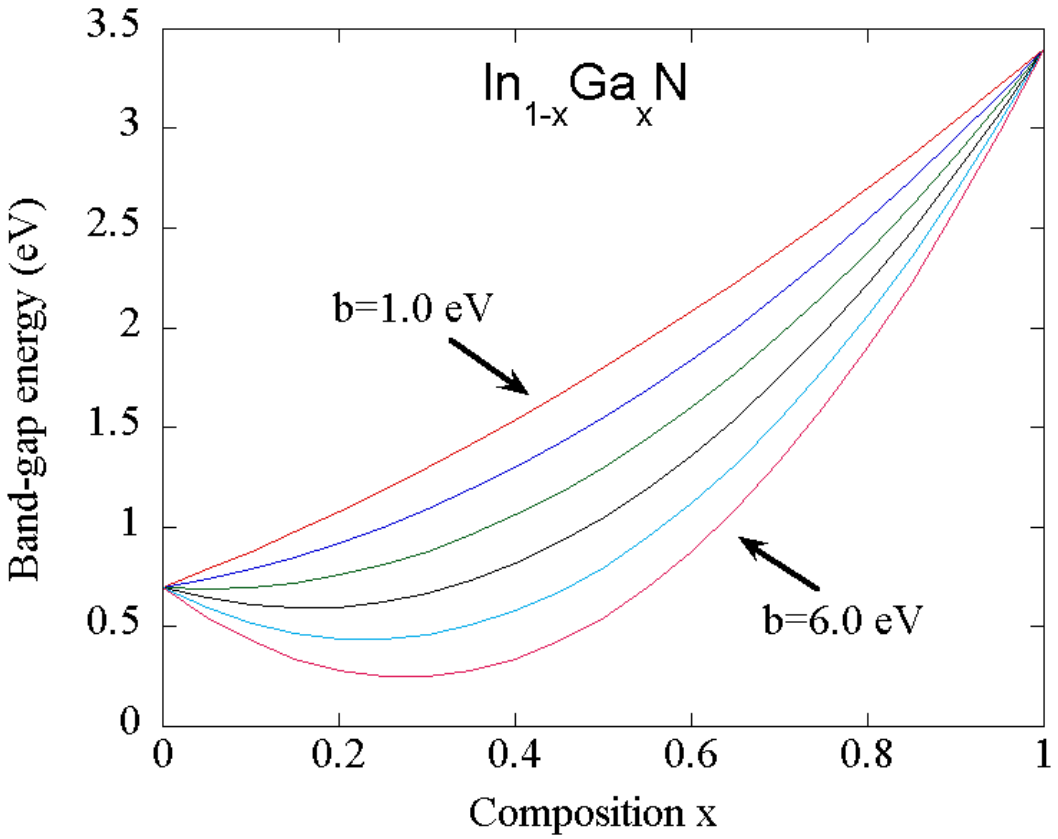

Figure 3.2 The dependence of band-gap of $In_{1-x}Ga_xN$ alloy system on composition x for bowing parameters range (1.0 – 6.0 eV) reported in the literature.

The dependence of the lattice parameters of $In_{1-x}Ga_xN$ system on the composition x can be estimated by linear interpolation between corresponding values of the base binaries InN and

GaN. According to Vegard's law, the relation between $In_{1-x}Ga_xN$ lattice parameters and composition is given by

$$a_o^{(In_{1-x}Ga_xN)} = x \cdot a_o^{(GaN)} + (1-x) \cdot a_o^{(InN)}$$

$$c_o^{(In_{1-x}Ga_xN)} = x \cdot c_o^{(GaN)} + (1-x) \cdot c_o^{(InN)} \qquad (3.2)$$

Although the Vegard's law assumes a linear relationship between the lattice parameters and composition, a careful investigation of dependence of $In_{1-x}Ga_xN$ lattice parameters on composition is required in order to estimate the contribution from crystal distortions.

Alloying the binaries InN and GaN entails sufficient mixing of the members within the same crystal structure. The deviation of this process from ideal mixing conditions (random mixing) results in phase separation[125] generally due to spinodal decomposition. The spatial inhomogeneity in indium atom inclusion in $In_{1-x}Ga_xN$ layers due to spinodal decomposition results in distinct indium-rich and gallium-rich $In_{1-x}Ga_xN$ phases distributed uniformly throughout the film. According to the theoretical calculations[126], the solubility of InN in GaN is less than 6% due to temperature dependent binodal and spinodal decomposition. Another calculation showed that suppression of the phase decomposition would be possible in strained epitaxial layers[127]. There have been several studies in the recent years reporting phase separation in InGaN layers [128-130].

3.1.3 Growth techniques employed for InN, GaN, and InGaN

Presently employed growth techniques for InN, GaN and InGaN growth are Sputtering[131,132] , Metal Organic Chemical Vapor Deposition (MOCVD)[121,122], Molecular Beam Epitaxy (MBE)[118-120], and Hydride Vapor Phase Epitaxy (HVPE)[133,134]. InN growth by Sputtering is processed at very low temperatures and the reported band-gap values are the highest among all available techniques. Even though recent results of InN layers grown by MOCVD and MBE have demonstrated that the growth of high-quality InN layers is possible, the integration of such layers into the wide bandgap group III-nitrides heterostructures is still a challenge due to the low InN disassociation temperature and high equilibrium N_2 vapor pressure over the InN film. The following sections present the currently used techniques for group III-nitride growth.

Molecular beam epitaxy (MBE)

Molecular Beam Epitaxy (MBE) is a growth technique which is used to deposit 'molecular beam' of a source material. An MBE reactor is a modified version of Ultra High Vacuum (UHV) (~10^{-10} Torr) evaporator system [64]. The group III-nitride growth by MBE requires high temperatures for optimal thermal cracking of NH_3 and N_2 – the standard nitrogen sources used in MBE. The breakthrough in the growth of group III-nitride by MBE came with the development of plasma excitation nitrogen sources, using Radio-Frequency (RF) emission or Electron Cyclotron Resonance (ECR). In RF plasma, the effective generation of the reactive nitrogen requires a small aperture size. In the case of an ECR plasma source, the generation rate of reactive atomic nitrogen increases with increasing input microwave power. However, nitrogen ions with energy higher than ~ 60 eV may induce defects in the epitaxial layer. The growth of single phase high quality InN layers by MBE were reported with the band-gap of 0.7eV[67-71].

Reactive indium is provided by effusion cell by temperature adjustments. The growth of InN is processed in the growth temperature regime of 450 to 600 °C; while GaN epilayer growth is is accomplished in the growth temperature regime of 700 to 800 °C. The encountered 200°C difference between the processing temperatures of InN and GaN contributes to the observed difficulties to stabilize embedded indium-rich InGaN heterostructures at optimum growth temperatures.

Metalorganic Chemical Vapor Deposition (MOCVD)

Metalorganic Chemical Vapor Deposition (MOCVD) – also denoted as 'metalorganic vapor phase epitaxy' (MOVPE), 'organometallic chemical vapor deposition' (OMCVD), or 'organometallic vapor phase epitaxy' (OMVPE) - is a chemical vapor phase growth technique where the metal precursors – e.g. group III or group II-elements are transported to the growth surface via organometallic compounds. Organometallic compounds – also denoted as precursors - used in the growth of group III-nitride compound semiconductors are for instance trimethylindium (TMI), trimethylgallium (TMG), or Trimethyaluminum (TMA). The group V precursor is typically ammonia (NH_3). In MOCVD, the growth is driven by chemical reaction processes rather than the kinetic of the molecular beams utilized in MBE. MOCVD is generally used for compound semiconductor growth and is advantageous due to its high throughput, film homogeneity, and its ability to use large wafers as substrate Nitrogen (N_2) and and/or hydrogen (H_2) are commonly used carrier gases to transport the precursors to the reaction region. The growth of InN by low-pressure MOCVD requires typically high V-III ratios ($>10^4$) due to the inefficient cracking of the ammonia precursor at the InN growth temperatures. So far, high defect densities have been observed in InN layers grown by MOCVD. One possible cause is the lack of

lattice-matched substrate material. Sapphire is presently the most suited substrate material choice. Commonly, a GaN buffer layer on sapphire is used to reduce the lattice-mismatch from 22% to 10%. In order to overcome lattice mismatch related growth limitations, various growth techniques have been applied, including Atomic Layer Epitaxy (ALE) and double-zone MOCVD. The suitable growth temperature region for deposition of InN by low-pressure MOCVD is 450-600°C, while it is between 80 °C and 100 °C for the growth of GaN epilayers. In order to integrate indium-rich $In_{1-x}Ga_xN$ layers into gallium-rich InGaN heterostructures, the indium-rich epilayers have to be stabilized at growth temperatures where thermal deposition of the indium-rich epilayers is observed - a server limitation in the fabrication of envisioned device structures.

Hydride Vapor Phase Epitaxy (HVPE)

Hydride Vapor Phase Epitaxy (HVPE) is an epitaxial growth technique that has been used for over four decades to grow group III-nitrides [112]. In HVPE, hot gaseous metal chloride precursors (GaCl, InCl or AlCl) react with NH_3. The metal chlorides are formed by passing HCl gas over group III-metals in a reaction temperatures controlled quartz furnace. HVPE establishes reaction pathways for the growth at the substrate of group III-nitride semiconductor materials. Thick, free-standing GaN substrates with an electron mobility of 1320 cm^2/V sec and a donor concentration of 7.8×10^{15} cm^{-3} have been grown via this method [133,134]. It has been shown that the dislocation density in GaN layers decreases with an increase in layer thickness[134]. As a result, HVPE is an attractive technique for lattice matched growth of thick epilayers. Single crystal InN samples were grown by using an In-Br_2-NH_3-N_2.[135] The growth of InN epitaxial layers by HVPE was also reported using InCl, $InCl_3$ and NH_3 sources[136,137].

Growth using sputtering technique

Sputtering is a thin film growth technique based on ballistic bombardment of reactive species evaporated from solid material by temperature. The rf-sputtering technique is very challenging, since the metal sources In, Ga, and Al are easily oxidized. The first group III-nitride growth by plasma assisted deposition was InN powder in 1910 in which metallic indium reacted with nitrogen by cathodic discharge[138]. The group III-nitride layers grown by sputtering are generally polycrystalline or have columnar morphology limiting material efficiency. Epitaxial InN layers grown by sputtering were reported[139] with less quality of electrical and structural properties compared to those grown by other techniques.

3.2 Nano-scale surface morphology analysis on semiconductors

Scanning Probe Microscopy (SPM) techniques offer the ability of mapping physical properties (topography, conductivity, force, softness, magnetic, capacitance etc.) with nano-scale resolution. SPM techniques extend conventional optical microscopic material characterization to atomic level investigation. The SPM techniques can be applied to different fields of scientific research and industrial processes. A few application areas of SPM in semiconductor research are:

- *high-resolution mapping of the physical properties*
- *nano-scale patterning and etching*
- *microengineering and microfabrication*
- *self-assembly of surface adsorbates and nanomanipulation*
- *nanotribology and nanometrology*

In synthesis of semiconductor layers, epitaxy refers to growth of a layer in a particular crystallographic orientation preferred by the substrate. Epitaxial thin film growth requires production of monocrystalline (single phase) structures with low defect and dislocation density to achieve high performance devices. In order to improve the quality of semiconductor materials, a complete knowledge about the growth path leading to the final product is essential. This path involves physical and chemical processes at growth surface. The characterization of epitaxial layers has generally focused on electrical, optical, and magnetic properties of the final product. Microscopic and nanoscopic level investigation of surface processes at the atomic level is crucial to understand the growth process itself and how it may lead to improved material properties. Growth surface processes such as, adsorption, desorption, and surface diffusion processes are influenced by the interface and surface morphology. Other factors influencing material quality are the defects and the dislocations which can propagate through crystals resulting in interface modification. Since the film surface is the final interface of a growing layer, surface morphology is defined by overall contributions of surface processes, defects and dislocations. Therefore, microscopic investigation of surface morphology reveals information about all these factors affecting macroscopic optical and electrical properties of the layers and is of importance both from technological and academic points of view.

In surface morphology analysis of semiconductors, surface roughness and grain area are important parameters related to surface characteristics and they can be correlated to the structural properties such as, crystallographic orientation and crystalline lattice strain. The surface roughness is the key element controlling the abruptness of the interfaces. In MQW applications of $In_{1-x}Ga_xN$ films, the interface abruptness relates carrier dynamics on diffusive and scattering effects on the interfaces[140]. Manipulation and optimization of the interfacial and surface

properties of the layers can be achieved by evaluating the surface morphological properties and macroscopic properties together. The morphology of the grains in thin films are related to crystal lattice distortion and the electrical mobility of the carriers since the grain boundary potentials introduce the additional resistance against free carriers toward reduced mobility.

The $In_{1-x}Ga_xN$ alloys are the least understood and the most promising among group III-nitride ternary alloys. An improved knowledge about this alloy system can be obtained by investigating the physical and the surface morphological properties of this alloy system and its base binaries and evaluating the findings together. Understanding the correlation between macroscopic material properties and surface morphological properties may lead improved ability to engineer nanoscopic properties in relation to desired material properties. In this research, nanoscopic investigation of surface morphological properties of InN and InGaN surfaces was performed to change experimental conditions (growth temperature, precursor ratios etc.). The findings from the surface morphological analysis were correlated to the results obtained from other characterization techniques (X-Ray diffraction, Raman spectroscopy, optical transmission spectroscopy, and infrared reflectance spectroscopy). The significant aspects of nano-scale surface morphology evaluation for this research are stated below:

- The acquisition of surface morphology information from InN and $In_{1-x}Ga_xN$ layers and its evaluation together with the results of the ex-situ characterization experiments. Raman spectroscopy experiments were performed to analyze crystalline quality and lattice strain analysis and plasmon coupling to the lattice vibrations. X-ray diffraction experiments were carried out to analyze the orientation and the quality of crystal phases and dependence of lattice parameters to the composition x in $In_{1-x}Ga_xN$ layers. Optical

transmission spectroscopy experiments were performed to characterize the optical band-edge dependence on the composition x. The results of infrared reflectance spectroscopy experiments were analyzed to obtain information about dielectric function, film thickness and plasma frequency.

- Analyzing the etching-growth behavior of indium-rich group III-Nitride layers in order to gain insights in the role of grain boundaries or the other extended defects on the electrical and optical properties and correlation of this information to real-time optical characterization data to understand the effects of the different growth parameters in this behavior.
- Analyzing the growth modes of InN and correlating them to the process parameters such as, growth temperature - as well as to the real-time optical monitoring data gathered by laser light scattering. The correlation information is analyzed in order to understand how different growth modes influence the structural, electrical, and optical properties of InN. The related growth parameters to the growth modes are important to engineer embedded or free-standing self-organized nanostructures under HPCVD conditions and control these structures by changing the growth parameters.
- Optimization of InN nucleation at initial stages of growth by employing different growth conditions such as, precursor delivery sequence, precursor ratio, and substrate temperature. The spatial distribution and dimension of the nucleated islands are investigated by AFM.
- Analyzing the effects of different precursor (ammonia) exposure time on the growth rate and the surface morphology of InN layers.

- Understanding the effects of varying composition x of $In_{1-x}Ga_xN$ layers on the surface morphology.
- Analyzing the effects of different precursor ratios and substrate temperatures on surface morphological and electrical properties of $In_{1-x}Ga_xN$ layers in relation to phase stability in these layers.

3.3 Growth and characterization of InGaN layers

This section presents a short introduction on the growth of group III-nitrides by HPCVD and the processing parameter for the InGaN layers investigated in this thesis. It also describes the real-time and ex-situ characterization techniques used, and the numerical techniques applied to analyze the surface morphology results.

3.3.1 High-pressure Chemical Vapor Deposition (HPCVD)

As discussed in section 3.1.3, the encountered limitations in the growth of embedded InGaN layers by low-pressure growth techniques such as, MOCVD and MBE require the exploration of alternative growth techniques that provide the ability to control and stabilize the partial pressures of constituent during the growth process. The approach explored by HPCVD is to utilize the pressure dependency of surface reaction chemistry to stabilize the constituent at higher growth temperatures than possible under low-pressure CVD conditions. The higher growth temperature provides two major advantages; a higher mobility of the constituents at the growth surface, which may lead to better structural properties, and an avenue to narrow the growth temperature window between the binaries InN and GaN and may therefore allow us to stabilize ternary InGaN alloys not stable otherwise. The original motivation to explore HPCVD

stems from the desire to stabilize highly volatile compounds like InN and related alloys[141,142]. Studies in the indium - nitrogen system[143] have shown that much of the uncertainty in the p - T - x relations due to the missing experimental validation[144]. Under thermodynamic equilibrium conditions, the nitrogen pressures required to prevent thermal decomposition of bulk InN is given by the relation[145]

$$p(N_2) \rightarrow p_0 . \exp\left[\frac{\Delta H_r}{R}\left(\frac{1}{T} - \frac{1}{T_0}\right)\right] \tag{3.3}$$

where ΔH_r is the heat of formation, R is the universal gas constant and T is the equilibrium temperature. Solution of Equation 3.2 to AlN, GaN, and InN provides the p-T^{-1} relation illustrated in Figure 3.3. The thermodynamic equilibrium relation is essential for the bulk crystal growth and provides an upper criterion for off-equilibrium conditions utilized in thin film growth techniques. It indicates that in the pressure range $p_{N_2} \leq 10^2$ bar and for substrate temperatures ≤ 900 K the surface decomposition of InN may effectively be suppressed. In view of the higher melting temperature of InN (~1200 °C) as compared to InP (1062 °C), this appears to be a minimum requirement for the growth of high quality epitaxial InN layers and related heterostructures.

The custom-built high-pressure CVD reactor at GSU can be operated at pressure up to 100 bars in order to explore the growth of InN[145-147], an essential step to improve the material quality and for the fabrication of indium rich group III nitride alloys. The details of the HPCVD system have been described elsewhere[148,149].

The HPCVD system is based on a horizontal flow reactor[148,150]. In order to prevent uncontrolled deposition on the opposite site, a symmetrical sample design was chosen. The schematic view and the image of the inner shell of the HPCVD reactor are shown in Figure 3.4. In order to optimize the precursor and carrier gas consumption, a narrow flow channel with a height of 1mm was implemented.

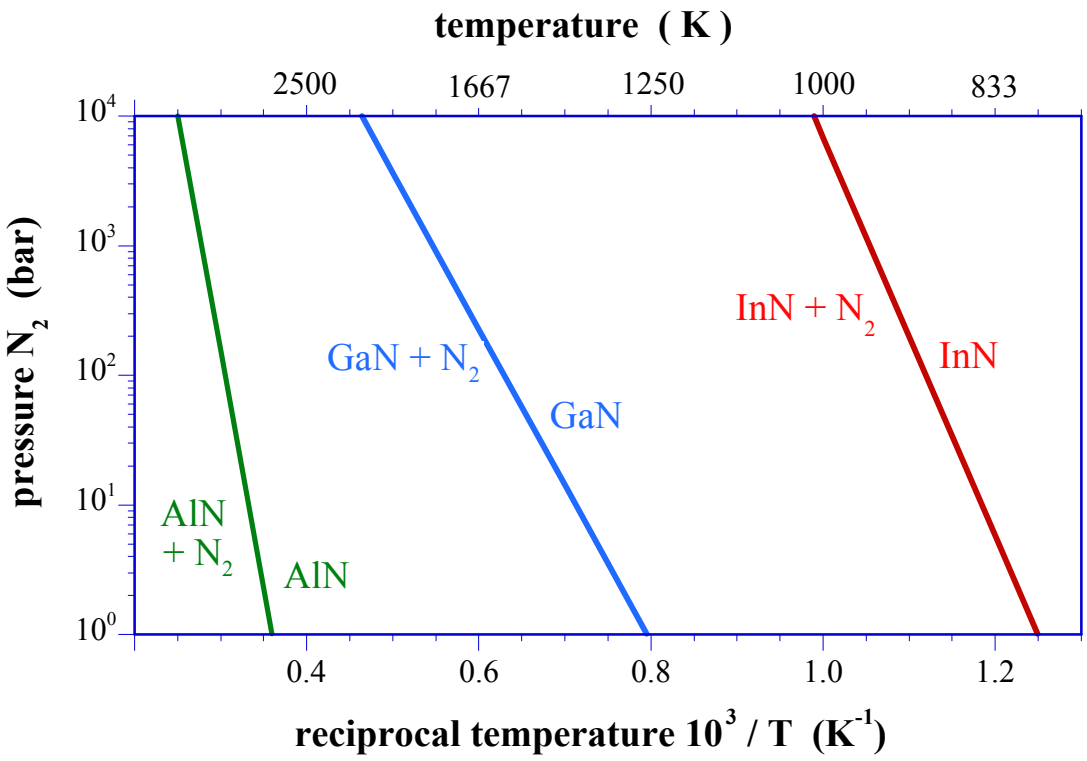

Figure 3. 3 Thermal decomposition pressure vs. reciprocal temperature for AlN, GaN and InN[142].

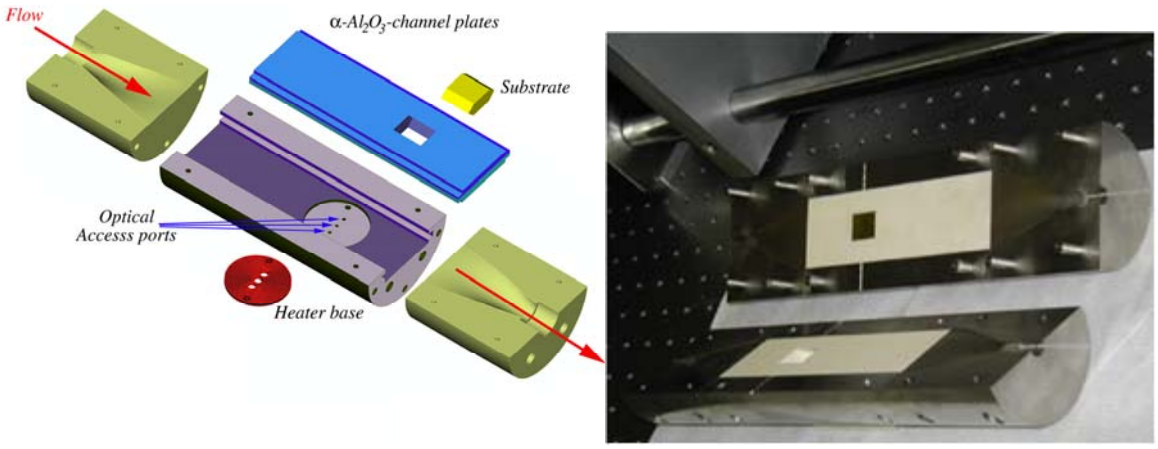

Figure 3.4 a) Schematic view of the HPCVD reactor showing the flow direction and containing the optical access ports, b) image of the assembled HPCVD reactor[151].

The schematic view of inner concentric reactor embedded to outer shell is illustrated in Figure 3.5. The optical access ports are located perpendicular to flow direction. The outer shell is symmetric confirming inlet and outlet optical ports are on-axis. The optical access ports are used for real-time observation of precursor delivery kinetics by Ultraviolet Absorption Spectroscopy (UVAS), evolution of the surface topography by Laser Light Scattering (LLS), and evolution of the growth chemistry by Principal Angle Reflectance Spectroscopy (PARS). The optical access ports used for PARS are located at 28^{o} which is specific to the application[142].

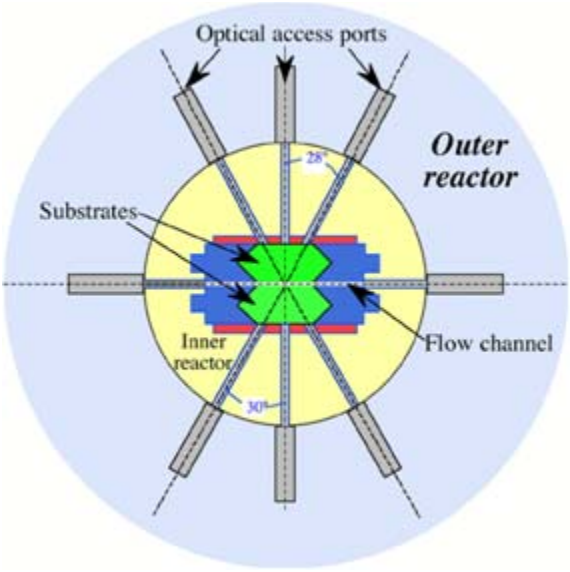

Figure 3. 5 Schematic view of the HPCVD reactor. Two optical ports provide access to the flow channel and three ports in each of the two half sections of the reactor provide access to the growth surface[142].

The InN and $In_{1-x}Ga_xN$ layers investigated in this thesis were all grown at reactor pressure of 15 bar. Under these conditions, the successful growth of InN epilayers[146] at growth temperatures 200°C higher than the possible at low-pressure CVD conditions has been demonstrated.

3.3.2 Growth procedure

The previous section summarized the design and physical construction parameter of the HPCVD system. In this section, details on the growth procedure of InN and InGaN layers are provided. The main issue in HPCVD is the delivery of the sufficient amount of precursors at high-pressures, while avoiding pressure fluctuations during the embedding of the precursors in the high-pressure carrier gas stream. Elements of HPCVD operation are

- compression of the precursors to the reactor pressure and embedding of the precursor pulses in the main carrier flow,
- temporal controlled embedding of the precursors at precise times in order to control the chemical reactions at growth surface,
- verification of the stability of growth temperatures,
- real-time growth monitoring techniques for gas phase and growth surface,

In the growth of InN and InGaN layers explored in this thesis, active indium, gallium, and nitrogen precursor fragments were supplied to growth surface via Trimethylindium (TMI), Trimethylgallium (TMG), and Ammonia (NH_3) precursors, respectively. A schematic representation of the pulsed injection scheme used for precursor delivery is illustrated in Figure 3.6. The NH_3 and (TMI, TMG) injection times were the parameters under investigation. The pulse separation time between the (TMI, TMG) and NH_3 was a further parameter studied. The InGaN layers were grown on GaN/Sapphire(0001) templates or Sapphire (0001) substrates at a reactor pressure of 15 bar and a main gas carrier flow of 12 slm.

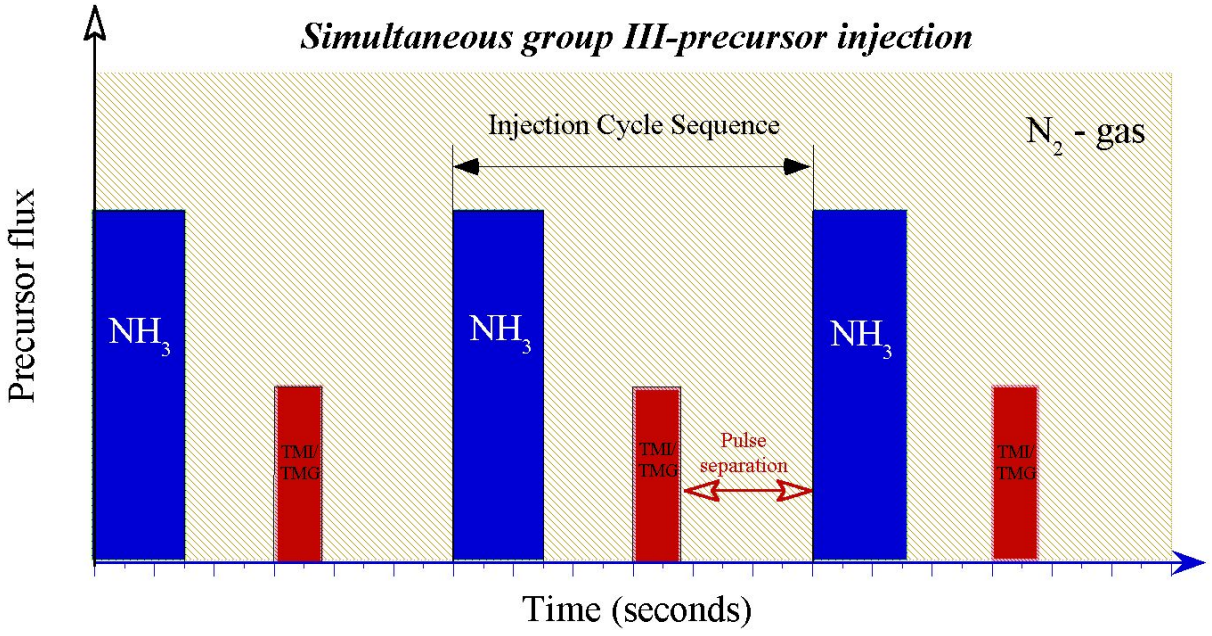

Figure 3. 6 Schematic view of the pulsed injection mode employed for InN and InGaN growth.

3.3.3 Real-time growth monitoring

Understanding the relations between growth surface chemistry and thin film properties requires highly sensitive real-time monitoring techniques. Optical characterization techniques are uniquely suited due to the noninvasive character and their high-sensitive nature to surface and bulk materials properties.

The versatile nature of optical characterization techniques allows the monitoring of specific to molecular vibration modes in the IR or UV wavelength region, the evolution of the dielectric function of the growing layer, as well as the analysis of scattering processes at surfaces/interfaces and the evolution of growth modes.

In the HPCVD system, the gas phase above the growth surface is monitored by Ultraviolet Absorption Spectroscopy (UVAS). The precursors TMI, TMG and NH_3 all have characteristic optical fingerprints in the UV wavelength region. These spectral signatures can be

utilized to identify and track the spatial and temporal evolution of the employed precursors. The evolution of the surface morphology is characterized by Laser Light Scattering (LLS). The change in the angular dependence of the laser signal is function of the roughness of the growth surface. The surface chemistry of the layers is investigated by Principal Angle Reflectance Spectroscopy (PARS). PARS monitors the changes in the reflectance close to the pseudo Brewster angle, which is altered by the growth surface chemistry processes, as well as the overall thin film growth process. In the following section, these techniques are described in more detail.

3.3.3.1 Laser Light Scattering (LLS)

Knowing the real-time evolution of the surface topography provides important information related to the thin film nucleation and growth modes, to potential etching processes, or any deviations of processing conditions. Here, the non-specular scattered PARS laser light is utilized for real-time Laser Light Scattering (LLS). Although, LLS does not provide information on the scale of monolayers, it provides information on evolution of surface roughness on the scale of several tens of injection cycles. The LLS system implemented in the HPCVD system is illustrated in Figure 3.7.

The laser light incidence to surface is 28 deg from the surface normal. For a specular surface, incident photons are expected to be reflected at the same angle as incidence. Any topographical modification at the surface results in off-angle scattering. Here, only light scattered perpendicular to the surface is collected and correlated to changes in the surface topography / roughening. The scattered intensity is acquired by a Photo Multiplier Tube (PMT). The surface roughening in epitaxial film growth can be correlated to the growth mode, the overall surface roughening, and/or etching processes.

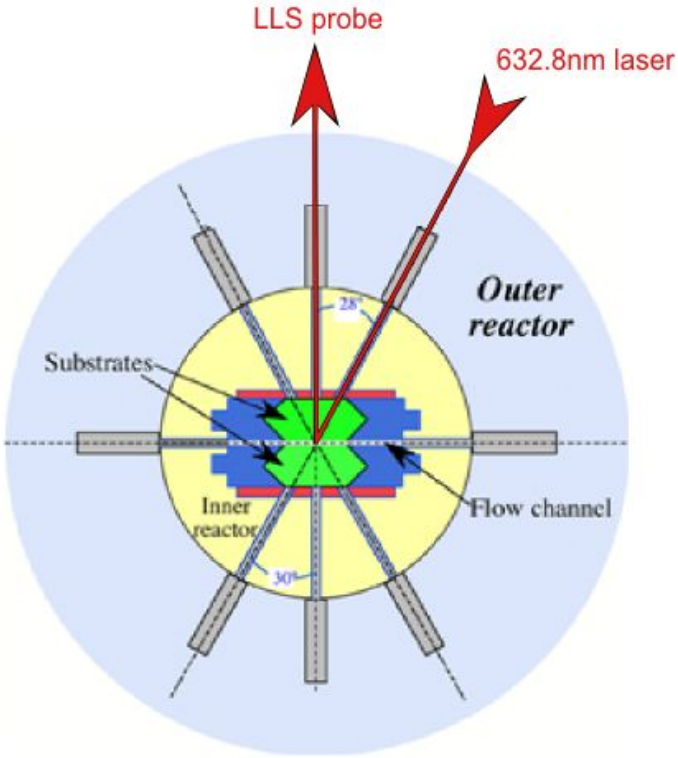

Figure 3. 7 Schematic view of the LLS operation in HPCVD reactor[142].

LLS is a powerful technique to observe surface topographical properties in real-time and relate them to the changes in the surface chemistry during growth.

3.3.3.2 Principal Angle Reflectance Spectroscopy (PARS)

Principal Angle Reflectance Spectroscopy (PARS) utilizes p-polarized laser light impinging the substrate-ambient interface near the pseudo-Brewster angle φ_B and monitors the changes in the reflected intensity. The reflectance behavior in this configuration is illustrated in Figure 3.8. Depending on the substrate temperature and monitoring wavelength, the principal angle φ_P varies from 27.5 deg to 30 deg for the sapphire-ambient interface[143]. The angle of total reflection, φ_T, is approximately 5 deg above φ_P. Both inner half parts of the reactor are identical

to the exception of the angle of incidence for (PARS), which is set to 28 deg and 30 deg for the upper and lower part, respectively, as schematically depicted in Figure 3.9.

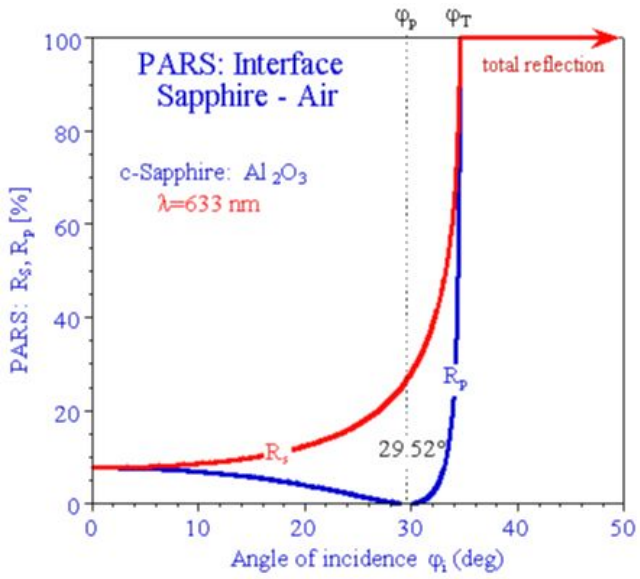

Figure 3.8 Angle dependency of reflectance for p- and s- polarized light at the interface Sapphire-ambient, Depicted are the characteristic angles: principal angle φ_p and total reflection angle φ_T.[142]

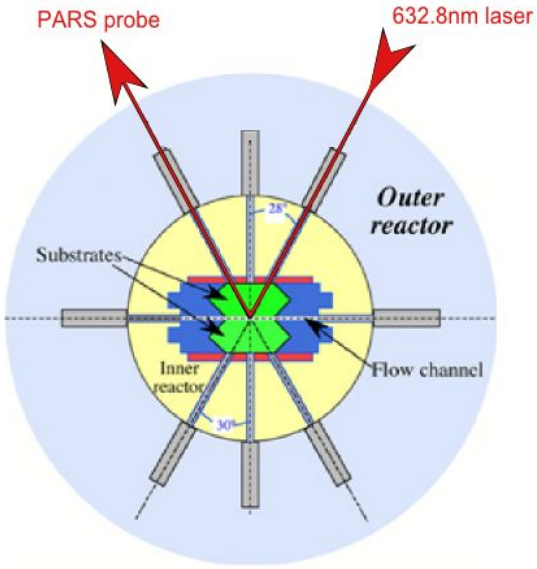

Figure 3. 9 Schematic view of the PARS operation in HPCVD reactor.[142]

The modification of the angle φ_P is a result of deviations at refractive index; thus, the dielectric function of the material[143]. Therefore, the information obtained on PARS is a collective contribution of surface chemistry and surface topography modification since both are involved in the effective medium modulating the dielectric function. In the HPCVD system, PARS is operated with a p-polarized light beam (λ=6328Å) incident to the surface. The scattered intensity is probed at the same angle as incidence, and the signal is detected using a Si photodiode.

The temporal evolution of the PARS trace contains crucial information related to the growth surface and information on the overall layer growth. A typical set of real-time optical monitoring traces by PARS and LLS is illustrated in Figure 3.10. Superimposed on the interference oscillations is a fine structure that is strongly correlated to the time sequence of the supply of precursors employed. From the analysis of the PARS signal, the average growth rate and the difference between the dielectric functions of film and substrate can be estimated. The monitored LLS trace tracks the evolution of the surface morphology, providing details on the nucleation and the overgrowth kinetics as well as the overall surface roughness. As shown in Figure 3.10, the LLS signal increases at the beginning of the growth, but it decreases and becomes smoother during the steady-state growth.

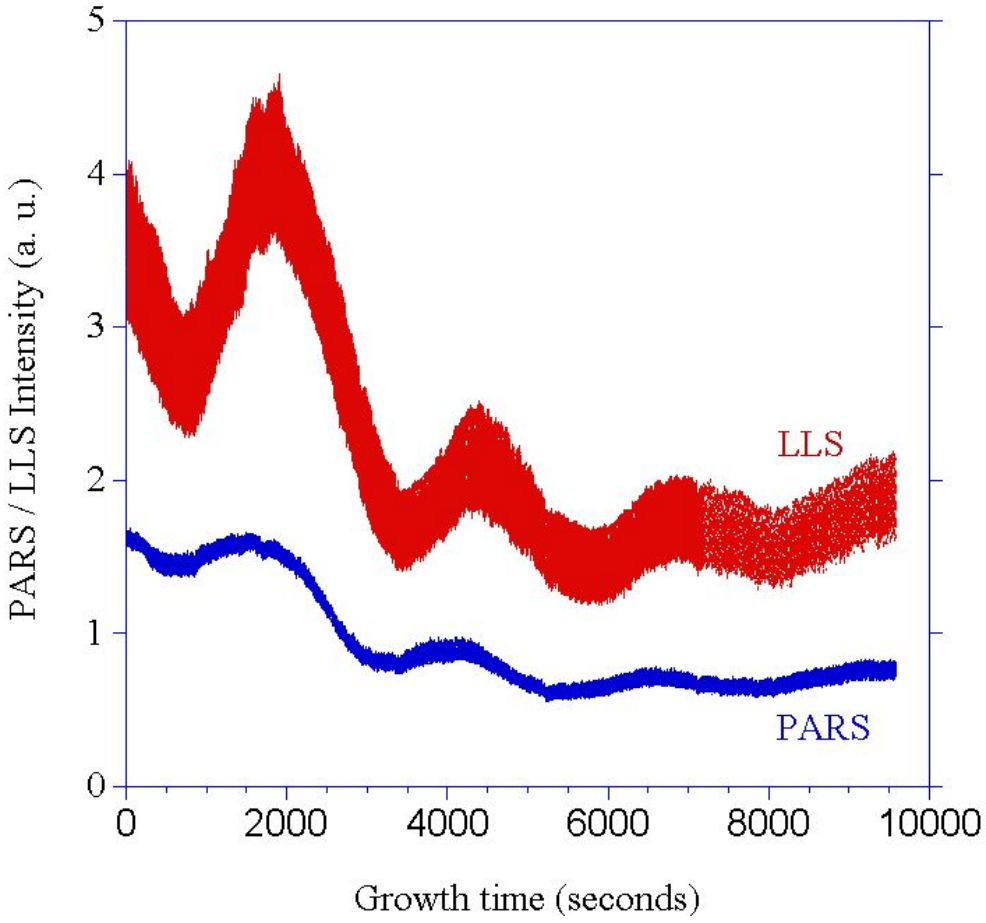

Figure 3. 10 Real time optical monitoring of InN growth by PARS and LLS.

3.3.3.3 Ultra Violet Absorption Spectroscopy (UVAS)

In the HPCVD system, the precursors, TMI, TMG, and ammonia injected into the growth surface are tracked using Ultra Violet Absorption Spectroscopy (UVAS)[143,152]. The reasons why UVAS was chosen are due to limitations of optical probe techniques in the visible and infrared regime, even if modulation techniques are applied. The heater radiation for a 1000K black body emitter vanishes below 350 nm and probe techniques utilizing lower wavelengths are not affected by the heater radiation.

In UVAS, ultraviolet radiation is passed through the growth channel interacting with the precursors in the gas phase (see Figure 3.11). The transmitted intensity is spectrally resolved

recorded and the absorption for each precursor determined. During growth, a characteristic precursor absorption wavelength is chosen/set and recorded as a function of growth time. An optimal wavelength where all three precursors TMI, TMG and NH_3 can be monitored is 221.3 nm [151].

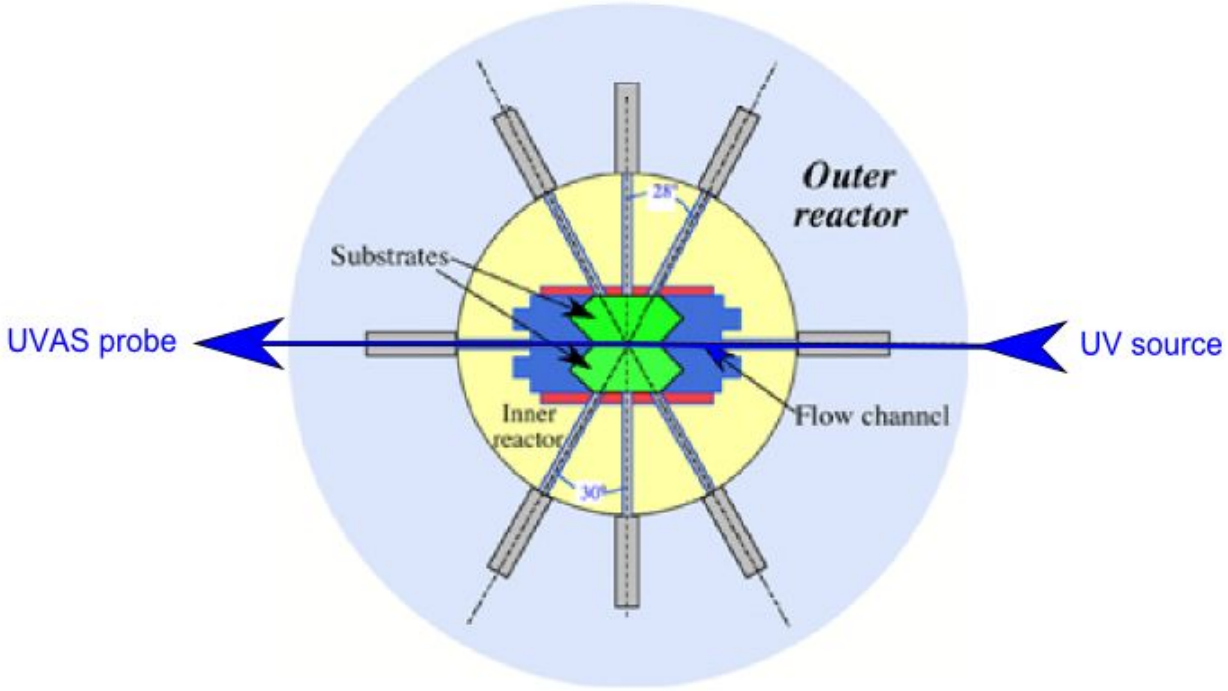

Figure 3. 11 Schematic view of the UVAS operation in HPCVD reactor.[142] The source and probe signal are on-axis and perpendicular to the flow direction.

The UVA traces carry information about arrival time and pulse shape of the precursors. This is of importance to investigate the gas-phase and the growth surface reaction kinetics, which play an important role on the overall physical properties of InN and InGaN layers. For instance, the separation between ammonia and TMI/TMG precursor arrival times relate the time given to the mobile precursor fragments at the growth surface and in potential gas-phase reactions. UVAS and PARS (see 3.3.3.2) provide complementary information to access these relations.

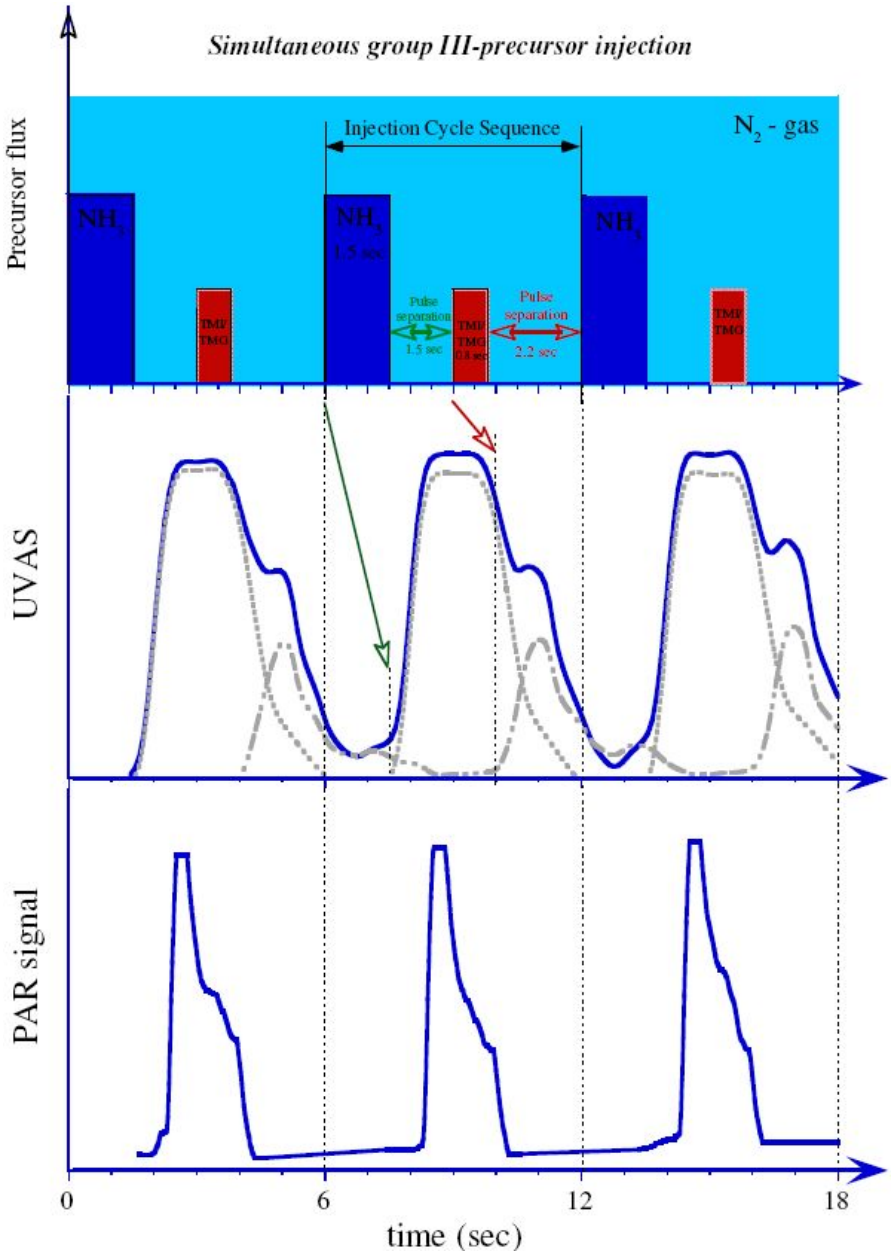

Figure 3. 12 Typical PARS and UVAS traces along with the corresponding injection scheme. Three injection cycles are presented.

Figure 3.12 illustrates typical UVAS and PARS traces together with the corresponding precursor injection sequence. The precursor injection sequence corresponds to the switching pattern at which the precursors are injected in the growth reactor, while the UVA and PAR traces are recorded at the time when the precursors reached the center of the growth surface. The time

difference between the switching action and observation at the center of the growth surface relates to the travel time of the gas-phase precursors. The UVA trace shows the superimposed signal for all the precursors recorded at wavelength λ=221.3nm, as well as the deconvoluted gaussian peak contributions for each precursor injected. The UVA trace provides information on arrival times, the respective amounts of precursors, and the overlapping of individual species at the surface relating to the growth chemistry. The arrival of group III-fragments at the growth surface increases the intensity of PAR signal due to the higher effective dielectric function of the metal-containing fragments and the growth surface. The arrival of the active nitrogen fragments at the growth surface results in a decrease of the effective surface dielectric function and a decrease of the UVA signal. The analysis of the UVA and PAR traces can provide correlations to the growth chemistry per precursor injection sequence as well as to the growth evolution (e.g. thickness, dielectric function) over an extended growth period.

3.3.4 Ex-situ characterization techniques

This section describes the ex-situ characterization techniques utilized to analyze the structural, electrical, and surface morphological properties of InN and InGaN layers.

3.3.4.1 Raman Spectroscopy (RS)

In order to study the structural quality and electrical properties of the InN and InGaN layers, Raman spectroscopy was utilized to analyze the phonon modes in the epilayers. The Raman experiments were carried out using a custom built[153] Raman spectrometer consisting of a McPherson 2062 monochromator, McPherson 275 DS double monochromator. The Raman

experiments were performed in back-scattering geometry (z(xx)$\underline{z}$) using excitation wavelength of 532nm.The Raman spectra were collected using nitrogen cooled CCD array.

Raman spectroscopy is an optical characterization technique for studying lattice vibrations by analyzing the inelastic scattered radiation that is generated during the interaction with the phonons. Vibrational frequencies provide a unique insight on the forces responsible for chemical binding. Therefore, Raman spectroscopy is a powerful technique to identify the crystal type and quality. The inelastic scattering of radiation during its interaction with matter was first described by C. V. Raman in 1928.

The interaction of the electric field of incident radiation with matter leads to exchange of energy in two ways; elastic or inelastic. The elastic scattering of radiation is called Rayleigh scattering. If the interaction is inelastic, the scattering process is called Raman scattering in which the number of photons is as low as one millionth of the Rayleigh photons. The Raman scattering can happen in two ways:

1. *The incident photons can transfer some of their energy to excite molecules into higher vibrational levels resulting in scattered photons of decreased energy, and this process is called Stokes scattering.*
2. *The incident photons can attain some energy from molecular vibrations resulting in scattered photons of increased energy, and this process is called Anti-Stokes scattering.*

Stokes and Anti-Stokes scattering processes in the Raman Effect are illustrated in Figure 3.13. In normal conditions (no external excitation), the energy of a molecular system is

minimized as the lowest vibrational energy level is populated. Consequently, Stokes scattering is more intense since the molecules that are vibrationally excited prior to irradiation can give a rise to the anti-Stokes line.

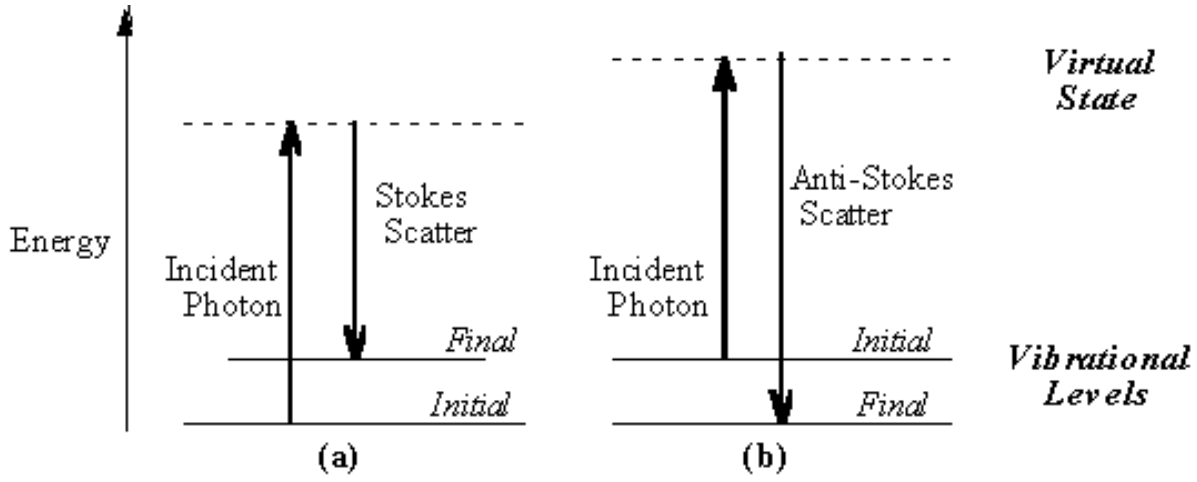

Figure 3. 13 Stoke's and Anti-Stoke's scattering in Raman effect.[192]

Raman spectroscopy is one of the challenging optical spectroscopy techniques in which only inelastically scattered photons are detected among billions of elastically scattered ones. Therefore, instrumentation and sensitivity in detection are very important. The essential components of a Raman spectrometer are given in the following:

- A monochromatic laser light source of very small beam diameter is required. The size of the beam diameter has influence on resolution. The excitation wavelength should be selected by considering fluorescence and resonance effects. The shape of the beam should carefully be investigated since the Raman lines screen the shape of the excitation beam.

- An optical filter is necessary to eliminate the photons which are scattered elastically, and the filter can be a supernotch or a super edge filter.
- A spectrometer is utilized to analyze the spectral behavior of the scattered radiation. A monochromator with high density diffraction grating is the best solution for the spectrometer. The density of grating has influence on resolution. The optical throughput and resolution optimization are the key elements in the Raman spectrometer integration.
- High-sensitivity radiation detection is essential. CCD detector arrays are generally used to optimize the optical integration time in the investigated spectral regime.

According to the group theory, the intensity of the scattered radiation has a non-zero value only for specific polarizations and scattering geometries for specific vibrational orientations. These are known as Raman selection rules, which are essential for determining the crystal symmetry and allowed Raman modes. These selection rules are determined by considering the polarization of incident electric field and if this field is able to induce a change in the polarizability of the oscillation.

InN and InGaN have wurtzite crystal structure with four atoms in the unit cell and belong to C^4_{6v} space group. The character table for C_{6v} is presented in Table 3.3.

Table 3.3 Character table for C_{6v} point group symmetry

D_{2d}	E	$2C_6(z)$	$2C_3(z)$	$2C_2(z)$	$3\sigma_v$	$3\sigma_d$	Linear Functions	Quadratic Functions	Cubic Functions
A_1	+1	+1	+1	+1	+1	+1	z	x^2+y^2,z^2	z^3, $z(x^2+y^2)$
A_2	+1	+1	+1	+1	-1	-1	R_z	-	-
B_1	+1	-1	+1	-1	+1	-1	-	-	$x(x^2-3y^2)$
B_2	+1	-1	+1	-1	-1	+1	z	-	$y(3x^2-y^2)$
E_1	+2	+1	-1	-2	0	0	(x,y) (R_x,R_y)	(xz,yz)	(xz^2,yz^2) $[x(x^2+y^2)$, $y(x^2+y^2)]$
E_2	+2	-1	-1	+2	0	0		(x^2-y^2) , xy)	[xyz, $z(x^2-y^2)$]

The lattice vibrations in a wurtzite crystal system with C_{6v} point group symmetry are characterized by the following irreducible representation[109]:

$$\Gamma_{ac}+\Gamma_{opt}=\left(A_1+E_1\right)+\left(A_1+2B_1+E_1+2E_2\right) \tag{3.3}$$

The character table for the C_{6v} point group symmetry shows that the symmetry of the lattice vibration is classified into non-degenerate A_1, A_2, B_1, and B_2 modes and double degenerate E_1 and E_2. The modes A_1, E_1, and E_2 with the quadratic basis functions are Raman active. The modes A_1, and E_1 with linear basis functions are both Raman and IR active; therefore, they exhibit Longitudinal Optical (LO) and Transverse Optical (TO) splitting. B_1 mode is neither Raman nor IR active, thus, is silent. Consequently, the group III-nitrides may exhibit

six optical phonon modes, E_2(high), E_2(low), E_1(LO), E_1(TO), A_1(TO), and A_1(LO), in the first order Raman spectrum. In Table 3.4, the spectral positions of these Raman active phonons are shown for wurtzite InN and GaN. The modes allowed for a specific scattering configuration are determined by the Raman selection rules.

Table 3. 4 First order Raman active phonon frequencies (cm^{-1}) of hexagonal (wurtzite) GaN and InN at room temperature.

	GaN	InN
E_2(low)	144	87
A_1(TO)	531.8	447
E_1(TO)	558.8	476
E_2(high)	567.6	488
A_1(LO)	734	586
E_1(LO)	741	593
Reference	[109]	[152]

The Raman selection rules are determined by the scattering geometry considering the polarization of incident radiation with respect to the polarity of the lattice vibrations. Table 3.5 shows the Raman selection rules for the wurtzite group III-nitrides. The scattering configuration is given in the Porto notation which is an encoding technique to describe the configuration of the directions and polarizations of the incident and scattered radiation. For instance, in z(x,y)$\underline{z}$, z is the direction of incident radiation, x is the polarization direction of the incident light, y is the polarization direction of the scattered light, and $\underline{z}$ is the direction of the scattered light.

Table 3. 5 Raman selection rules for hexagonal group III-nitrides[109]

Configuration	Allowed Mode
$z(x,x)\bar{z}$	A_1(LO), E_2(low), E_2(high)
$z(x,y)\bar{z}$	E_2(low), E_2(high)
$x(z,z)\bar{x}$	A_1(LO)
$x(y,y)\bar{x}$	A_1(LO), E_2(low), E_2(high)
$x(z,y)\bar{x}$	E_1(TO)
$x(y,z)\bar{x}$	E_1(TO), E_1(LO)

Besides wurtzite, the group-III nitrides can also crystallize in zincblende (cubic) structure whichhas F$\underline{4}$3m T_d^2 point group symmetry. In the cubic crystal symmetry, only one lattice vibration is allowed in Raman spectrum and splits into LO and TO components[154]. In Table 3.6, the spectral positions of these phonon components are shown for cubic InN and GaN.

Table 3. 6 First order Raman active phonon frequencies (cm^{-1}) of cubic (zincblende) GaN and InN at room temperature.

	GaN	InN
TO	555	472
LO	742	586
Reference	[151]	[152]

Whether the crystal structure is wurtzite or zincblende, the phonon modes in the group III-nitrides are sensitive to compositional fluctuations, and crystal strain due to defect incorporation. As a result, the corresponding Raman lines exhibit shifted spectral positions, and modified line-shapes.

This study focuses on Raman spectroscopic analyses of wurtzite InN, and InGaN in the backscattering geometry z(xx)$\underline{z}$. In this scattering configuration, A_1(LO), E_2(low), and E_2(high) phonon modes are allowed according to the Raman selection rules. The high-energy split of the E_2 phonons, E_2(high), is sensitive to crystalline strain which modifies the line-shape and the spectral position. Therefore, this phonon mode can be used to characterize the local crystalline quality of the InN and InGaN layers. The phonons in the InGaN crystal are expected to obey one-mode behavior[155] in which the positions of the Raman lines alternates between its corresponding values for InN and GaN linearly as a function of the composition. For instance, E_2 (high) phonon mode is observed at 567 and 488 cm^{-1} for GaN and InN, respectively. Then, the E_2 (high) mode of $In_{0.5}Ga_{0.5}N$ is expected to be positioned at 527.5 cm^{-1}. Although there are reports[155] showing one-mode behaviors of phonon modes of InGaN, it requires more studies on unstrained and intrinsic layers.

Corresponding Raman line of the longitudinal split of the A_1 phonons, $A_1(LO)$, is also expected to be modified by crystalline strain, however, the polar nature of this line results in additional contributions from coupling to plasmons broadening the spectral line-shape. This coupling between the $A_1(LO)$ phonon mode and plasma oscillations is advantageous to estimate the free carrier concentration in InN and InGaN layers[156].

Calculation of free carrier concentration from $A_1(LO)$ phonon mode

In Raman scattering, plasmon coupling to LO phonon modes results in the line-shape broadening. This coupling is due to the longitudinal macroscopic electric field components of LO phonons. As a result of the plasmon-phonon coupling, two coupled modes (LPP^- and LPP^+) are expected to appear in the Raman spectrum, however, they have not been observed yet.

The line-shape broadening of the $A_1(LO)$ phonon mode can be used to estimate free electron concentration in InN layers[156]. In order to do this, a model dielectric function is usedto simulate the experimental $A_1(LO)$ Raman line. The most general expression for the dielectric function is given by

$$\varepsilon(q,\omega) = \varepsilon_\infty + \varepsilon_c + \varepsilon_e \tag{3.4}$$

where ε_∞, ε_c, and ε_e are the high frequency dielectric constant, the phonon and plasma contributions, respectively. The dielectric function model based on the classical Drude approach doesn't take electron-electron interaction into account; so, the dielectric function can be expressed as

$$\varepsilon(q,\omega) = \varepsilon_\infty \cdot \left(1 + \frac{\omega_{LO}^2 - \omega_{TO}^2}{\omega_{TO}^2 - \omega^2 - i\omega\Gamma} - \frac{\omega_p^2(q)}{\omega^2 + i\omega\gamma_p} \right) \tag{3.5}$$

where ω_{LO} and ω_{TO} are the oscillation frequencies of LO and TO phonon modes, respectively, Γ is the broadening parameter and γ_p is the collision frequency of free carriers. At the small wave-vector limit, plasma frequency, ω_p, can be expressed as

$$\omega_p^2(q) = \omega_p^2 + \frac{3}{5} q^2 \cdot v_f^2 \tag{3.6}$$

$$v_f = \frac{\hbar}{m^*} (3 \cdot \pi^2 \cdot n)^{1/3} \tag{3.7}$$

where v_f is the velocity of the Fermi electrons, m* is the effective electron mass and n is the free electron concentration.

The dielectric function based on the Lindhard-Mermin approach takes the conservation of the local electron density into account..In Lindhard-Mermin approach, the dielectric function is given by[157]

$$\varepsilon_e(q,\omega) = \varepsilon_\infty \frac{(1 + i/\tau \cdot \omega)[\chi_e^0(q, \omega + i/\tau) - 1]}{1 + (i/\omega \cdot \tau)\{[\chi_e^0(q, \omega + i/\tau) - 1]/[\chi_e^0(q,0) - 1]\}} \tag{3.8}$$

where the time dependent Lindhard susceptibility is given as[158]

$$\chi_e^0(q,\omega) = \frac{e^2}{2 \cdot \pi^3 \cdot q^2} \int_V f(E_f, T, k) \frac{E(q+k) - E(k)}{[E(q+k) - E(k)]^2 - (\hbar \cdot \omega)^2} \tag{3.9}$$

which includes the Fermi distribution and the Fermi energy of the electron gas at a specific temperature.

In a polar crystal, the light scattering mechanism depends on the lattice configuration, the charge density, and the band structure of the material. The lattice configuration induces the Deformation Potential by allowed Electro-Optics (DPEO) scattering mechanism in which the atomic displacement introduces elastic strain while the effective mass is unchanged. The charge density effect induces the Charge Density Fluctuations (CDF) scattering mechanism in which the scattered light is configured by the charge density fluctuations of free electrons. The band structure of the material induces the Impurity Induced Froclich (IIF) scattering mechanism in which the electron or hole is scattered within the same band by the macroscopic electric field of the LO phonon.

The Raman intensity of the scattered light can be calculated by integrating the spectral line shape function up to a maximum wave-vector limit with a weight factor function of Yukawa type impurity potential. The Raman intensity can be expressed as

$$I(\omega) = \int_0^{q_{max}} W(q) \cdot L(q,\omega) \cdot dq \tag{3.10}$$

$$W(q) = \left(\frac{4 \cdot \pi}{q^2 + q_{TF}^2} \right)^2 \tag{3.11}$$

where q_{TF} is the Thomas-Fermi screening wave-vector which is expressed as

$$q_{TF}^2 = \frac{6 \cdot \pi \cdot n \cdot e^2}{E_F \cdot \varepsilon_\infty} \tag{3.12}$$

The spectral line shape function is the product of a scattering factor S(ω) and the imaginary part of the negative of the inverse dielectric function.

$$L(\omega) = S(\omega) \cdot \mathrm{Im}\left[-\frac{1}{\varepsilon(q,\omega)} \right] \tag{3.13}$$

S(ω) for the DPEO scattering mechanism is

$$\begin{aligned} S(\omega) = 1 + 2 \cdot C \cdot \frac{\omega_{TO}^2}{\Delta}\left[\omega^2 \cdot \gamma_p \cdot \left(\omega_{TO}^2 - \omega^2 \right) + \omega^2 \cdot \Gamma \cdot \left(\omega_p^2 - \gamma_p^2 - \omega^2 \right) \right] \\ + C^2 \cdot \frac{\omega_{TO}^4}{\Delta} \cdot \frac{\omega_p^2}{\Omega^2}\left[\gamma_p \cdot \Omega^2 + \Gamma \cdot \left(\omega_p^2 - 2\omega^2 \right) \right] + \omega^2 \cdot \Gamma \cdot \left(\omega^2 + \gamma_p^2 \right) \end{aligned} \tag{3.14}$$

$$\Delta = \omega_p^2 \cdot \gamma_p \cdot \left[\left(\omega_{TO}^2 - \omega^2 \right)^2 + \omega^2 \cdot \Gamma^2 \right] + \omega^2 \cdot \Gamma \cdot \left(\omega^2 + \gamma^2 \right) \tag{3.15}$$

$$\Omega^2 = \omega_L^2 - \omega_L^2 \tag{3.16}$$

where C is the first Faust-Henry coefficient. S(ω) for the CDF scattering mechanism is

$$\begin{aligned} S(\omega) = q^2 \cdot \left[\frac{\omega_p^2}{\Delta} \cdot \gamma_p \cdot \left(\omega_{LO}^2 - \omega^2 \right)^2 + \omega^2 \cdot \Gamma^2 \right] \\ + \omega^2 \cdot \Gamma \cdot \Omega^2 \cdot \left(\omega^2 + \gamma_p^2 \right) \end{aligned} \tag{3.17}$$

and S(ω) for the IIF scattering mechanism is

$$S(\omega) = q^2 \tag{3.18}$$

In this analysis, the free carrier concentration is the input for the simulation routine based on the theory described above. The free carrier concentration is varied until the best Lorentzian type peak fit to the experimental A_1(LO) peak is obtained. The Raman intensity is calculated by iterating Lindhard susceptibility triple integral in the intensity integral. Execution time of the program is optimized by adjusting the size of integration steps and the integration method.

3.3.4.2 Infrared Reflectance (IR) spectroscopy

The film thickness, the plasma frequency, and the free carrier concentration of the InN and the InGaN layers have been analyzed using Infrared Reflectance Spectroscopy (IRS). The IRS experiments were performed in the reflection mode using the Perkin Elmer System 2000 Fourier transform infrared spectrometer with Graseby reflection accessories. A Mercury Cadmium Telluride (MCT) detector was used for the short wavelength (1.5-20 μm) range and TGS based pyroelectric detector was used for long wavelength (<50 μm) range.

IRS analysis of InN and InGaN involves the utilization of both elastic and inelastic scattering components of infrared radiation-sample interaction. The inelastic component is due to the interaction between the phonons and the radiation. The elastic component of the interaction is utilized using ray optics.

A major advantage of the IRS is that it can be used to determine the plasma frequency since the radiation having smaller frequency than plasma frequency results in the increased reflectance. At smaller frequencies than the plasma frequency, interference of the infrared radiation reflected from the film surface and the film-template interface results in oscillations in the reflectance signal. The frequency of this oscillation is related to the optical path difference

introduced by the travel time of the radiation through the film. This travel time depends on the film thickness and the dielectric constant of the film. So, from interference oscillations, it is possible to calculate the film thickness for a known dielectric constant. This calculation is performed employing a simulation routine with the theory described in the following.

Calculation of the structural and the electrical properties of the group III-nitrides using IRS analysis

The experimental IRS results are simulated by using a model dielectric function in order to characterize the phonon and the plasmon properties, the carrier concentrations, the carrier mobility, the layer thickness, and the interface behavior[159]. The model dielectric function consists of the high frequency dielectric constant (ε_∞), and plasmon and phonon contributions which can be expressed as

$$\varepsilon = \varepsilon(\omega) = \varepsilon_\infty + \sum_i \frac{S_i \cdot \left(\omega_{TO}^2 - \omega_{LO}^2\right)}{\omega_{TO}^2 - \omega^2 - i \cdot \omega \cdot \Gamma} - \frac{\varepsilon_\infty \cdot \omega_p^2}{\omega^2 + i \cdot \omega \cdot \gamma_p} \qquad (3.19)$$

where γ_p is the electron damping due to the scattering from randomly distributed stationary impurities, ω_p is the plasma frequency, ω_{TO}, ω_{LO}, Γ, S_i are the TO and LO phonon frequencies, the damping and the strength of i^{th} oscillator, respectively.

The light propagation through a multilayer stack is modeled using the Transfer Matrix Method[160,161]. Reflectivity can be calculated by solving the Maxwell equations for plane electromagnetic waves with boundary conditions of electric/magnetic field components at the air/film and the film/substrate interfaces. There are two waves with the electric-field amplitudes

E^+ and E^- propagating in the opposite directions in each layer. Suppose '0' refers to air, '1' to the film, and '2' to the substrate, respectively. The transfer matrix M_r can be expressed as

$$M_r = M_{01} \cdot M_1 \cdot M_{12} \tag{3.20}$$

The interface matrix between the j^{th} and $(j+1)^{th}$ layers has the from

$$M_{j,j+1} = \frac{1}{2 \cdot \sqrt{\varepsilon_{j+1}}} \begin{pmatrix} \sqrt{\varepsilon_{j+1}} + \sqrt{\varepsilon_j} & \sqrt{\varepsilon_{j+1}} - \sqrt{\varepsilon_j} \\ \sqrt{\varepsilon_{j+1}} - \sqrt{\varepsilon_j} & \sqrt{\varepsilon_{j+1}} + \sqrt{\varepsilon_j} \end{pmatrix} \tag{3.21}$$

and the propagation matrix for the film of thickness d can be written as

$$M_1 = \begin{pmatrix} \exp(i2\pi\sqrt{\varepsilon}d/\lambda & 0 \\ 0 & \exp(-i2\pi\sqrt{\varepsilon}d/\lambda \end{pmatrix} \tag{3.22}$$

where λ is the wavelength of the incident radiation. Then, the reflectance R can be written as

$$R = \left| \frac{M_{r1,0}}{M_{r1,1}} \right|^2 \tag{3.23}$$

Employing the transfer matrix model described above, the best fitting parameters for the layers are obtained using the nonlinear Levenberg-Marquart fitting algorithm. The theory and the application of IR reflectance spectroscopy simulations have been detailed extensively elsewhere[159].

3.3.4.3 X-Ray Diffraction (XRD)

A crystal is a three-dimensional distribution of atoms in an ordered manner (wurtzite, zincblende etc.). As a result of this arrangement, parallel planes of the atoms are formed and the separation between these planes is a result of lattice configuration. The spacing between these crystallographic planes is in the order A^o. X-rays are the most suitable radiation to analyze the crystallographic planes since their wavelengths have close matches to lattice spacing. Diffraction of the x-rays from the crystallographic planes exhibits interference maxima peaks only at some specific incidence angles depending on the orientations of the planes investigated. According to Bragg's law, the diffraction of the waves from a lattice plane is given as the following

$$n \cdot \lambda = 2 \cdot d \cdot \sin\theta \tag{3.24}$$

where n is the diffraction order, λ is the wavelength of the x-ray, 2dsinθ is the path difference resulting in this diffraction. All these parameters are shown in the illustration of XRD operation (see Figure 3.14).

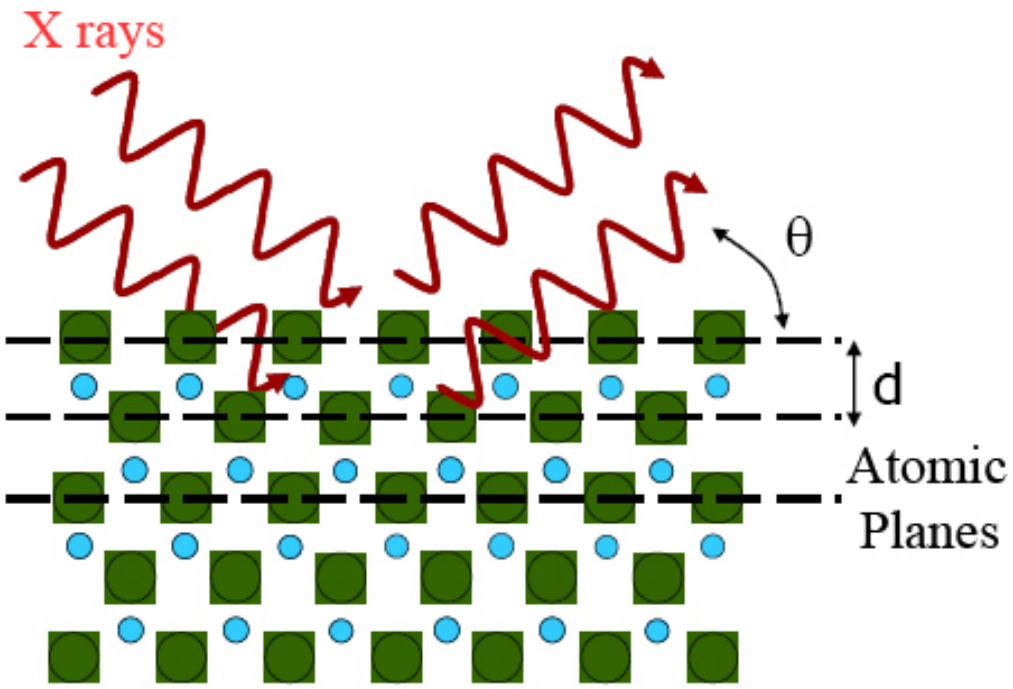

Figure 3. 14 Schematic illustration of X-ray diffraction from lattice planes of a crystal [162].

In XRD analysis of the InN layers, the Full Width Half Maximum (FWHM) of the Bragg reflection peak from (0002) plane of the wurtzite crystal has been investigated. The 2-θ position of this reflection is 31.3^{o} for relaxed wurtzite InN. Increased compressive strain in InN could change the lattice parameters along c-axes shifting the spectral position and broadening the spectral line-shape of this reflection. Therefore, the position and FWHM of (0002) Bragg reflection peak can be used to investigate the crystalline quality. Different from the Raman spectroscopy, where the probing size is on the μm order, the probing size of XRD is at mm order.

The spectral position of the InGaN (0002) Bragg reflection has been used to calculate the lattice parameters by using the equations 3.24 and 3.25 which is given as[31]

$$\frac{1}{d_{hkl}^2} = \frac{4}{3}\frac{h^2 + k^2 + hk}{a^2} + \frac{l^2}{c^2} \tag{3.25}$$

where a and c are the lattice parameters of the wurtzite crystal, d is the planar spacing, and h,k,l are the Miller indices of the reflection plane. According to the Vegard's law (see section 3.1.2), in InGaN, the lattice parameters a and c are located between the binary end members (InN and GaN) and both shift linearly with changing alloy composition. The lattice parameters for InN and GaN are given in Table 3.1 and Table 3.2, respectively.

In this research, the FWHM of the InGaN (0002) Bragg reflection peak has been used to investigate the crystal strain in InGaN layers. The crystalline strain effect might also shift the spectral position of this Bragg reflection. As a result, the shift in the spectral position of InGaN (0002) Bragg reflection is due to the contributions from the strain effect and the composition. Since the contribution from the strain effect is relatively low compared to that of the composition, the shift in the spectral position has been assumed completely due to the composition and the strain effect has been kept within the error margin provided in the compositional analyses of InGaN layers.

XRD experiments were performed by a Philips X`pet MRD-pro 4-circle diffractometer with a monochromatized CuKα x-ray source. The statistical properties of the Bragg reflection peaks, the FWHM and the spectral position, were determined using peak fitting [163].

3.4 Results and discussion

The results of the ex-situ and real-time characterization experiments performed on InN and InGaN layers grown by high-pressure CVD are presented in this section.

3.4.1 Indium Nitride (InN) layers

The results of surface morphological studies on InN layers are reported in this section. These results have been correlated to the results obtained from the real-time optical characterization tools and ex-situ characterization experiments.

3.4.1.1 Surface morphology versus crystallographic planes

The influence of different templates on crystallographic and surface morphological properties of InN layers has been investigated. InN layers were grown on Sapphire (0001) and GaN/Sapphire (0001) templates which had different lattice mismatch to InN. The lattice mismatch between InN and Sapphire is about 18% while it is about 11% between InN and GaN.

In Figure 3.15, the correlation between surface roughness and FWHM of (0002) Bragg reflection is presented. For InN layers grown on both types of templates, a similar behavior is observed in which the broadening in XRD (0002) reflection peak results in higher surface roughness. The dashed ellipse encloses the most of the InN layers grown on GaN/Sapphire (0001) templates. The samples having single InN phase are marked with arrow. Although there are some samples grown on GaN/Sapphire (0001) templates (outside of the dashed ellipse) with respectively lower surface roughness, the general tendency is that the samples grown on GaN/Sapphire (0001) templates have higher surface roughness than the ones grown on Sapphire (0001) for a similar FWHM of (0002) Bragg reflex peak. All samples within the dashed ellipse have double InN phase on the XRD pattern.

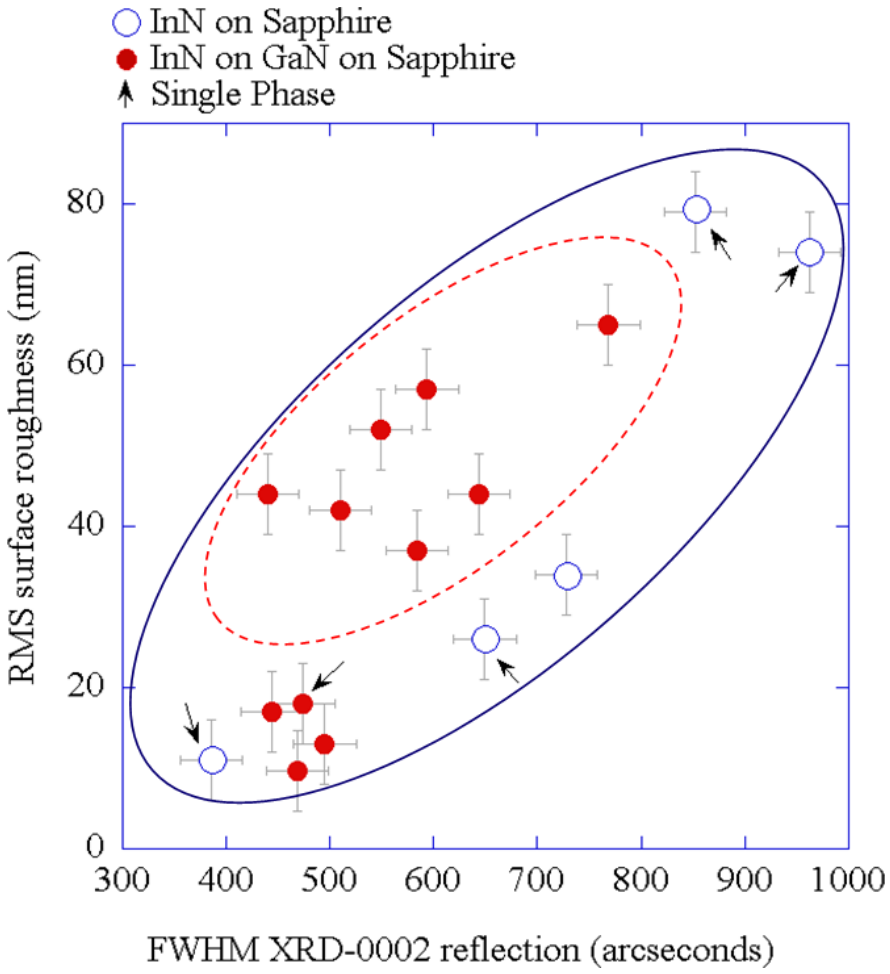

Figure 3.15 InN surface roughness versus FWHM of (0002) Bragg reflection peak for samples grown on GaN/Sapphire(0001) and Sapphire(0001) templates.

The correlation between the average grain area and the FWHM of (0002) Bragg reflection peak is shown in Figure 3.16. The samples exhibiting material decomposition at surface are marked with asterisk. There is a rough correlation between average grain area and FWHM of (0002) Bragg reflection peak. However, this correlation is highly affected by material decomposition decreasing the average grain area. The material decomposition is more dominant at the surface of the InN layers grown GaN/Sapphire (0001) templates despite the fact that they have sharper (0002) reflection peak than their counterparts grown on Sapphire (0001) templates.

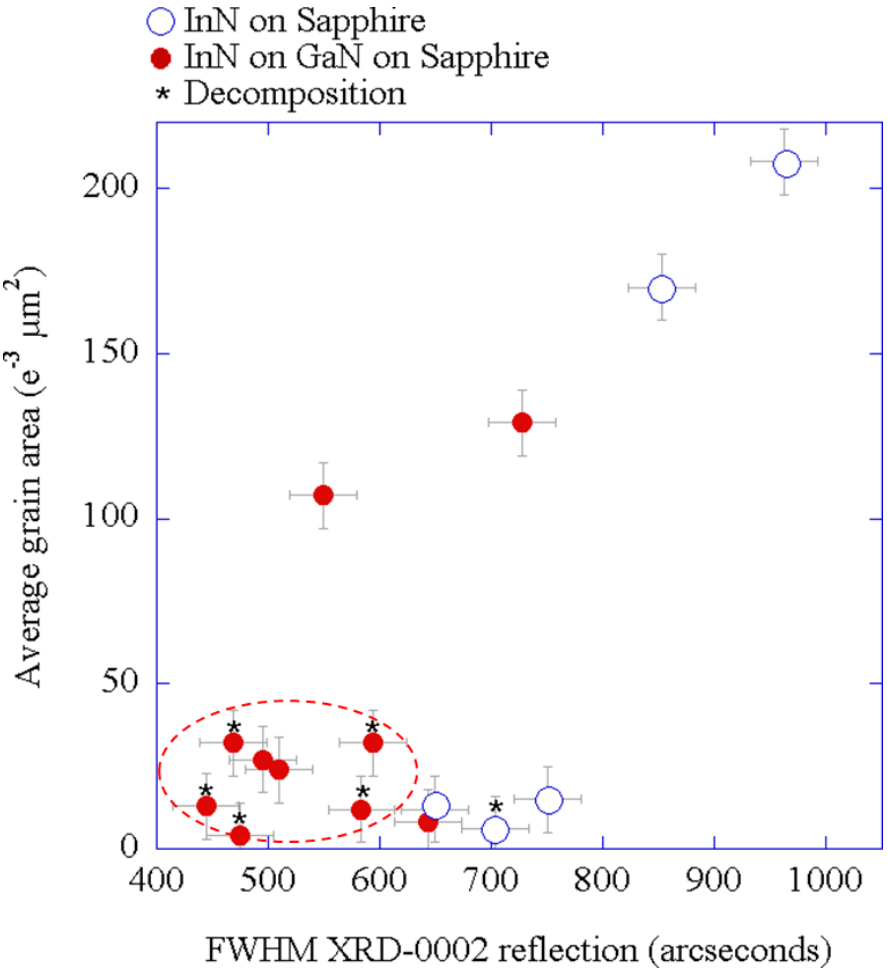

Figure 3.16 InN average grain area versus FWHM of (0002) Bragg reflection peak for samples grown on GaN/Sapphire(0001) and Sapphire(0001) templates.

The broadening of InN (0002) Bragg reflection peak in XRD pattern is a measure of how good the reflection plane is arranged at long range order (~mm). The degradation in the long range ordering along InN (0002) plane resulted in line-shape broadening in the corresponding XRD peak. The InN layers grown on Sapphire (0001) templates generally exhibited larger broadening in the XRD (0002) reflection line-shape than the ones grown on GaN/Sapphire (0001) templates due to higher lattice mismatch which degrades long range atomic ordering along (0002) plane more. The InN layers grown on GaN/Sapphire (0001) showed higher inclusion of the second InN phase (0101) exhibiting increased surface roughness and increased

long range ordering along (0002) plane of InN. These layers enclosed by the dashed ellipse in Figure 3.16 exhibited surface material decomposition more than their counterparts grown on Sapphire (0001) templates. In the next section, the correlation between the surface morphological properties and phonon dynamics of the same layers is discussed.

3.4.1.2 Surface morphology versus phonon dynamics

The phonon dynamics and surface morphological properties of InN layers grown on GaN/Sapphire (0001) and Sapphire (0001) templates have been studied. Surface roughness and average grain area of InN layers have been correlated to the broadening in the line-shape of E_2(high) Raman line.

In Figure 3.17, the correlation between surface roughness and FWHM of E_2(high) Raman line of InN layer grown on different templates is shown. The InN layers having single phase are marked by black arrow. The layers grown on GaN/Sapphire (0001) templates were populated in low the FWHM region of the E_2(high) Raman line although they spanned a wide region of surface roughness depending on inclusion of the second InN phase as discussed in the previous section. Single phase InN layers grown on Sapphire (0001) templates exhibited a broadening in the line-shape of E_2(high) Raman line and high surface roughness. Although some InN layers grown on Sapphire (0001) templates exhibited sharper E_2(high) Raman line, their surface roughness was higher than the ones grown on GaN/Sapphire (0001) templates.

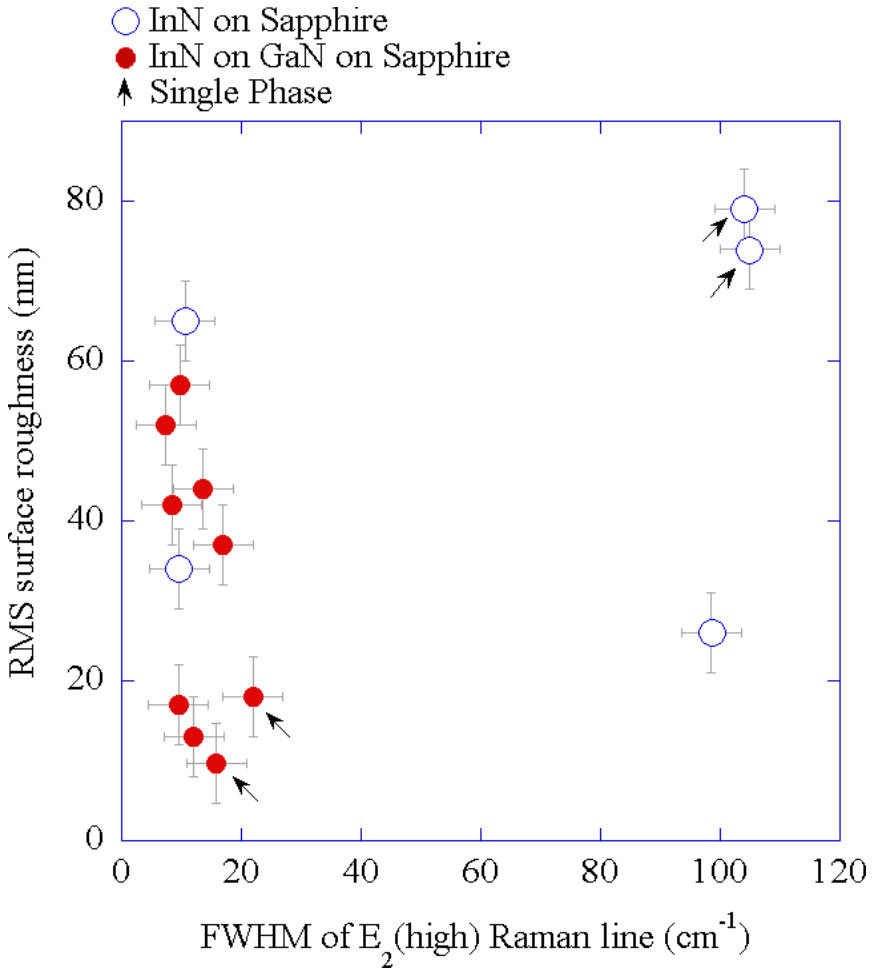

Figure 3.17 RMS surface roughness versus FWHM of E_2(high) Raman line of InN layers grown on GaN/Sapphire(0001) and Sapphire(0001) templates.

The correlation between average grain area and FWHM of E_2(high) Raman line is shown in Figure 3.18. The InN layers exhibiting material decomposition on the surface are marked with asterisk. The InN layers grown on GaN/Sapphire (0001) templates were populated in low the FWHM of E_2(high) Raman line. The grain area was affected by material decomposition at surface especially for the layers grown on GaN/Sapphire (0001) templates.

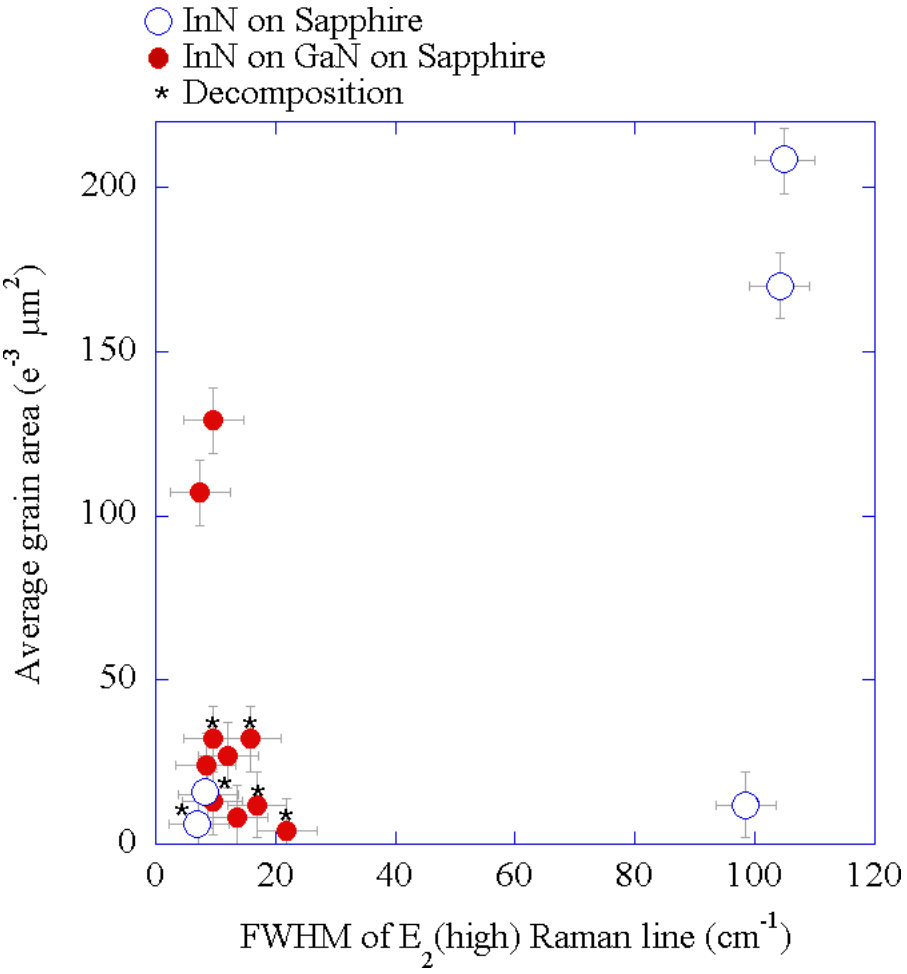

Figure 3.18 Average grain area versus FWHM of E_2(high) Raman line of InN layers grown on GaN/Sapphire(0001) and Sapphire(0001) templates.

The lattice oscillations are sensitive to crystal distortion due to strain effect; therefore, the broadening in the observed line-shape of a phonon mode in Raman spectrum refers to reduced crystalline quality. In order to investigate the quality of InN crystal, the most suitable phonon mode is E_2(high) because it doesn't couple to other vibrational modes and is not affected by plasma oscillations but the crystalline quality. The broadening in the line-shape of E_2(high) phonons in Raman spectrum of wurtzite InN is the indicator of crystalline quality at short range orders (~μm) dictated by the beam diameter of Raman excitation. The InN layers grown on GaN/Sapphire (0001) templates exhibited higher crystalline quality at local range than the ones

grown on Sapphire (0001) templates. This was due to the higher lattice mismatch between Sapphire and InN than that between GaN and InN. This observation is in a good agreement with the report investigating on the effects of different templates on crystalline quality of InN layer grown by MOCVD[167]. In Figure 3.17, it is observed that inclusion of the second InN phase (0101) increases the surface roughness of InN layers grown on GaN/Sapphire (0001) templates. However, there is no such relation observed in the layers grown on Sapphire (0001) templates. The single phase InN layers grown on Sapphire (0001) templates have large surface roughness and FWHM of E_2(high) Raman line. The same samples exhibit large grain areas as presented in Figure 3.18. Therefore, these results suggest that it would be possible to grow strained single phase InN layers on Sapphire (0001) templates. Utilization of this type strained III-V layers in semiconductor technology is mature and the details are described elsewhere[168]. This strain in group-III nitride structures can also be manipulated to engineer advanced optoelectronic applications[169]. From Figure 3.18, the average grain areas of InN layers grown on GaN/Sapphire (0001) templates were reduced by material decomposition at surface. The behavior of surface decomposition is different from the layers grown on templates of different lattice mismatch to InN. In the next section, the results of the studies on surface material decomposition are presented.

3.4.1.3 The effects of in-situ material decomposition

In order to study the influence of lattice mismatch in in-situ material decomposition, InN layers have been grown on GaN/Sapphire (0001) and Sapphire (0001) templates. The results of ex-situ surface morphological analysis have been compared to the results of real-time optical characterization experiments performed on these InN layers.

In Figure 3.19.a, the real-time PARS and LLS traces are shown. In both traces, interference oscillations are present. The intensity of LLS signals starts to increase after the growth time about 5500 seconds marked by the arrow. This increase in the LLS signal is due to the increased off-axis scattering from the surface due to material decomposition at surface increasing the surface roughness. In Figure 3.19.b, AFM image of the same surface is depicted. At the surface, there are surface pits as a result of material decomposition.

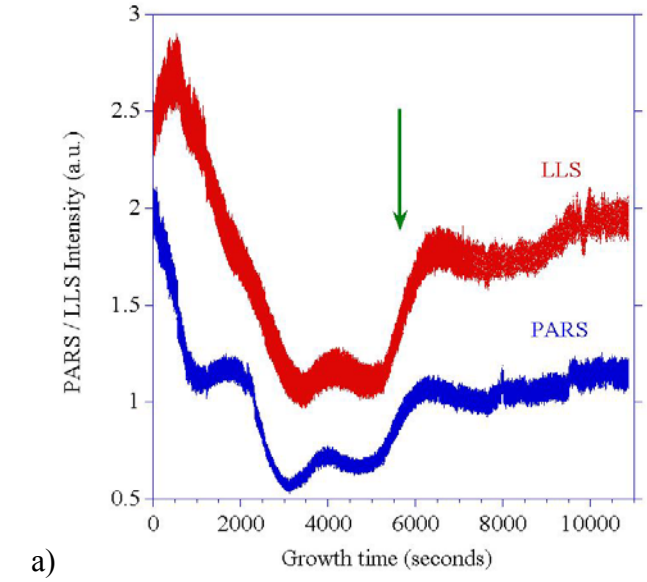

a)

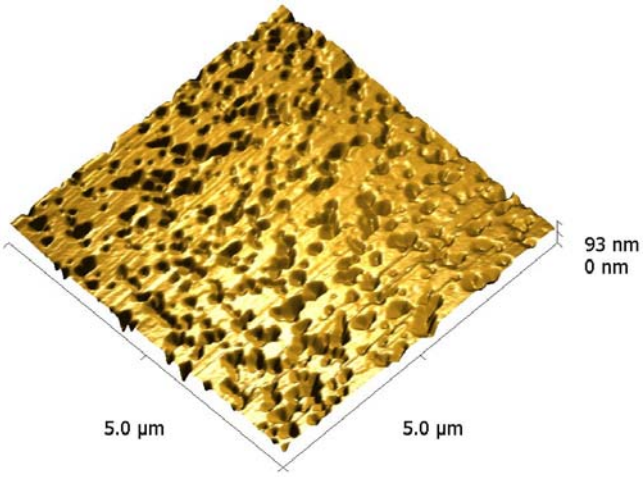

b)

Figure 3.19 a) Real-time LLS and PARS traces and b) 5.0µm x 5.0µm AFM image of decomposed InN layer

In Figure 3.20.a, the decomposition time as a function of surface pit depth is shown. In this analysis, the decomposition time refers to the total time from the green arrow position (see Figure 3.19.a) to the end of the growth run. The InN layers grown on Sapphire (0001) templates exhibit surface pits at lower decomposition time than the layers grown on GaN/Sapphire templates. In Figure 3.20.b, the correlation between FWHM of InN (0002) Bragg reflection peak and surface pit depth is shown. In both panels of the Figure 3.20, the layers

exhibiting single phase are marked by arrow. The InN layers grown on GaN/Sapphire (0001) templates exhibit sharper (0002) Bragg reflection peak than the layers grown on Sapphire (0001) templates. Increased surface pit depth results in broadening in the spectral line-shape of (0002) Bragg reflection peak.

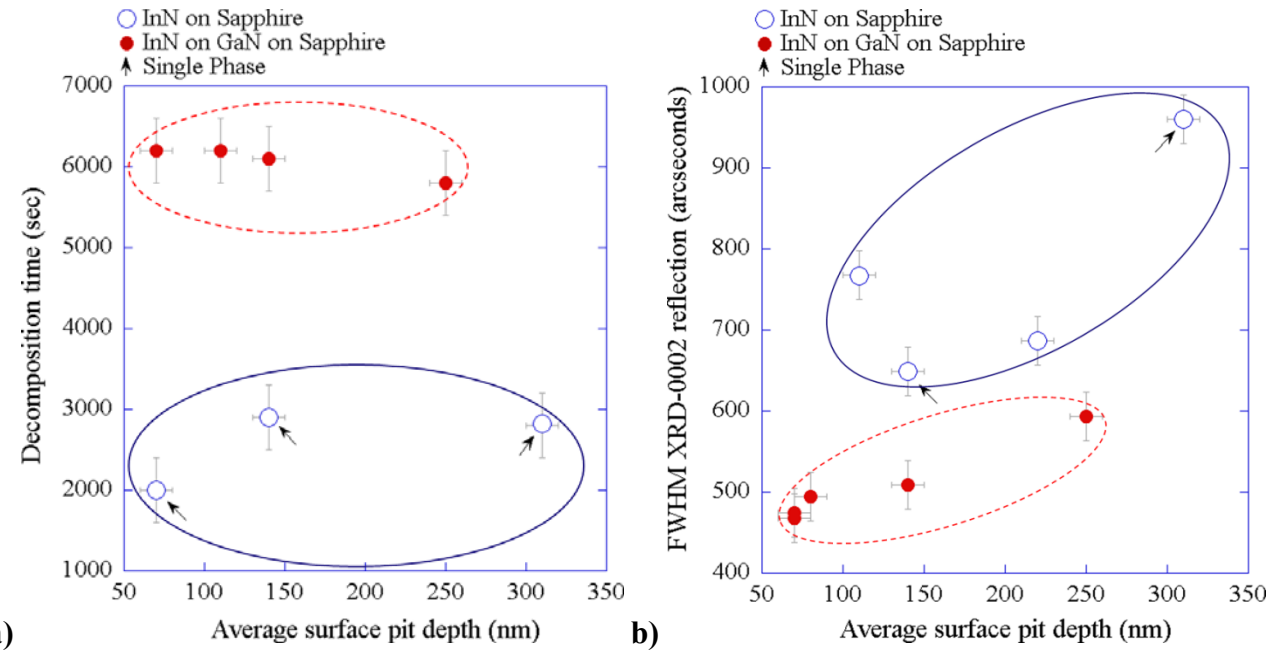

Figure 3.20 a) Decomposition time and b) FWHM of (0002) Bragg reflection peak versus average surface pit depth.

The results of material decomposition time versus average surface pit depth correlation suggested that InN samples grown on GaN/Sapphire (0001) templates had surfaces of higher stability than the samples grown on Sapphire (0001) templates; therefore, it took longer to remove the material on their surfaces. The layers grown on Sapphire (0001) templates tend to have single phase although the material decomposition is easier at their surface. Since XRD probes long range ordering, the observations made on XRD are affected by decomposition on both types of InN layers grown at different templates. InN layers grown on GaN/Sapphire (0001) templates exhibited better

(0002) lattice plane arrangement than the samples grown on Sapphire (0001) templates. However, the effects of decomposition were similar so that the increased average surface pit depth disturbed the (0002) lattice plane arrangement resulting in broadening in the corresponding XRD (0002) Bragg reflection.

3.4.1.4 Growth modes: Surface topography versus growth history

In order to investigate the influence of the growth temperature in growth modes, InN layers have been grown at different growth temperatures. The surface morphological and crystallographic properties of the layers have been analyzed and linked to the growth temperature.

The kinetic processes at the growth surface are affected by the surface characteristics such as, adsorption sites and potential barriers which are defined by the distribution of the surface energy. The growth driven by the arrival, the motion of the surfactants under the presence of adsorption sites, and the path that the advancing growth follows define the growth mode. In epitaxial growth, layer by layer growth of monocrystalline layers is the essence while three dimensional growth is utilized for development of unstrained nanostructures. In either case, a complete understanding of the growth conditions is essential to improve the understanding about InN layers to take further steps into the development of advanced optoelectronics structures. In order to understand the growth conditions defining the growth mode of InN layers, in-situ and ex-situ observations were compared and the findings from this analysis were correlated to surface morphology.

The growth modes of InN have been studied by OMVPE[170-172] and MBE[173] growth techniques. The effects of different buffer interlayer, HT-GaN and LT-InN, were studied and their effects on the crystalline properties and the growth modes were demonstrated[170]. Another

study reported the growth InN nanostructures by utilizing Volmer-Weber model for growth[171] and demonstrated the growth of InN nanostructures. A pulsed-MOVPE technique was demonstrated to provide high quality InN layers and the effects of the substrate in the growth mode was demonstrated[172]. The effect of high-speed reactant gas on MOVPE technique was investigated and the concentration was shown to enhance the 2D growth mode[172]. By the MBE technique, 2D and 3D growth modes of InN were investigated[173]. This study demonstrated that lowering the growth temperature from 450 C^o to 370 C^o shifts the growth modes of InN toward 3D from 2D growth. However, the information about the quality of the InN layers was not provided. In this research, the growth modes of InN at temperatures above 800 C were investigated and the findings were correlated to XRD characterization results.

The morphology of a surface is defined by the variation of surface energy[174]; thus, the final surface topography is constructed by the surface energy minimization real-time depending on the related growth path. The real-time evolution of the surface topography was investigated by LLS traces from different samples having different types of growth modes: 2D-like growth (i.e epitaxial growth), Columnar, and 3D growth.

2D-like growth

In Figure 3.21, InN layer grown on GaN/Sapphire (0001) template is presented. This surface is intentionally called 2D-like since it is not pure epitaxial although it has a relatively smooth surface of surface roughness ~17nm. In Figure 3.21.a, the AFM image of the sample is shown. It is a relatively smooth surface and large grain areas.

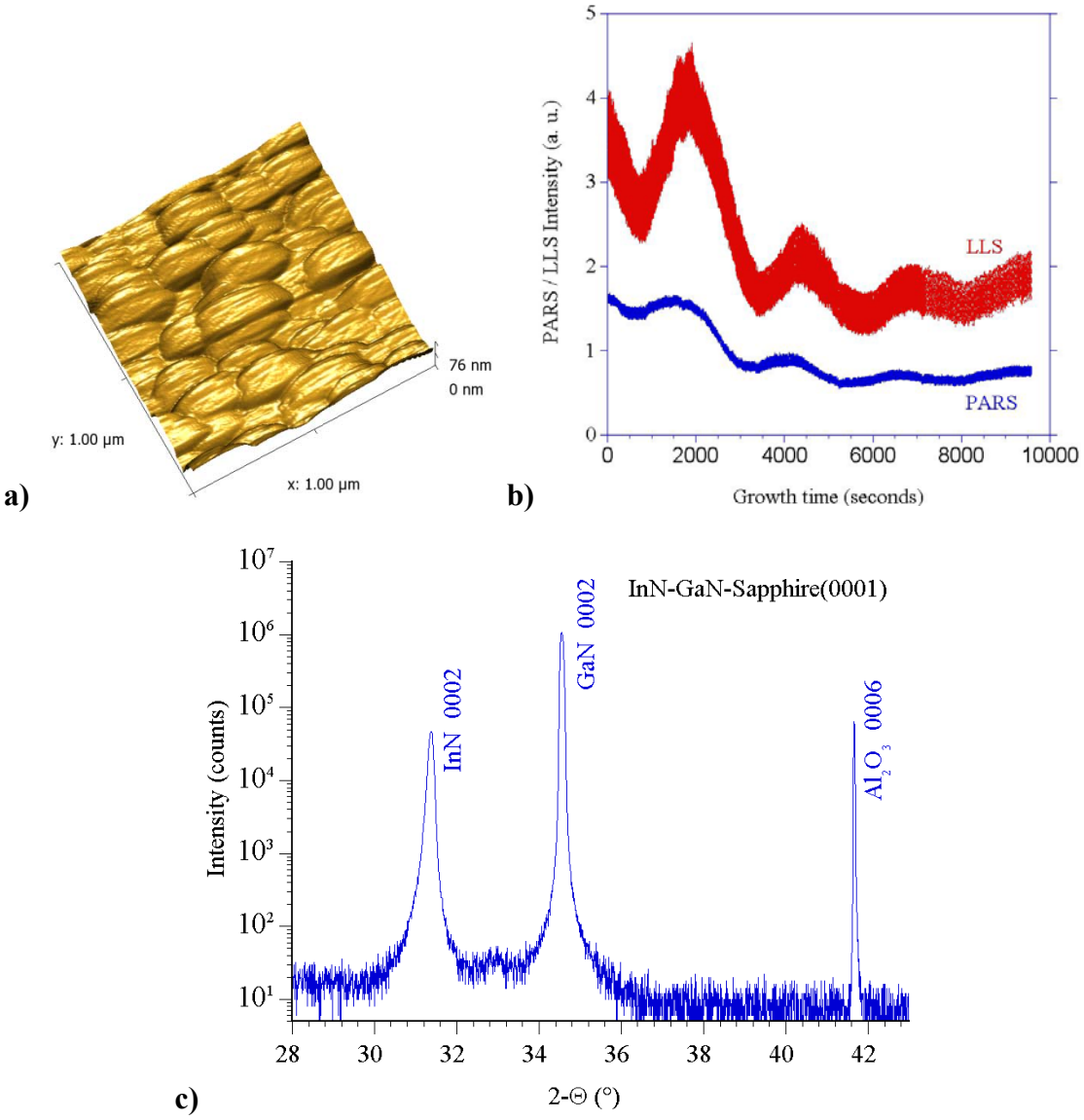

Figure 3. 21 a) PARS and LLS signals, b)AFM image, c) XRD pattern for 2D-like InN growth.

In Figure 3.21.b, the real-time evolution of LLS and PARS signal is demonstrated. LLS signal has a decrease in the first ~5000 seconds indicating the transition of the surface from nucleation to layer and latter progression of the signal tends to decrease while maintaining the interference oscillations due to changing thickness of the growing film. The overall down-slope tendency of LLS signal is the indication of 2D growth while the interference oscillations confirm

the growth of a single layer. In Figure 3.21.c, the XRD pattern of the sample is shown. A sharp InN (0002) Bragg reflection peak is an indication of high quality single phase InN crystal. This peak has a FWHM of about 458 arcseconds.

Columnar growth

The columnar growth has been observed on InN layer grown on Sapphire (0001) template. The AFM image of this surface is shown in Figure 3.22.a. This growth is not perfectly columnar since the hexagonal columns are located on the top of non-geometric large grains. This observation indicates that the growth was redirected from 2D to columnar growth during the growth progression. In Figure 3.22.b, corresponding to the real-time LLS trace is shown. In LLS signal, the decrease observed in first ~8000 seconds along with interference oscillations is because of the layer formation. However, further progression of the growth is toward the columnar growth since the interference oscillations are not present anymore although LLS signal continues to decrease.

In Figure 3.22.c, XRD pattern of the layer is shown where single phase InN (0002) Bragg reflection is present. The FWHM of the peak is about 962 arcseconds indicating a reduction in crystalline quality. The broadening of an XRD feature could be influenced by mainly crystalline quality, tilting of the crystallites from preferred c-axes orientation, and thermal expansion difference between the film and the template.

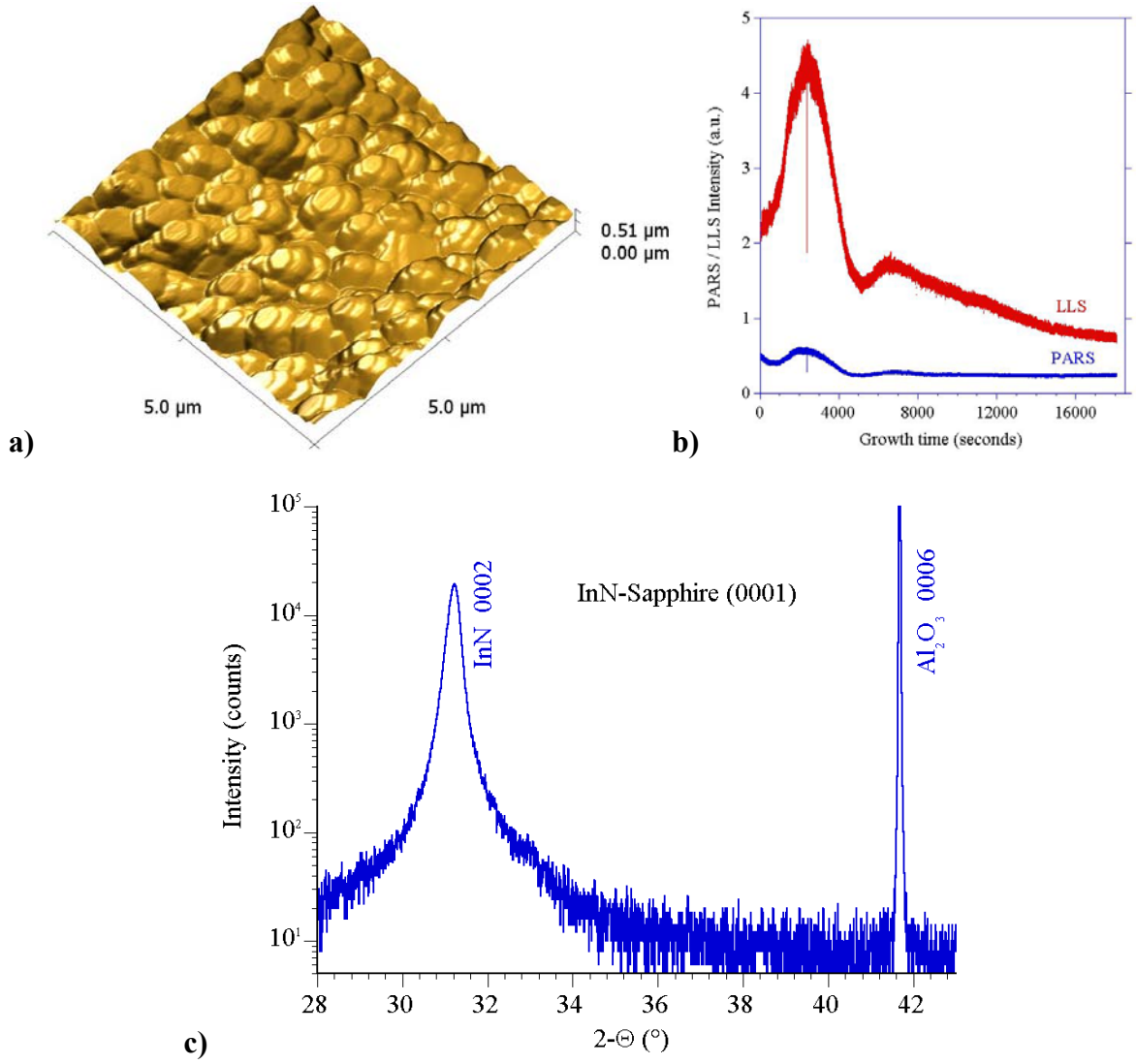

Figure 3. 22 a) PARS and LLS signals, b)AFM image, c) XRD pattern for columnar InN growth.

In Figure 3.23, the deviations of the InN crystallites from c-axes are presented in oblique view of the AFM image. The tilt angles vary from 15-35 degrees to surface normal. The tilts and the variations are owing to the common contributions of the lattice mismatch and thermal expansion difference between InN and Sapphire. In InN samples grown on GaN/Sapphire templates, both effects are suppressed by the GaN buffer layer. In the AFM image, the hexagonal symmetry is observed from clear hexagonal shapes of the InN crystallites. Therefore, the

broadening in the (0002) reflection is the result of lattice mismatch and thermal expansion difference.

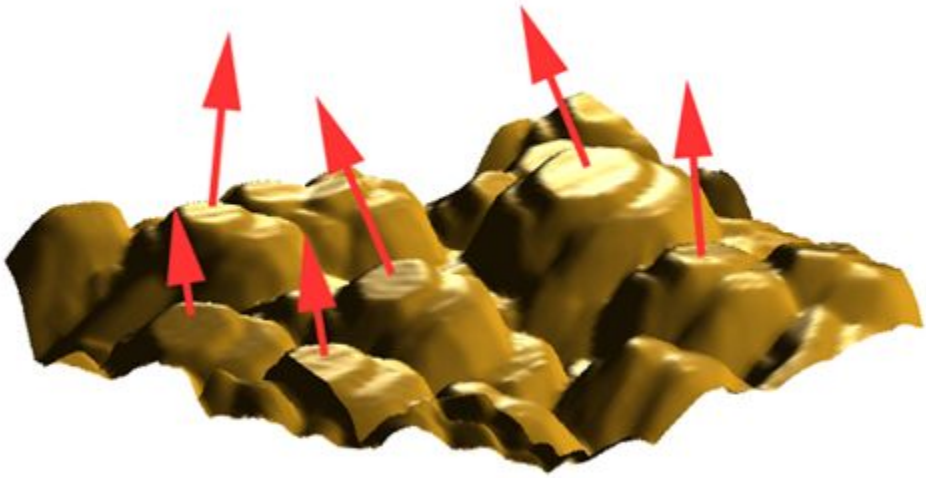

Figure 3.23 AFM image of InN columnar growth showing tilt axis of the columns due to lattice strain and thermal expansion difference between InN and Sapphire.

3D growth

Three-dimensional growth has been observed in InN sample grown on GaN/Sapphire templates. The AFM image of the surface is shown in Figure 3.24.a in which a representative hexagonal pyramid is observed. Another region on the surface is shown in the next panel, b, of the same image where there is a 2D layer and hexagonal plate underlying large pyramid. The plate is shown by continuous arrow while the pyramid is shown by dashed arrow. The optical image of the surface is shown in Figure 3.25, where the hexagonal pyramids and plates are observed.

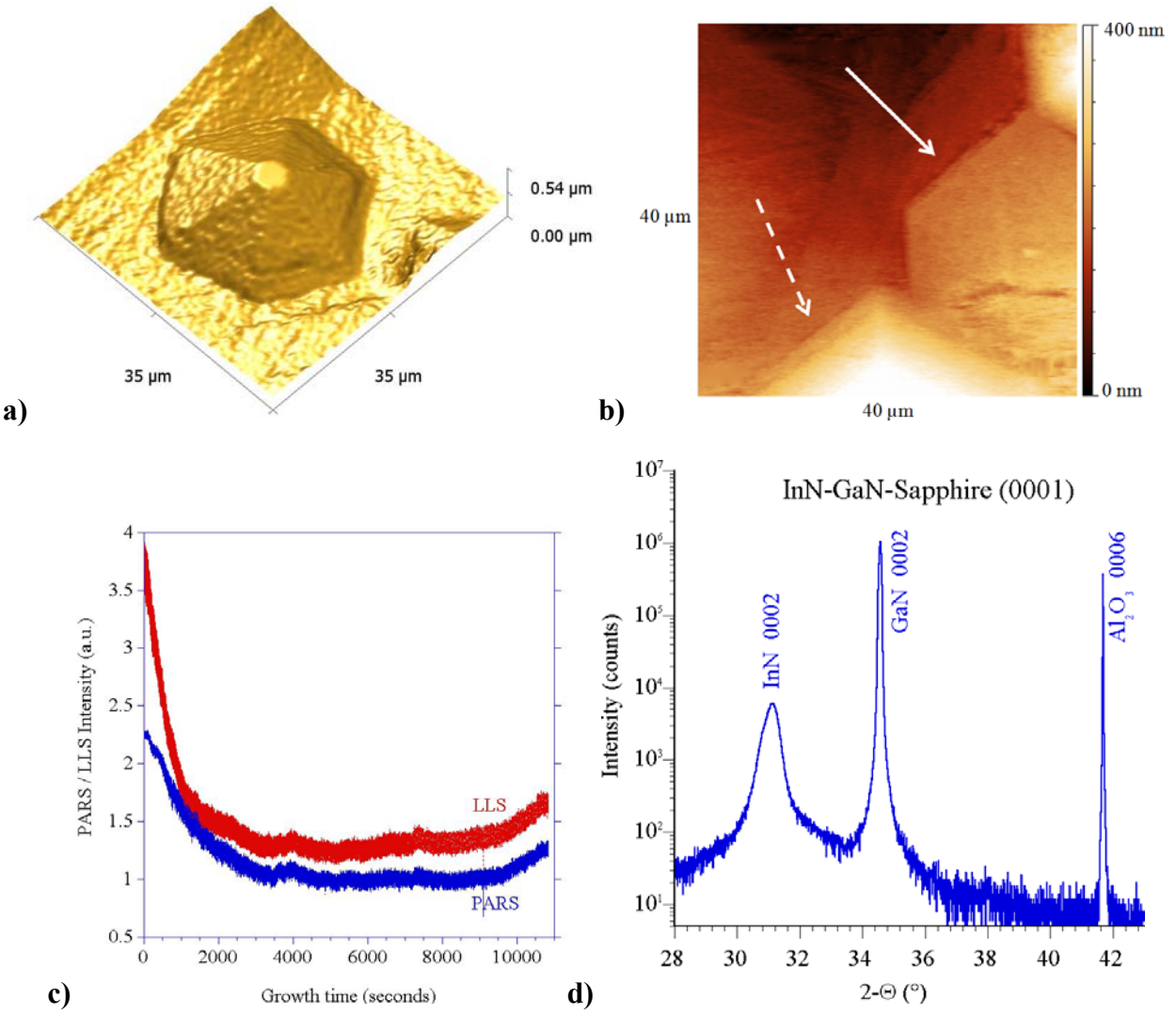

Figure 3. 24 a) AFM image of 3D InN growth, b) AFM image of the same sample at a different region showing plates and 2D layer under 3D structures, c) PARS and LLS traces and d)XRD pattern of 3D InN growth.

The real-time PARS and LLS traces are shown in Figure 3.24.c. The LLS signal decreased in first ~3000 seconds of the growth indicating formation of a thin layer at surface. However, the progression of the signal shows a tendency of a slight increase. In no stage of the LLS trace, are interference oscillations present. The XRD pattern of the sample is depicted in the panel d of the same figure. The XRD pattern presents that the layer is a single phase InN with a broad (0002) Bragg reflection peak. The FWHM of this peak is about 1659 arcseconds. The tilt

angles of the pyramids vary between 3-7 degrees from AFM results since the GaN buffer layer suppresses the effects due to the lattice mismatch and the thermal expansion difference. Hence, the broadening observed in the XRD (0002) reflection is due to the large 3D structures rather than lattice mismatch.

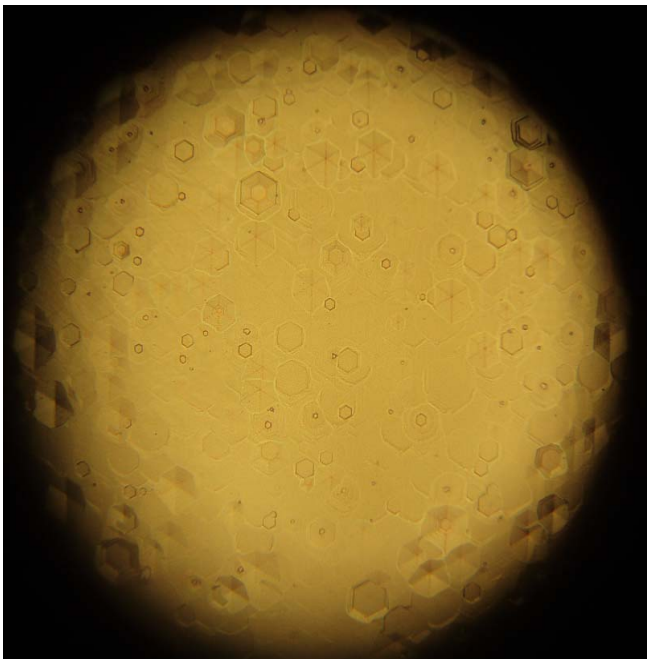

Figure 3. 25 Optical image (1mm x 1mm) of InN surface of 3D structures.

Discussion: InN growth mode investigation

In HPCVD growth, the efficiency in source material use and the optimization of diffusion length is provided by small channel height around ~1mm (see section 3.1.1). The consequence of the small height of the flow channel is that the film growth on both substrates is affected by the both heaters loaded symmetrically. So, the growth temperatures on both heaters have to be considered in the evaluation of the AFM results. In Table 3.7, all the findings on growth modes are summarized. All templates utilized in this analysis were loaded into lower substrate holder.

Table 3. 7 Summary of the results of the growth modes analysis of InN layers grown on different templates.

Growth Mode	Template	Growth Temperature (C^o)		FWHM of XRD (0002) Reflection (arcsec)	Tilt angle of crystallites (deg)
		Lower Heater	Upper Heater		
2D	GaN/Sapphire	800	Constant 820	457	-
Columnar	Sapphire	800	Graded 820-800	962	15-35
3D	GaN/Sapphire	800	Constant 820	1659	3-7

One of the factors to determine the growth mode in epitaxial film growth is the surface mobility of the adatoms due to their kinetic energy at surface. This energy is provided by the temperature introduced by the heaters to the growth surface and the growth temperature influences the growth mode directly. The InN sample grown on GaN/Sapphire (0001) template at temperatures of the lower heater at 800 C^o and the upper heater at constant 820 C^o reveals 2D-like growth mode. This growth was dominated by Frank-van der Merve model in which layer by layer growth was proposed[174]. However, as the lower heater decreased to 800 C^o and the upper heater is graded (linearly) from 820 C^o to 800 C^o, the growth mode shifts to Stranski- Krastanov mode[174] in which the growth starts 2D; however, it advances towards 3D in terms of hexagonal columns. The mobility of the adatoms in the early stages of the sample showing columnar growth was enough to be adsorbed at appropriate growth sites evoking the 2D growth. However, at the later stages of the growth, by gradual decrease of the upper heater temperature, their mobility was decreased resulting in adatom adsorption at the closest sites instead of preferential sites. Because of this reason, the growth initializing in 2D progressed and resulted in 3D growth.

The same behavior observed in the LLS trace of this sample where the interference oscillations were not continuously observed as the sample showing 2D growth but disappeared after sometime by the change of the growth mode to 3D. These temperature settings where the columnar InN growth was observed are the transition regions for InN growth modes. The observation made on the InN sample showing a strong 3D mode is supportive of this idea. As the lower and the upper heater temperatures are kept constant at 800 C^o and 820 C^o, respectively, the growth processes promoted 3D growth resulting in large hexagonal pyramids. The upper heater temperature is the highest that the sample showing columnar growth was decreased from. Because of this reason, in the sample exhibiting large pyramids, the adatom motility was higher which promoted their lateral motion. This growth was dominated by Volmer-Weber model in which 3D growth was proposed[174]. Shifting the growth from 2D to 3D broadens the XRD (0002) Bragg reflection peak since it modulates the long range ordering of the lattice planes. The tilting of the crystallites due to this shift into 3D growth differs depending on the template type. The template with higher lattice mismatch to InN, Sapphire (0001), exhibits InN layer with crystallites of larger tilt angles than GaN/Sapphire (0001) template.

The results of this section suggest that single phase high quality InN layers can be grown at different temperatures yielding a variance in crystalline quality and the growth modes. Temperature gradient approach can be used to play with the geometry of InN such as, transition from hexagonal columns to hexagonal pyramids. Depending on the direction and the range of the temperature gradients, embedded or free-standing strain-free nanostructures can be engineered. The results obtained from this analysis demonstrated similar behavior to the report[149] investigating the tendency of the growth to advance 3D by decreased growth temperature although there is a large difference between the growth temperatures investigated.

3.4.1.5 Surface morphology during coalescence

In order to study the coalescence behavior of InN layer grown on GaN/Sapphire (0001) template, a transition region from substrate to film has been investigated by AFM. The transition is due to the temperature gradient at a close area of the template edge. At this transition region, it is possible to investigate how the film forms from the individual islands.

The coalescence of InN islands in the initial stages of growth has been studied by OMVPE[175-157] and MBE[178] growth techniques. By MOCVD growth technique, the temperature dependence of the coalescence behavior was demonstrated[175]. The effects of indium pre-deposition were demonstrated to enhance the coalescence behavior[176]. Another report demonstrated the introduction of CCl_4 to suppress indium droplet formation[177]. The results of this analysis demonstrated that the increasing CCl_4 incorporation enhanced the InN coalescence. On the other hand, in MBE grown InN films, the growth temperature was demonstrated to play the major role in determining the coalescence behavior[178].

The optical image in Figure 3.26.a shows the direction of flow by the arrows and the transition region within the red square. The line in the square was where the AFM investigation was performed. In Figure 3.2.6.b, the square is zoomed and the transition region of length of 2.5 mm is demonstrated. High resolution AFM image was taken at every 0.1mm step and surface roughness of 200nm x 200nm area at each step was determined. The c panel of the same figure shows the 4μm x 4μm AFM image of the transition region. The surface roughness as a function of distance is depicted in the panel d. The roughness at point 0 nm is about 15 nm which is the roughness of the grown layer. Moving to the coalescence region, there is a gradual increase observed in the surface roughness from 15 nm to 20 nm within 1 mm of the transition region. In the next 0.5 mm, at 1.5 mm of transition line, the surface roughness increases from 20 nm to 40

nm rapidly where the surface minimization occurs exhibiting a turning point at the curve, and there is a rapid decrease in the surface roughness to 12 nm. This is the region where there are infrequent nucleated islands on smooth template surface.

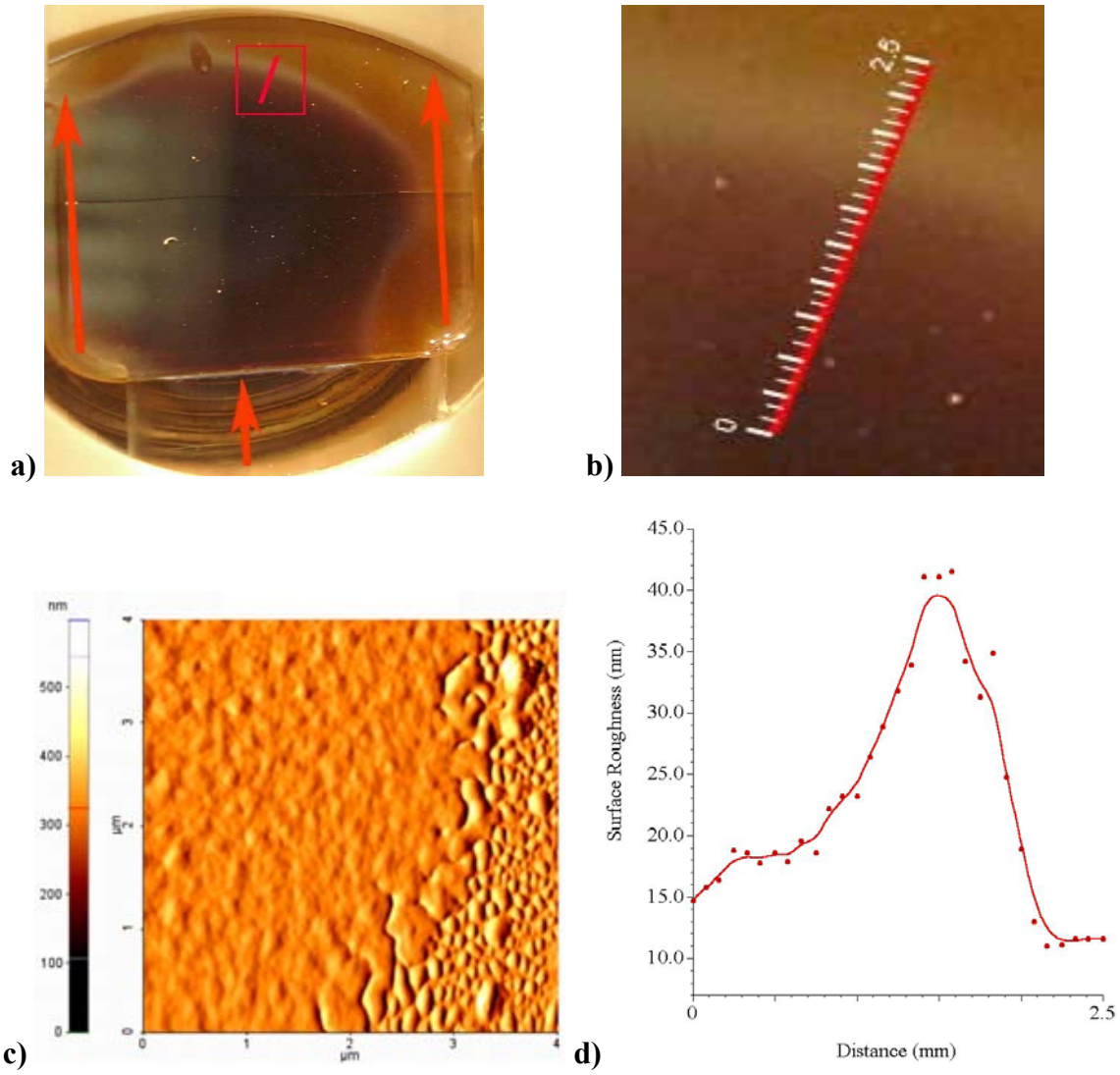

Figure 3. 26 a)AFM image of the InN grown on GaN/Sapphire template for coalescence study in which the region studied is shown by a red line, b) the zoomed optical image of the region within red box in a, c) AFM image of the same region, d) changes in the surface roughness as a function of distance along the transition region.

In the initial stages of the thin film growth, the adsorption sites capture the mobile adatoms to form islands. As the growth continues, these islands become large enough to coalesce with each other to form larger grains of the deposited material and the growth advances until a uniform layer of film is obtained[179]. The coalescence is the first step in which the layer is formed; therefore, it is important to understand the coalescence behavior to improve the knowledge about InN thin film growth. The surface tension of InN islands during nucleation governs the coalescence behavior during transition from nucleation to layer stage exhibiting changes in the surface roughness. The results of this analysis reveal that the turning point of the surface roughness is about 40 nm during coalescence of InN layers grown by HPCVD on GaN/Sapphire (0001) templates. The maximum height of the nucleated islands during the coalescence could be an important limiting factor for heterostructures of thin epitaxial InN layers by determining the critical thickness of the nucleation.

3.4.1.6 Optimization of InN nucleation

In order to investigate the nucleation behavior, InN layers have been nucleated using different deposition mechanisms with changing precursor injection steps. The same procedure has been applied for the nucleation on GaN/Sapphire (0001) and Sapphire (0001) templates to investigate the influence of the templates of different lattice mismatch to InN.

The GaN/Sapphire (0001) and Sapphire (0001) templates were loaded into the HPCVD reactor in a symmetrical configuration. The growth pressure and the main flow were set to 15 bar and 12 slm which were kept constant along with the growth temperatures during the nucleation studies. The separation between TMI/TMG and ammonia pulses was 1.2 sec. A special

nucleation procedure was applied on samples grown on GaN/Sapphire (0001) and Sapphire (0001) templates.

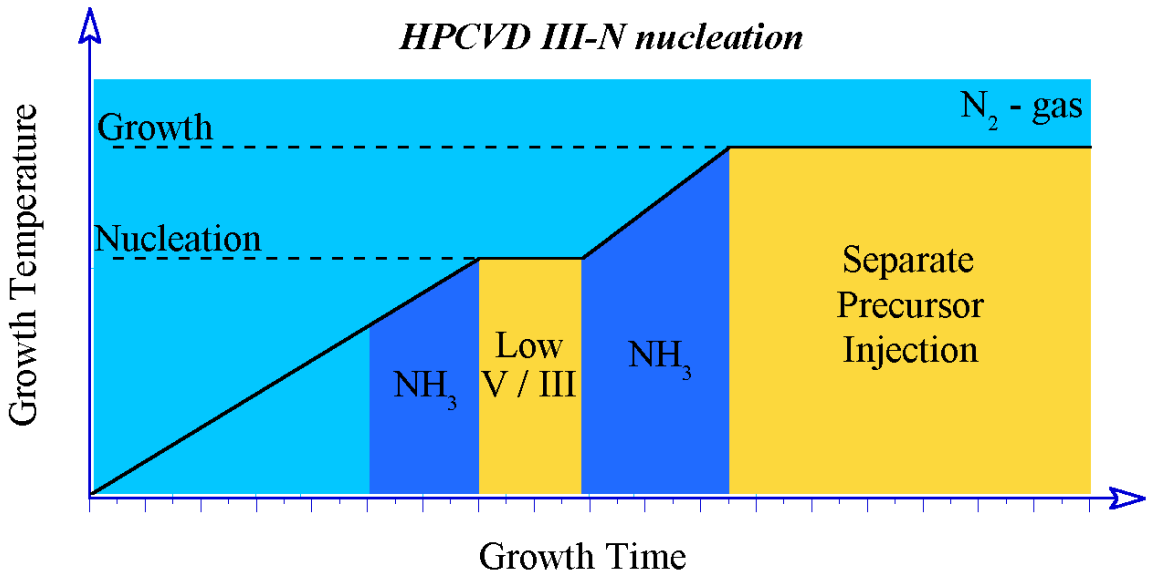

Figure 3. 27 Schematic view of growth pattern to optimize nucleation.

The schematic view of the nucleation procedure is shown in Figure 3.27. The nucleation procedure consisted of 4 sequences before the steady state growth sequence. The first was the heat-up sequence in which the heater temperature was increased gradually under high-pressure N_2 flow. At the end of the first sequence, the second sequence was nitridization of the template while temperature was still being ramped up. The nitridization time was kept constant for all samples investigated in this section. The third sequence was indium-rich (low V-III ratio ~500) InN growth at nucleation temperature which was kept lower than the growth temperature to decrease the mobility of indium atoms at surface. The fourth sequence was employed to consume the excess indium left from the previous sequence while the temperature was being ramped up to the growth temperature. The last sequence is the steady-state growth which was applied for 5

minutes for all samples investigated. In this study, only the number of the steps in the third and the fourth sequences was changed. The details of the patterns investigated are summarized in Table 3.8. Each step corresponds to one precursor injection cycle.

Table 3. 8 Different patterns for nucleation studies

Sequence	Pattern 1	Pattern 2	Pattern 3
Low V/III steps	5	10	15
Heat-up NH_3 steps	30	60	90
Growth steps	50	50	50

AFM images of nucleation surfaces on GaN/Sapphire (0001) templates using different nucleation patterns are demonstrated in Figure 3.28. All AFM images were acquired for an area of 30μm x 30μm. The color bar scales for z-axis are located to the right of each image. The nucleation by applying 5 steps of low V-III ratio and 30 steps of NH_3 heat-up sequences is shown in Figure 3.28.a. The nucleated clusters had large dimensional variations and their distribution was not homogeneous. By the increase of low V-III ratio sequence steps from 5 to 10 and NH_3 heat-up sequence steps from 10 to 60 in the pattern 2, the dimensional variation of the clusters decreased as the homogeneity increased. The AFM image of the surface nucleated by the pattern 2 is shown in the panel b. The pattern 3 consisted of 15 steps of low V-III sequence and 90 steps of NH_3 heat-up sequence. The AFM image of the surface nucleated by the pattern 3 is shown in the panel c. Application of the pattern 3 took the dimensional variation further down by increasing the homogeneity.

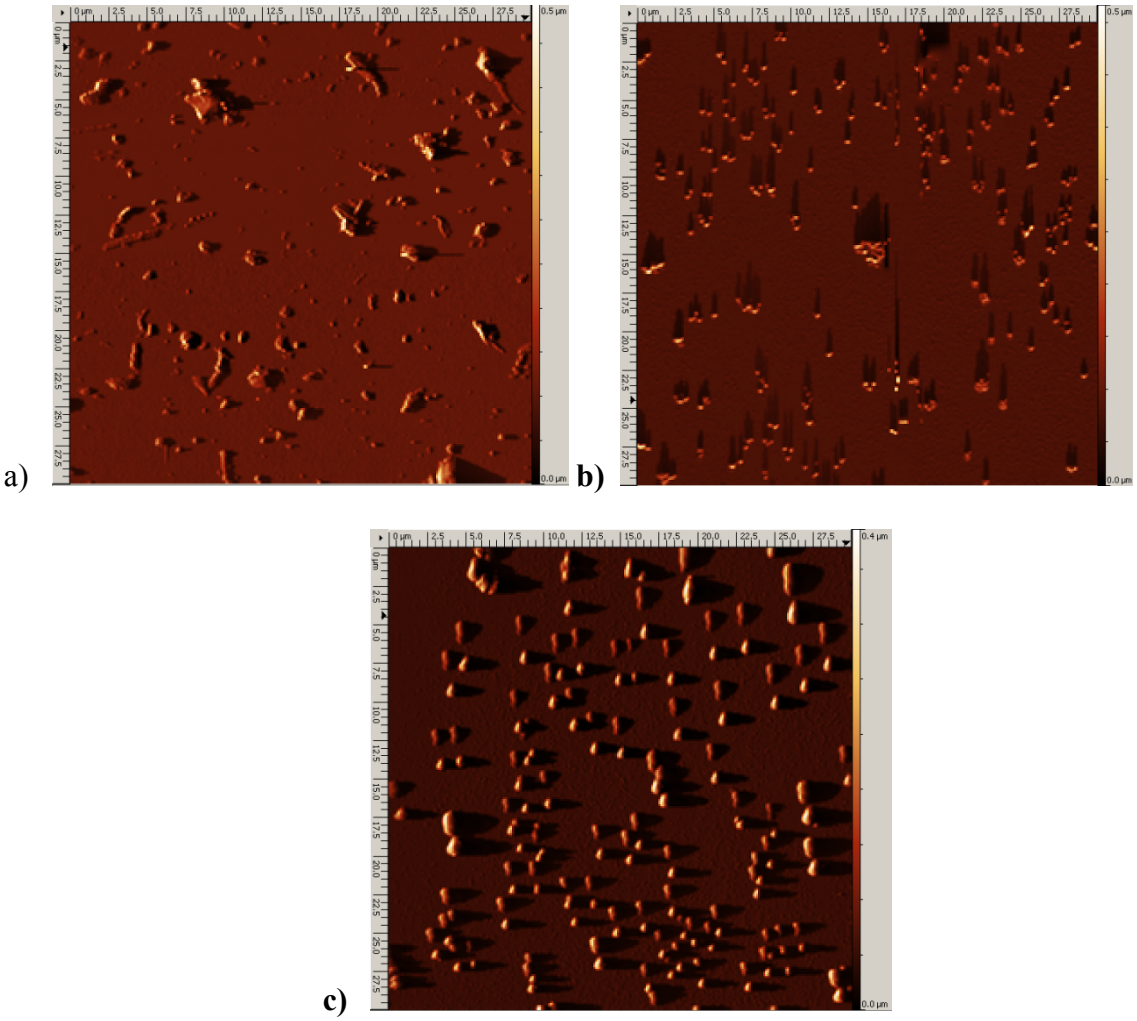

Figure 3.28 AFM images of the nucleation surfaces on GaN/Sapphire (0001) templates deposited with a) Pattern 1, b) Pattern 2, c) Pattern 3.

In Table 3.9, the results of the AFM analysis of GaN/Sapphire (0001) nucleation surface are shown for different patterns employed. The 3D surface coverage provides the ratio of the total cluster area to the total surface area in percentages. The average surface grain area is the arithmetic average of the projection area of the clusters at surface. The total 3D volume is the total volume of the clusters at surface. The standard deviation of cluster is the standard deviation of the projection area curve of the surface clusters. In a better nucleation, 3D surface coverage and average surface grain area should converge to a maximum while total 3D surface volume

and standard deviation of cluster area should converge to a minimum. According to the behavior of the parameters, a better nucleation is obtained by increasing the number of the steps in the heat-up sequence from 30 to 90 resulting in an increase in 3D surface coverage and average surface grain area and a decrease in total 3D surface volume and standard deviation of cluster area.

Table 3. 9 The 3D surface coverage, average surface grain area, total 3D surface volume of nucleated islands on GaN/Sapphire (0001) templates for different InN nucleation patterns.

	Pattern 1	Pattern 2	Pattern 3
Island surface coverage (percentage)	11	13	30
Average island area (μm^2)	0.74	0.86	0.93
Total island volume at surface (μm^3)	39.2	36.4	13.2
Standard deviation of island area distr. (μm^2)	0.97	0.68	0.17

The AFM images of the nucleation surfaces on Sapphire (0001) templates using the same procedure are shown in Figure 3.29. All AFM images were acquired for an area of 30μm x 30μm. The color bar scales for z-axis are located to the right of each image. The nucleation surface nucleated by applying 5 steps of low V-III ratio and 30 steps of NH_3 heat-up sequences is shown in Figure 3.29.a. The nucleated clusters had large dimensional variations and their distribution was not homogeneous similar to what was observed at GaN/Sapphire (0001) surface. By the increase of low V-III ratio sequence steps from 5 to 10 and NH_3 heat-up sequence steps

from 10 to 60 in the pattern 2, the dimensional variation of the clusters decreased as the homogeneity increased as shown in Figure 3.29.b. The AFM image of the surface nucleated by the pattern 3 is shown in Figure 3.29.c.

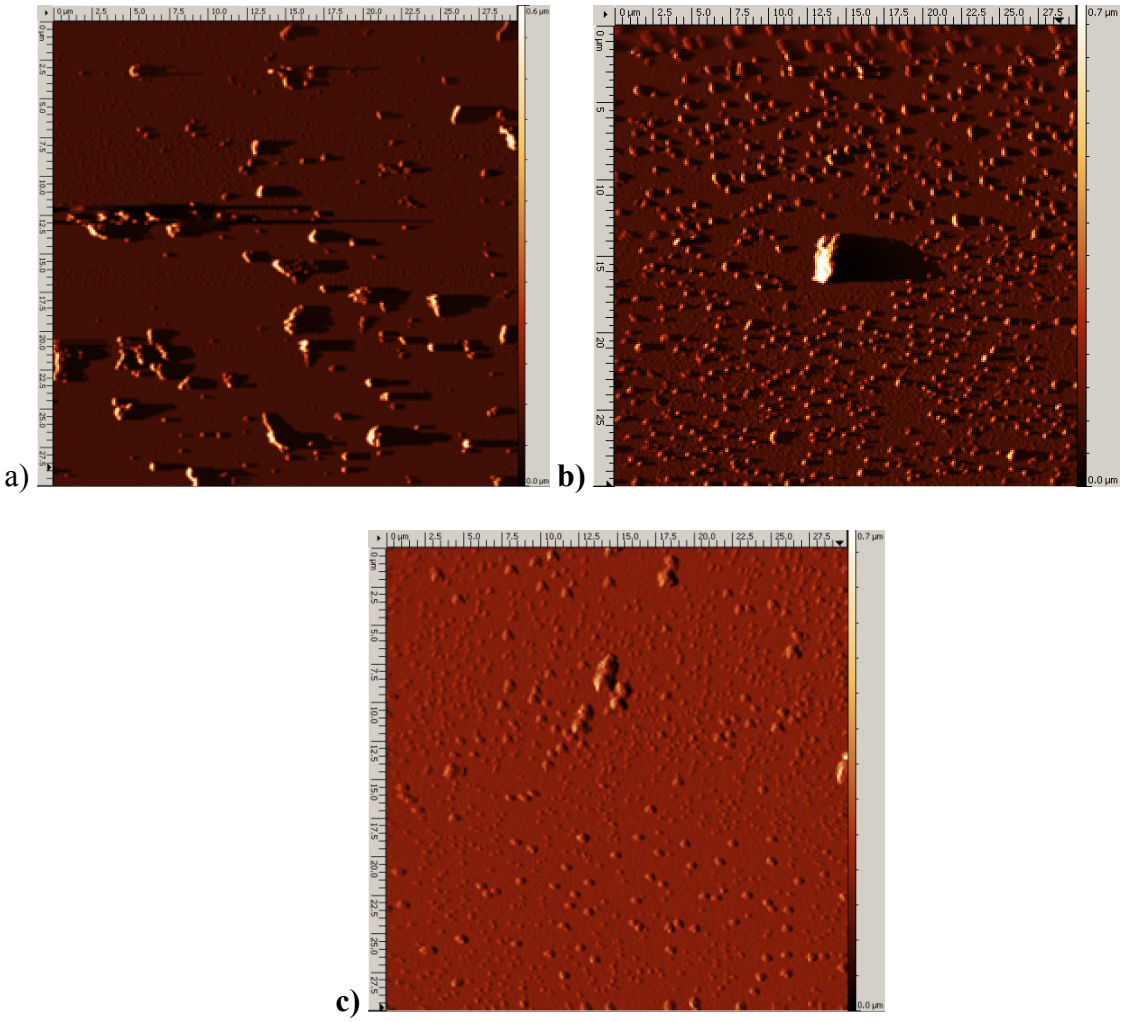

Figure 3.29 AFM image of the nucleation surface on Sapphire (0001) templates deposited with a) Pattern 1, b) Pattern 2, c) Pattern 3.

In Table 3.10, the results of the AFM analysis of Sapphire (0001) nucleation surface are shown for different patterns employed. A better nucleation has been obtained by increasing number steps in the heat-up sequence from 30 to 90 resulting in an increase in 3D surface

coverage and average surface grain area and a decrease in total 3D surface volume and standard deviation of cluster area. The 3D surface coverage of the layers grown on Sapphire (0001) is higher than that of the InN layers grown on GaN/Sapphire (0001) templates.

Table 3.10 The 3D surface coverage, average surface grain area, total 3D surface volume of nucleation on Sapphire (0001) templates for different InN nucleation patterns.

	Pattern 1	Pattern 2	Pattern 3
Island surface coverage (percentage)	12	26	43
Average island area (μm^2)	0.78	0.84	0.95
Total island volume at surface (μm^3)	46.0	40.1	28.2
Standard deviation of island area distr. (μm^2)	1.03	0.72	0.80

As a result of successful nucleation, the nucleated islands should exhibit minimum variation in cluster size and maximum areal coverage of adsorbate clusters. Epitaxy could be achieved by Frank-van der Merwe growth model[174] for which the highest population of surface nucleation sites and layer by layer growth are essential. In Molecular Beam Epitaxy (MBE), the epitaxial growth is achieved by ballistic beam of source atoms while in Chemical Vapor Deposition (CVD), it is achieved by kinetic processes happening at the growth front. These kinetic processes consisting of adsorption, diffusion, and desorption depend on the growth temperature and conditions. Another important parameter is the consumption efficiency of the source atoms at surface. The effects of this parameter are more pronounced in pulsed CVD

approach in which every growth cycle has to be self-complementary (~100% consumption) or special growth sequences have to be employed to consume the excess material left from previous sequence. This was one of the motivations behind application of different numbers of steps at different sequences of the nucleation procedure. The findings from nucleation studies on GaN/Sapphire (0001) and Sapphire (001) templates suggested that the increasing number of NH_3 resulted in surface clusters of larger areas, smaller volumes, and smaller standard deviation in clusters areas. This could be due to the increased number of the indium atoms from low V/III steps creating higher number of nucleation sites at the surface. Larger number of NH_3 steps provides more nitrogen atoms to the growth front by compensating these indium atoms and immobilizing at the nucleation sites. Therefore, higher density of surface cluster distribution is observed in a constant supply of material per injection cycle. The results of this analysis could have important implications in the development of self organized InN and/or group-III nitride nanostructures since they demonstrate that the nucleation can be manipulated for tailoring the nano-scale morphology.

3.4.1.7 Effects of ammonia (NH_3) exposure time

In order to understand the influence of the changing NH_3 pulse injection time on the surface morphological and structural properties, InN layers have been grown by HPCVD using the most successful nucleation pattern described in the previous section (see section 3.4.1.6). The surface morphological properties of the layers have been investigated using AFM. XRD and Raman spectroscopy have been used to investigate the structural properties of these layers.

Figure 3.32 demonstrates the pulse injection scheme employed for steady-state growth. Injection cycle shown by the double-head arrow is 6 seconds and TMI injection time was set to

800ms. S2 is the time separation between the end of the TMI injection and the start of the NH_3 injection. S2 and total growth time were kept constant for all samples investigated in this study while NH_3 injection time was varied from 1000 ms to 2500 ms by 250 ms steps. Corresponding NH_3 injection at each increment is shown by rectangles of fading blue. At each increment, V-III molar ratio was kept constant at 2100 and the precursor flux was adjusted accordingly. The HPCVD reactor was loaded with GaN/Sapphire (0001) and Sapphire (0001) templates in this study in order to investigate the lattice strain effect.

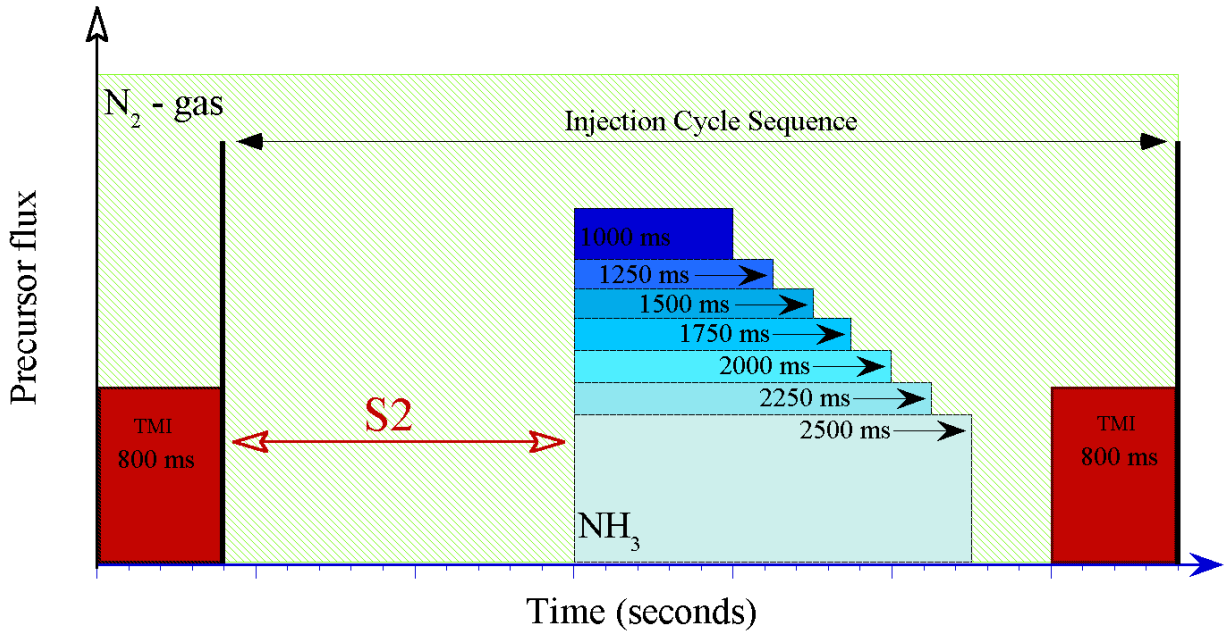

Figure 3.30 Pulsed injection sequence employed for steady-state growth for NH_3 injection time study.

AFM images of InN layers grown on GaN/Sapphire templates are shown in Figure 3.31 a-g for NH_3 pulse injection time of 1000 ms, 1250 ms, 1500 ms, 1750 ms, 2000 ms, 2250 ms, and 2500 ms, respectively. AFM was also used to measure the film thickness using the regions at film surface in which the material decomposition resulted in surface pits reaching to the template surface. These surface pits had relatively small areas (diameter ~ 5-10 μm) distributed randomly

over the surface. The depths of the surface pits were measured at different regions on the film surface and they are averaged to determine the film thickness.

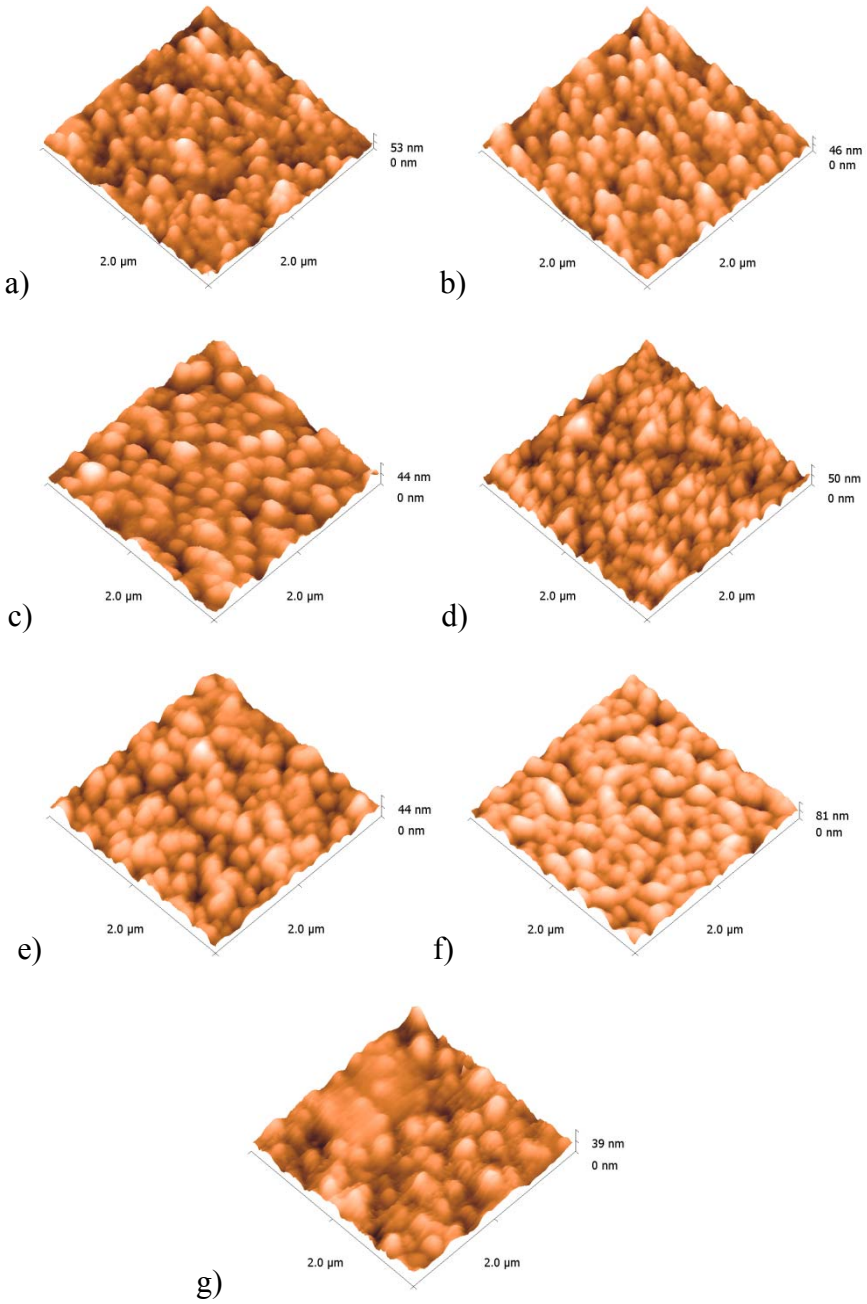

Figure 3.31 AFM images of InN layers grown on GaN/Sapphire (0001) templates with NH_3 pulse injection time of a)1000, b)1250, c)1500, d)1750, e)2000, f)2250, g)2500 ms.

The results of surface morphology analysis of the samples are summarized in Table 3.11. The parameters used for this analysis are film thickness, surface roughness, average grain area, average grain volume, and average growth rate. The average growth rate was calculated by dividing film thickness to the number of steady-state growth cycles. In the table, the average growth rate is given in monolayers/cycle. These InN layers were grown on GaN buffer layers on Sapphire templates. The crystal orientation of the underlying Sapphire was in c-direction (0001); therefore, the preferred crystal orientation for buffer GaN and grown InN layers were in (0001) direction. The lattice parameter of InN along c-axes is 5.7037 [74]. This value was used for the thickness of one monolayer of InN. The increased NH_3 pulse injection time results in an increase in film thickness, average growth rate, average grain area, and average grain volume. The surface roughness decreases with the increasing NH_3 pulse injection time.

Table 3. 11 Summary of the results of the surface morphology analysis of InN layers on GaN/Sapphire grown by changing NH_3 pulse injection time.

NH_3 pulse injection time (ms)	1000	1250	1500	1750	2000	2250	2500
Film thickness (nm)	295	328	376	386	458	468	512
Surface roughness (nm)	8.1	7.7	7.5	7.2	7.3	6.9	6.6
Average grain area (μm^2)	$2.9e^{-2}$	$3.2e^{-2}$	$3.8e^{-2}$	$4.8e^{-2}$	$4.7e^{-2}$	$7.5e^{-2}$	$1.0e^{-1}$
Average grain volume (μm^3)	$8.0e^{-4}$	$8.4e^{-4}$	$1.1e^{-3}$	$1.7e^{-3}$	$1.8e^{-3}$	$2.1e^{-3}$	$2.9e^{-3}$
Average growth rate (monolayers/cycle)	0.28	0.31	0.37	0.39	0.44	0.46	0.49

In Figure 3.32, the dependence of the film thickness and average steady-state growth rate on NH_3 pulse injection time is presented. For NH_3 pulse injection time of 1000 ms, the film thickness is 295 nm. The increase in the NH_3 pulse injection time up to 2500 ms resulted in film thickness of 512 nm. At 2500 NH_3 pulse injection time, the average steady-state growth rate was about half a monolayer per cycle. The dependence on the film thickness and the average steady-state growth rate with respect to NH_3 pulse injection time is almost linear.

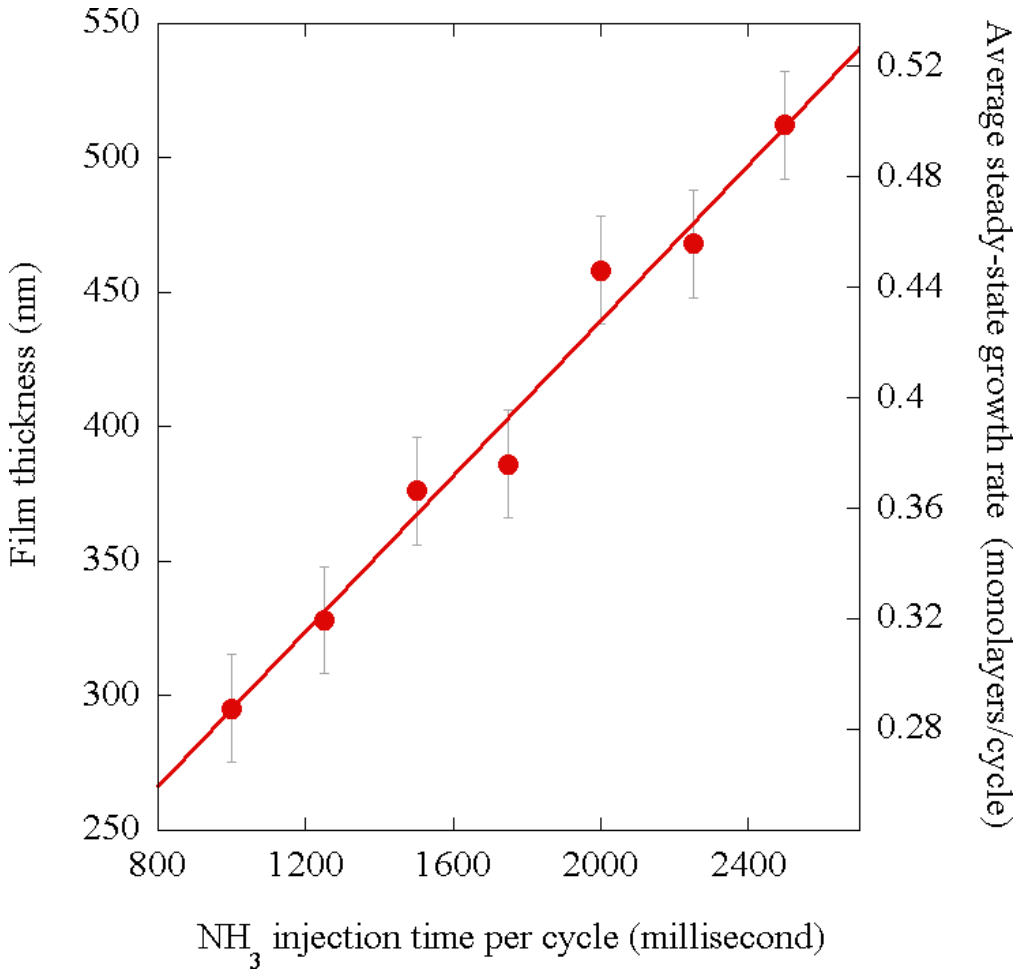

Figure 3.32 Film thickness and average growth rate of InN layers on GaN/Sapphire as a function of NH_3 pulse injection time.

In Figure 3.33, the surface roughness and the average grain volume as a function of changing NH_3 pulse injection time are shown. The increased NH_3 pulse injection time results in the decreased surface roughness while average grain area increased. This observation suggests that the decrease in the surface roughness is due to the increase in the grain areas in the lateral growth direction. This observation could also be supported by the decrease in the average grain volume by increasing NH_3 pulse injection time shown in Table 3.7. Therefore, the findings implied that the growth was pushed towards 2D growth regime by increasing NH_3 pulse injection time.

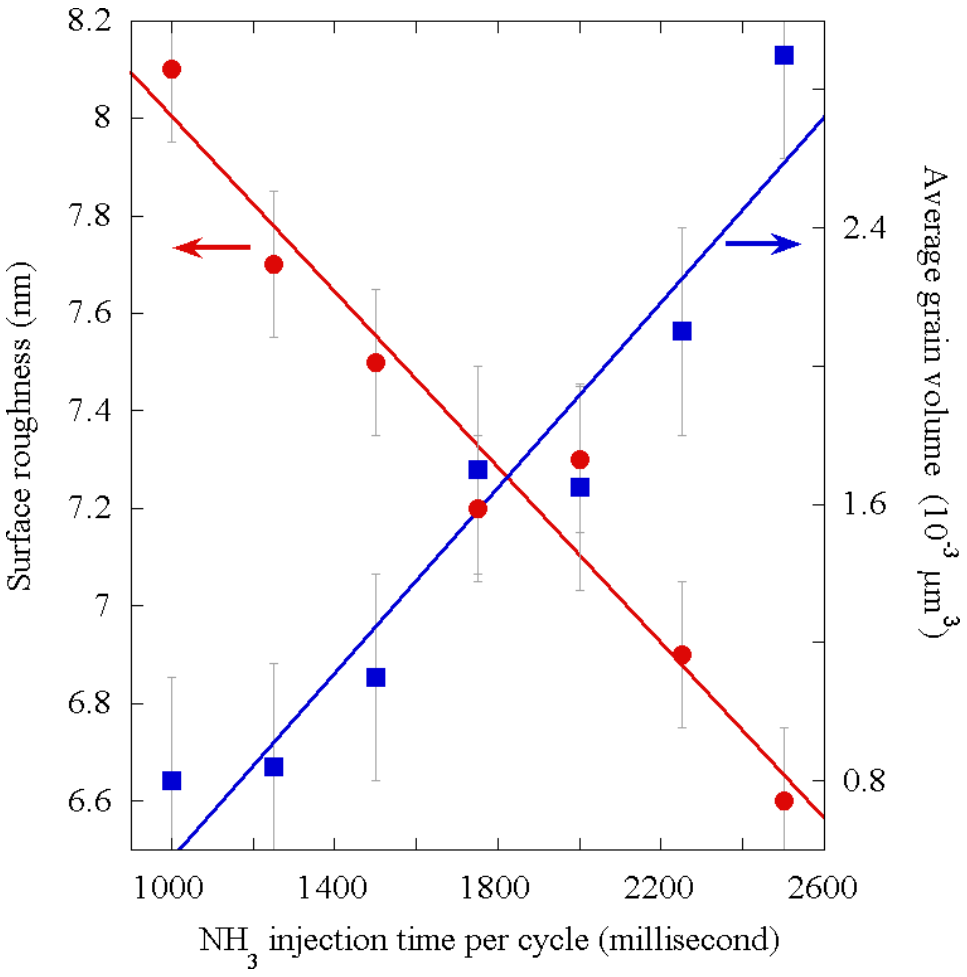

Figure 3.33 Surface roughness and average grain area of InN layers on GaN/Sapphire as a function of NH_3 pulse injection time.

The InN layers have been characterized by XRD to understand the effects of changing NH_3 pulse injection time with respect to crystallographic properties, depicted in Figure 3.34. The panels a and b present positions and FWHM of InN(002) Bragg reflection and the rocking curve analysis of InN (0002) plane with respect to NH_3 injection time, respectively. All InN layers had FWHM of (0002) reflection less than 420 arcseconds which demonstrated the high crystalline quality. The unstrained InN crystal has (0002) Bragg reflection at 31.3°. The deviation of this position is a strain effect. Because of this reason, NH_3 pulse injection time of 1750 ms decreased the crystal strain; however, further increase in the injection time introduced more strain to the lattice by shifting the peak position down and FWHM up. From the rocking curve analysis, shown in 3.34.b, the FWHM of the rocking curve decreased at higher NH_3 pulse injection time.

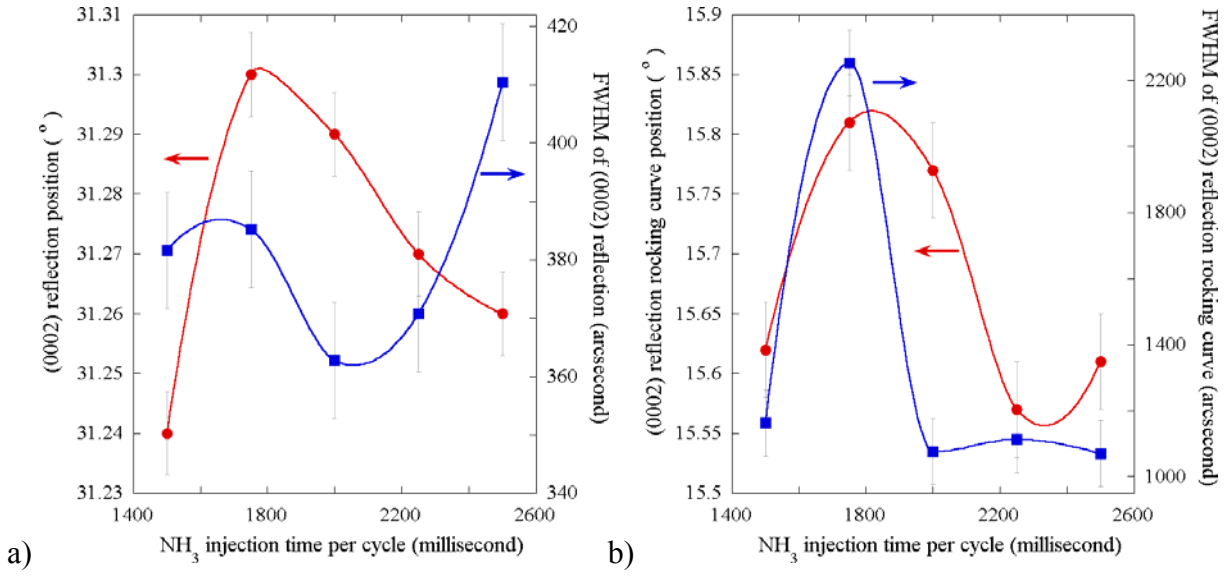

Figure 3.34 XRD analysis of InN layers on GaN/Sapphire (0001) templates with different NH_3 pulse injection time. a) (0002) Bragg reflection position and FWHM b) Rocking curve position and FWHM.

XRD provides information about crystal quality at macro scale (~mm). However, the investigation of local crystalline quality is useful to understand the effects of NH_3 pulse injection

time on structural quality of InN layers. This local information could be acquired from phonon behavior in the InN crystal. Raman spectroscopy experiments were conducted to characterize the phonons. E_2(high) phonon line in Raman spectra of group-III nitrides is informative about the crystalline quality. The spectral position and FWHM of this phonon line can be altered by the crystal strain and the crystalline quality, respectively. The spectral positions and FWHM of E_2(high) vibration modes are shown in Figure 3.35. There is a tendency observed in the position E_2(high) line to higher wavenumbers with line-shape sharpening by the increasing NH_3 pulse injection time. From the modulation of both curves in the figure, there is a clear dependency between spectral position and broadness of the E_2(high) Raman line. As the position of this phonon line shifts to higher energies, the peak is sharpened due to the strain relaxation and it is at the highest energy position in the InN layer grown with NH_3 pulse injection time of 2500 ms.

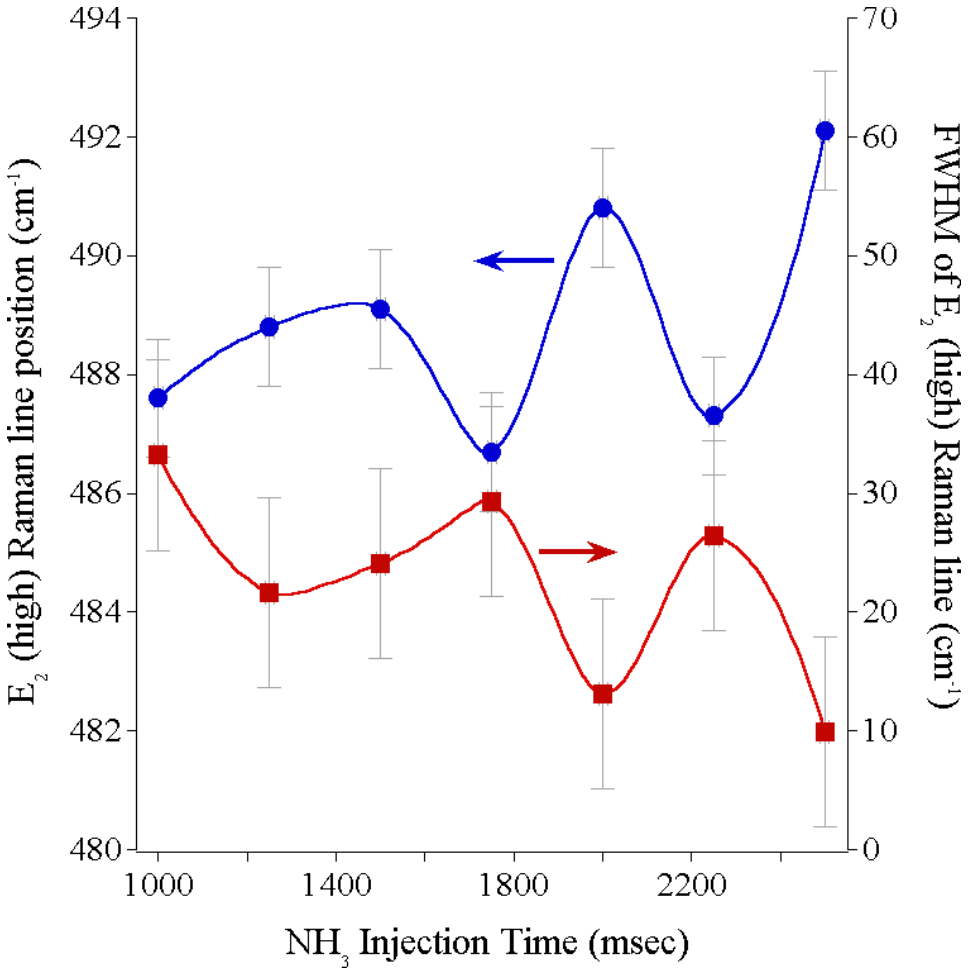

Figure 3.35 The position and FWHM of E_2(high) Raman line of InN layers on GaN/Sapphire (0001) as a function of NH_3 pulse injection time.

The strain effect on phonons can also be observed on InN layers grown on different substrates of different lattice mismatch to InN. Sapphire has higher lattice mismatch to InN than GaN. In Figure 3.36, the position of E_2(high) phonon line is demonstrated by changing NH_3 injection time for InN samples grown on GaN/Sapphire (0001) and Sapphire (0001) templates. Although the general trend of E_2(high) phonon line position on both curves is toward higher energies, the spectral positions of this phonon line stay at lower energies for the layers grown on Sapphire (0001) templates than those grown on GaN/Sapphire (0001). This is due to the suppression of strain effect by the GaN buffer layer.

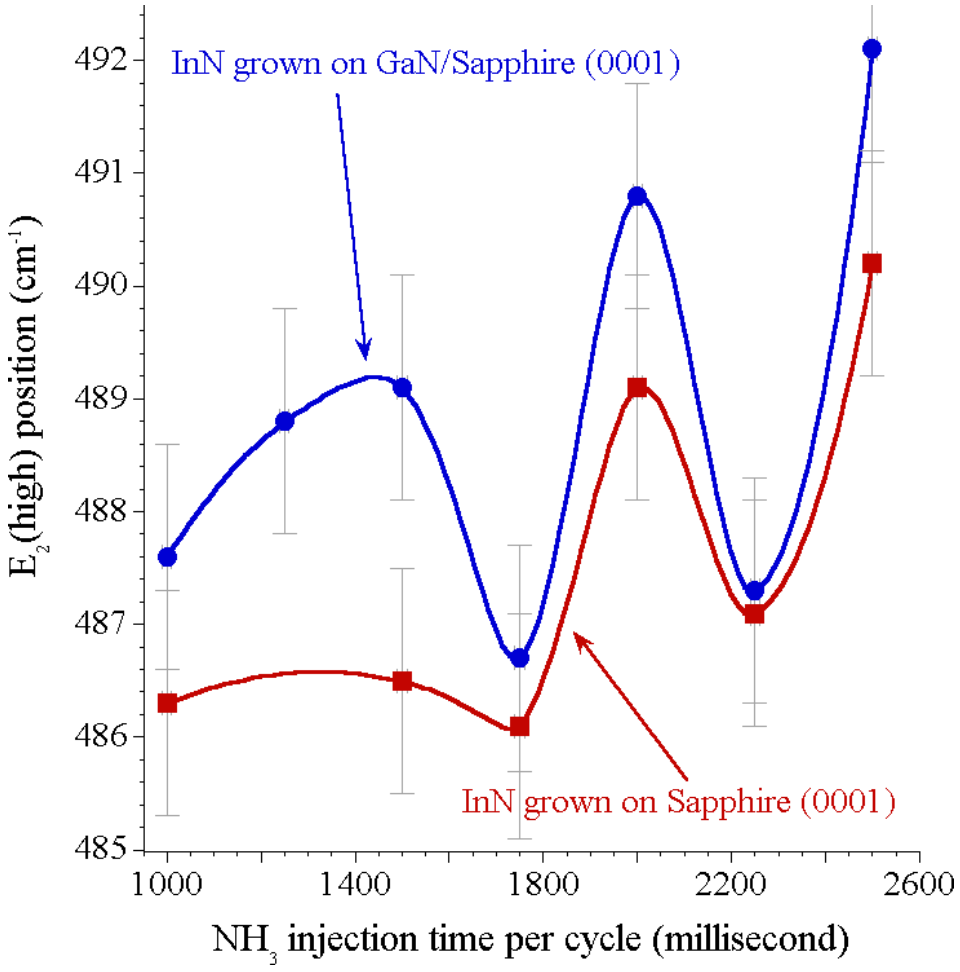

Figure 3.36 The spectral position of E_2(high) Raman line of InN layers grown on GaN/Sapphire and sapphire templates as a function of NH_3 pulse injection time.

In Figure 3.37, the correlation between the position and FWHM of the E_2(high) phonon line of InN samples grown on GaN/Sapphire (0001) templates is presented. This correlation suggests that E_2(high) phonon line shifts to higher wavenumber as sharpening due to strain relaxation.

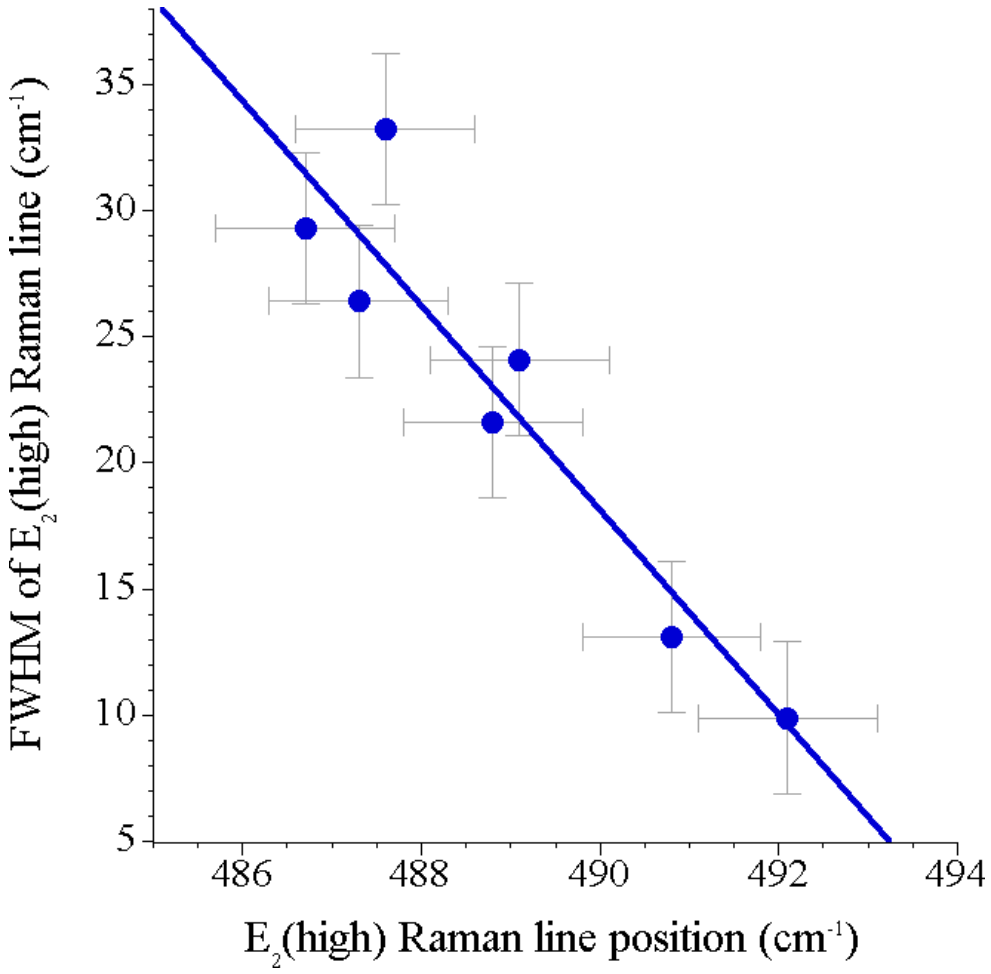

Figure 3.37 The FWHM versus the position of E_2(high) Raman line of InN layers on GaN/Sapphire (0001).

In Figure 3.38, the position and the FWHM of A_1(LO) phonon line of InN as a function of NH_3 pulse injection time is presented. A_1(LO) does not show a significant dependence to the variation of NH_3 pulse injection time. Furthermore, there is no correlation between the spectral position and the FWHM of this phonon line.

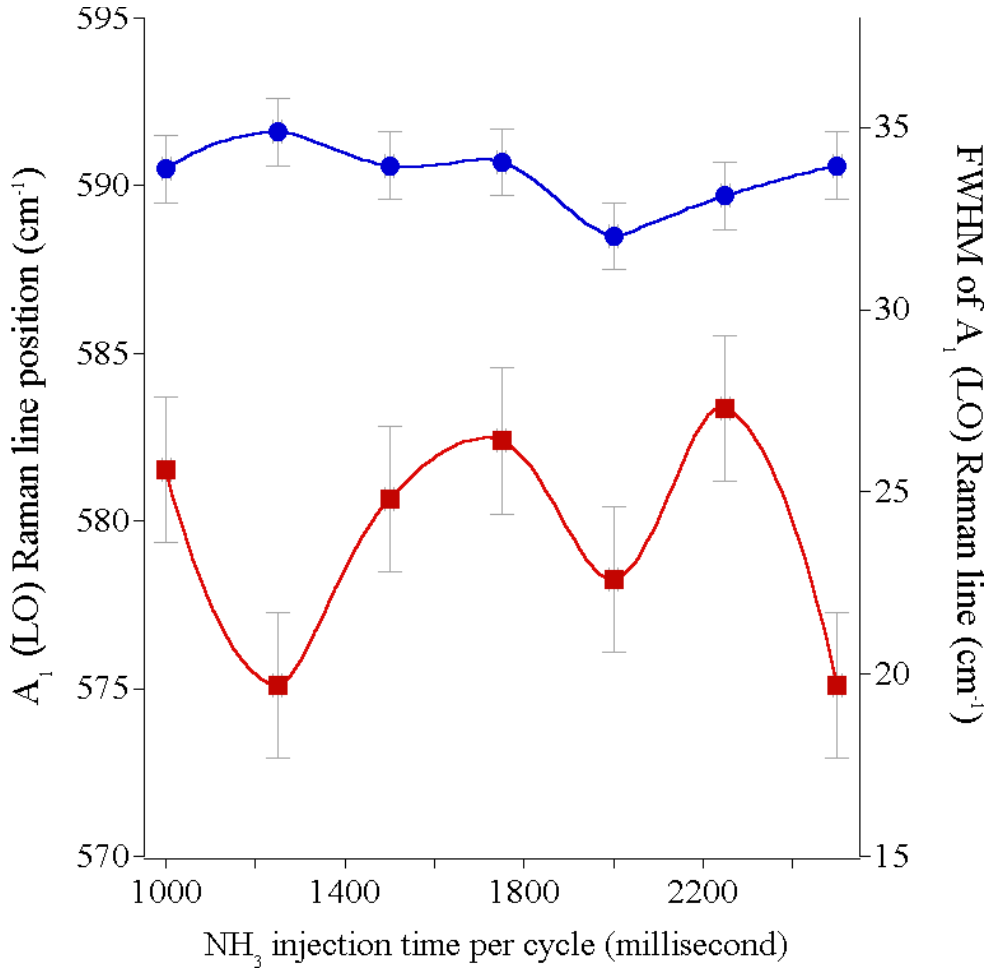

Figure 3.38 The position and FWHM of A_1(LO) Raman line of InN layers on GaN/Sapphire (0001) templates as a function of NH_3 pulse injection time.

The influence of NH_3 exposure time on surface morphological and structural properties of InN layers has been investigated. The dependence of the film thickness and average steady-state growth rate to NH_3 pulse injection time was almost linear suggesting that the consumption of Indium by NH_3 may not still be ~100%. The linear increase in the growth rate could indicate that the InN growth might be diffusion limited since a longer NH_3 injection pulse can increase the growth rate proportional to its exposure time and the amount of NH_3 injected to the growth surface is the same for all injection times. At 2500 ms, NH_3 pulse injection time, the average steady-state growth rate was about half a monolayer per cycle. The observations made on

E_2(high) phonons of InN revealed that the local crystalline quality increased by extending the NH_3 pulse injection time. Strain effect on phonons can also be observed on InN layers grown on different substrates of different lattice mismatch to InN. Sapphire has higher lattice mismatch to InN than GaN. The position of the E_2(high) phonon line of InN samples grown on both types of templates followed a similar fashion for changing NH_3 pulse injection time; however, the measured values for InN on GaN/Sapphire were higher than the ones on Sapphire due to less crystal strain. A_1(LO) phonon mode did not show a significant dependence to the variation of NH_3 pulse injection time. Although there was a slight dependence of this phonon line shifting downward, it was hard to extract a result out of the picture since A_1(LO) phonons could be coupled by plasmons. In the next section, the results of plasmon and LO phonon coupling analysis are presented.

3.4.1.8 Plasmon coupling to LO phonons in InN

The plasmon coupling to the A_1(LO) mode of InN crystal has been investigated by employing simulations on the observed line-shape of this phonon mode on the Raman spectrum. The theory behind the simulation was detailed in 3.3.4.1. The interaction between phonon and plasmons has been studied in highly doped III-V semiconductors[180-185] including InN.

In the previous section, the phonon mode which was not informative enough about the changes in the crystalline quality of InN was A_1(LO). Because of the polar nature of this oscillation, the effect of plasmon coupling is present besides the crystal strain effect. Consequently, this coupling is advantageous to quantify plasmon related the properties such as, free carrier concentration since the A_1(LO) phonons strongly interacts with the conduction-band electrons broadening the line-shape of this phonon mode [185].

In order to estimate the free electron concentration, the spectral peak corresponding to A_1(LO) phonon line was determined using Lorentzian peak fitting and, then, this peak was reconstructed numerically using the Linhard–Mermin dielectric function. In this approach, the dielectric function consists of high frequency, plasmon and phonon contributors. The best fit to experimental line-shape of the A_1(LO) phonon mode was obtained for DP+EO (Deformation Potential with Allowed Electro-optics) scattering mechanism. The effective mass m_{eff} was set to 0.14 m_0, noting that this will slightly underestimate the free carrier concentration[186]. The best-fit approximation for an InN layer grown on GaN/Sapphire template is presented in Figure 3.39.

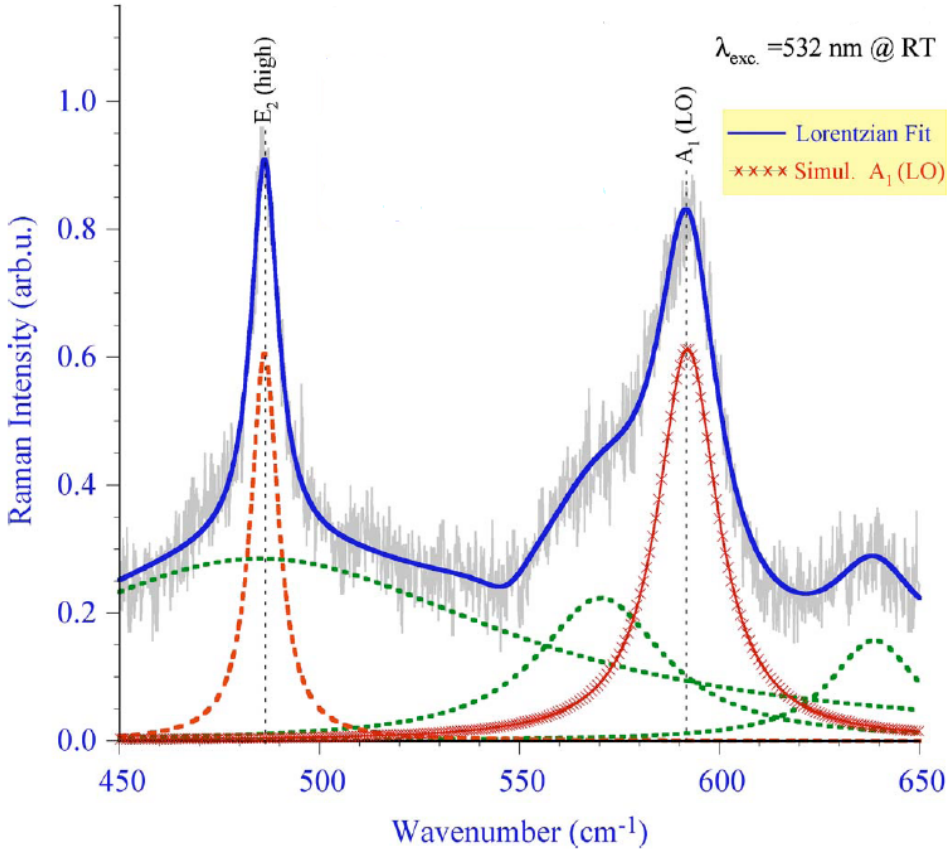

Figure 3.39 The experimental Raman spectra with the curve fit. The dashed peaks are the Lorentzian components of the curve fit. Simulated A_1(LO) peak is presented using the cross type variable markers.

The results of the simulations and the XRD analysis are summarized in Table 3.12. The XRD analysis revealed the epitaxial and single-phase InN layers with hexagonal symmetry and the FWHM of 202 arcseconds of (0002) Bragg reflection peak. The Raman analysis exhibited high crystalline quality by a sharp E_2(high) Raman peak of FWHM of 8.3 cm^{-1}. The observed line-shape of A_1(LO) phonon line in the Raman spectrum was simulated and the free carrier concentration was estimated as $2.5x10^{18}$ cm^{-3}.

Table 3.12 Summary of the results obtained from XRD analysis and simulations on plasmon-phonon coupling.

XRD (0002) Position (deg)	XRD (0002) FWHM (arcsec)	Raman E_2(high) Position (cm^{-1})	Raman E_2(high) FWHM (cm^{-1})	Raman A_1(LO) Position (cm^{-1})	Raman A_1(LO) FWHM (cm^{-1})	Free carrier concentration from A_1(LO) simulations
31.34	202	486.3	8.3	591.9	18.2	$2.5x10^{18}$

The free carrier concentration estimations obtained from A_1(LO) phonon line simulations have been compared to the estimations from infrared reflection spectra simulations using the method described in 3.3.4.2. InN samples, A and B, have been grown on GaN/Sapphire (0001) and Sapphire (0001) templates, respectively. Corresponding Raman spectra for these samples along with the Lorentzian curve fitting parameters and simulated spectra are presented in Figure 3.42.a-b for samples A and B, respectively. The FWHM of E_2(high) phonon line is smaller for the InN layer grown on GaN/Sapphire (0001) template.

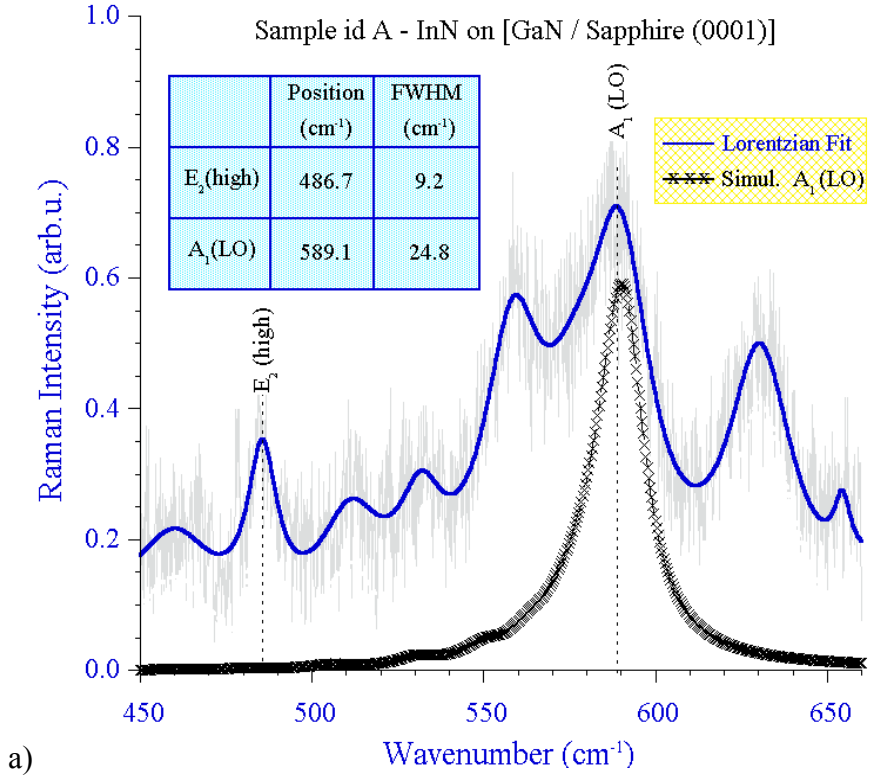

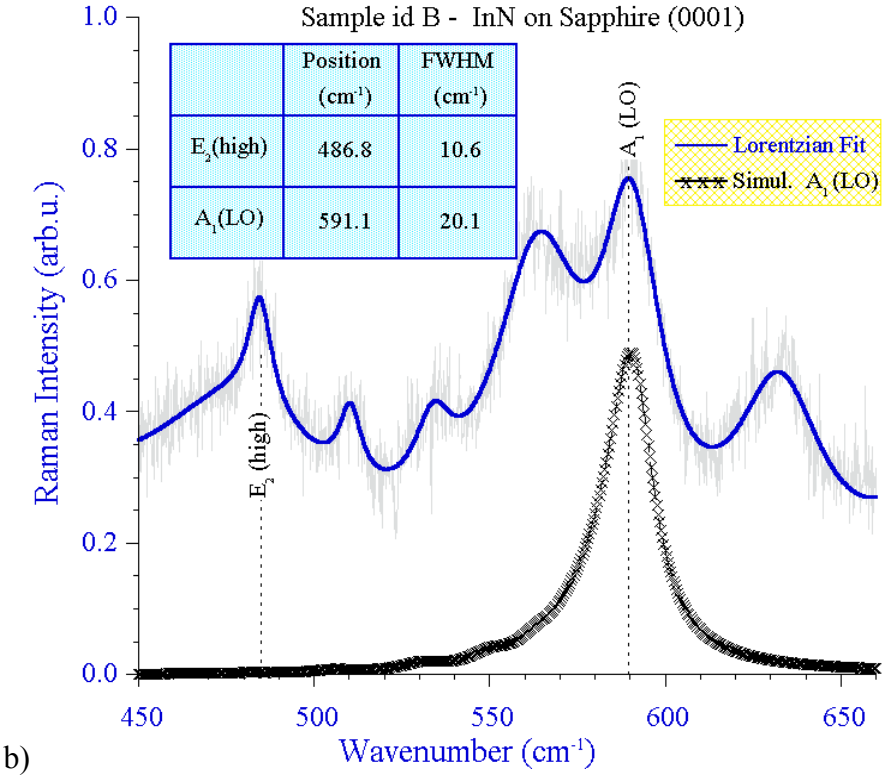

Figure 3.40 Raman spectra and simulated A_1(LO) phonon mode of InN samples (a)A and (b) B. [187].

Experimental and simulated IR spectra of the samples are shown in Figure 3.43. The interference oscillations observed in IR spectra of sample A is due to the GaN buffer layer in template. The horizontal line indicates the base line for the IR spectra of sample B.

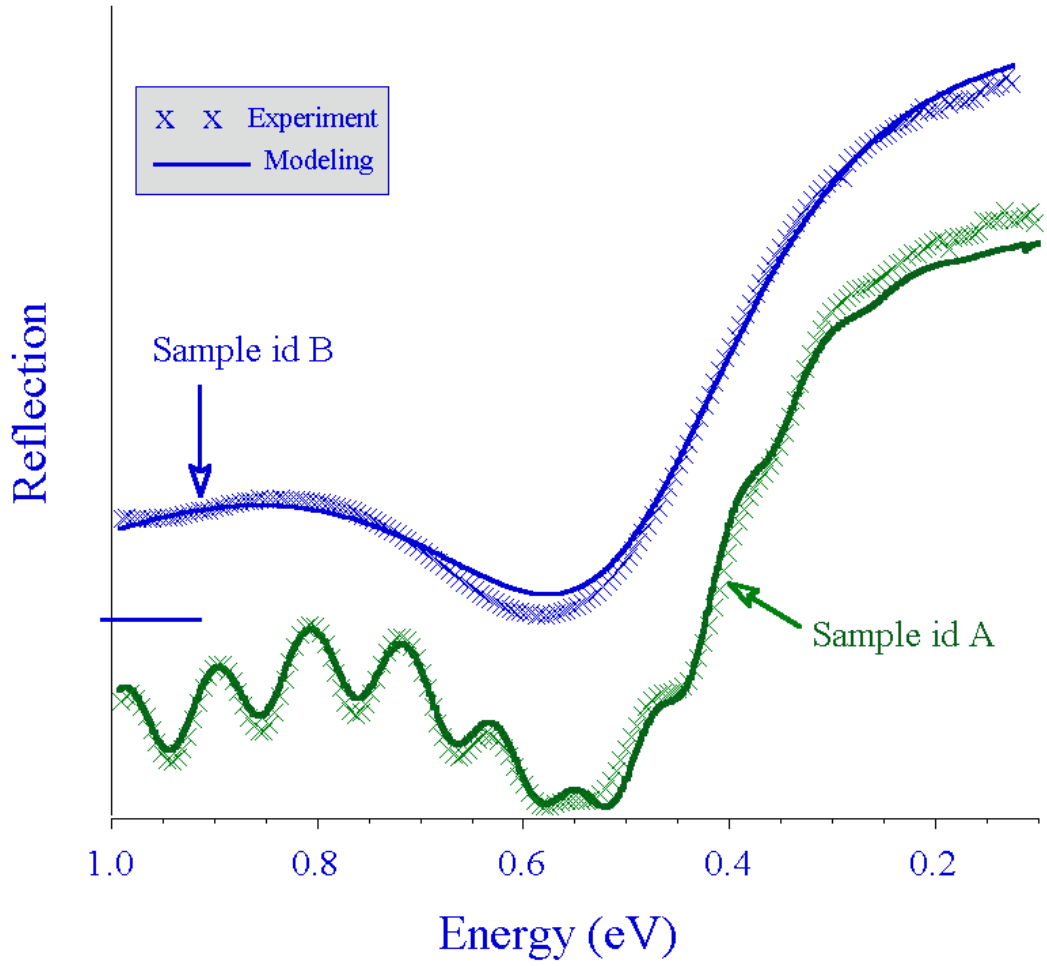

Figure 3.41 Experimental and simulated IR spectra of InN samples A and B. [187]

The estimations on high-frequency dielectric function (ε_∞), plasma frequency (ω_p) and free carrier concentration (n) by simulating Raman spectra and IR spectra are summarized in Table 3.13.

Table 3.13 Summary of the results obtained from XRD analysis and simulations on plasmon-phonon coupling.

Sample	A		B	
	Raman	IR	Raman	IR
ε_∞	8.3	7.5	8.6	7.1
ω_p (cm^{-1})	3441	3494	3907	3720
n (cm^{-3})	$1.0\ 10^{20}$	$9.0\ 10^{19}$	$1.04\ 10^{20}$	$1.0\ 10^{20}$

The dielectric constant acquired from IR analysis is lower than that acquired from Raman analysis. This could be due to larger effect of surface morphology. In infrared reflectance experiments, the spectra are obtained from an area larger than Raman experiments. Probing larger area in reflection mode could result in higher contribution from effective surface medium approximating the dielectric constant to smaller values as a result of the surface voids introduced by the surface morphology. The free carrier concentration estimations from both analyses are close to each other. However, it should be noted that in IR reflectance calculations, the contribution from the effective medium and in Raman analyses, the contributions from the crystal strain effect are neglected.

3.4.2 Indium Gallium Nitride (InGaN) layers

The significance of InGaN material system for designing advanced device structures has been summarized in section 3.1.1. Up to date, there have not been detailed studies reported on the surface morphological properties of InGaN and their correlation to structural properties.

3.4.2.1 The effects of composition on surface morphology

In order to investigate the influence of composition on surface morphological properties, $In_{1-x}Ga_xN$ layers have been grown in the incorporation range between 0.12 and 0.59.

The $In_{1-x}Ga_xN$ layers investigated have been grown by HPCVD on GaN/Sapphire (0001) templates. The pulse separation S2 (see Figure 3.32) was set to 1400 msec. The mixture of TMI and TMG precursors was pulsed for 800 msec and NH_3 precursor was pulsed for 1500 msec at every growth cycle. V-III ratio was set to 1300. Growth temperatures were 880 ^oC and 720 ^oC for the lower and the upper heaters, respectively. The experimental conditions for all samples were kept the same but the incorporation x.

The AFM images of the $In_{1-x}Ga_xN$ layers are shown in Figure 3.42a-e for gallium incorporation of 0.12, 0.19, 0.35, 0.47, and 0.59 respectively. The AFM images are in oblique view and corresponding z-scale is placed next to each image.

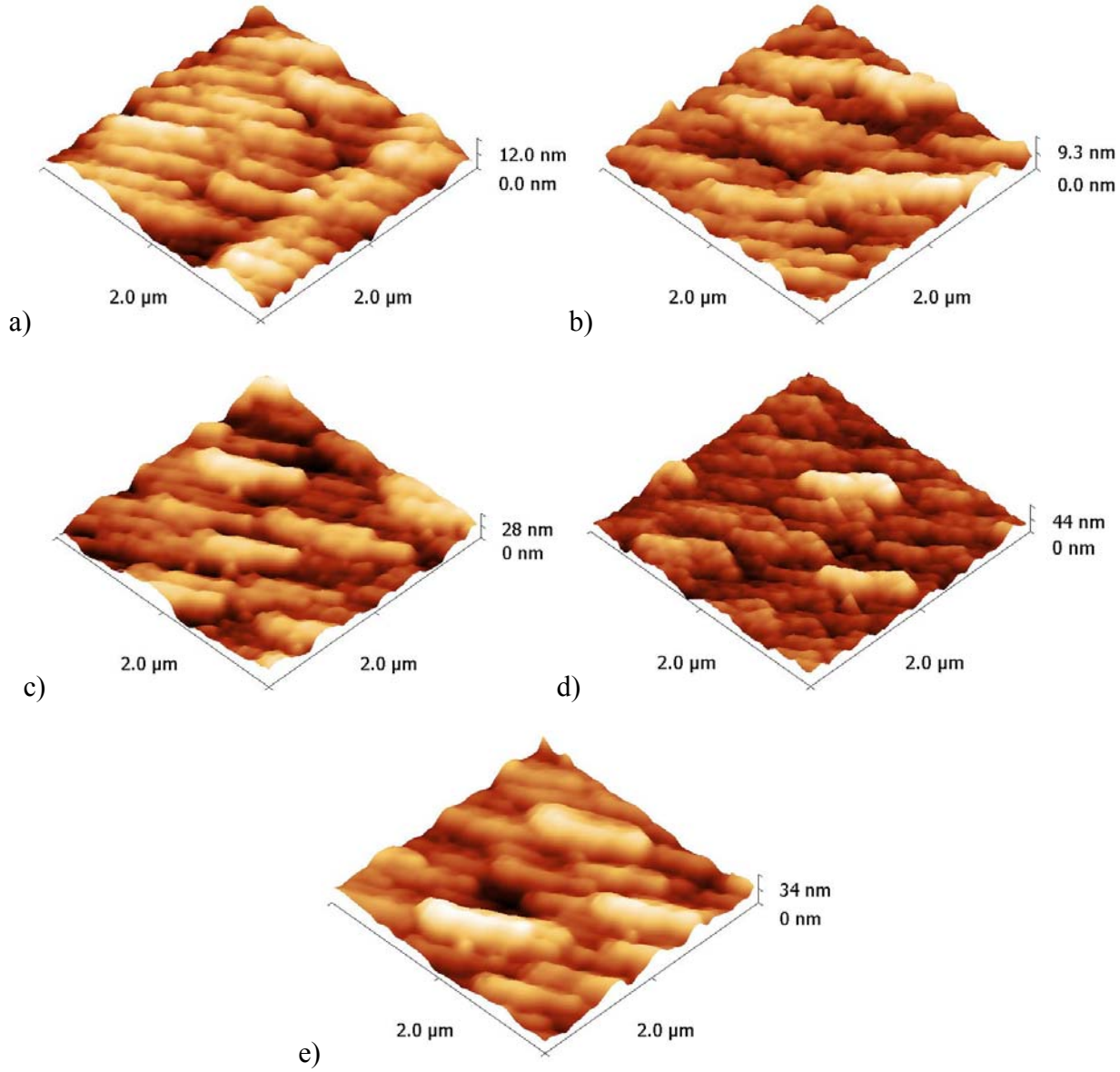

Figure 3.42 2µm x 2µm AFM images $In_{(1-x)}Ga_xN$ layers grown on GaN/Sapphire (0001) templates, a) x=0.12 , b) x=0.19, c) x=0.35, d) x=0.47, e) x=0.59

In Figure 3.43, the surface roughness of the $In_{1-x}Ga_xN$ layers are presented as a function of gallium incorporation. At low compositions (x < 0.20>, very smooth surfaces were obtained. By the increasing composition, surface of the $In_{1-x}Ga_xN$ layers became roughened. At composition of 0.6, the surface roughness is almost tripled as compared to the composition of 0.10.

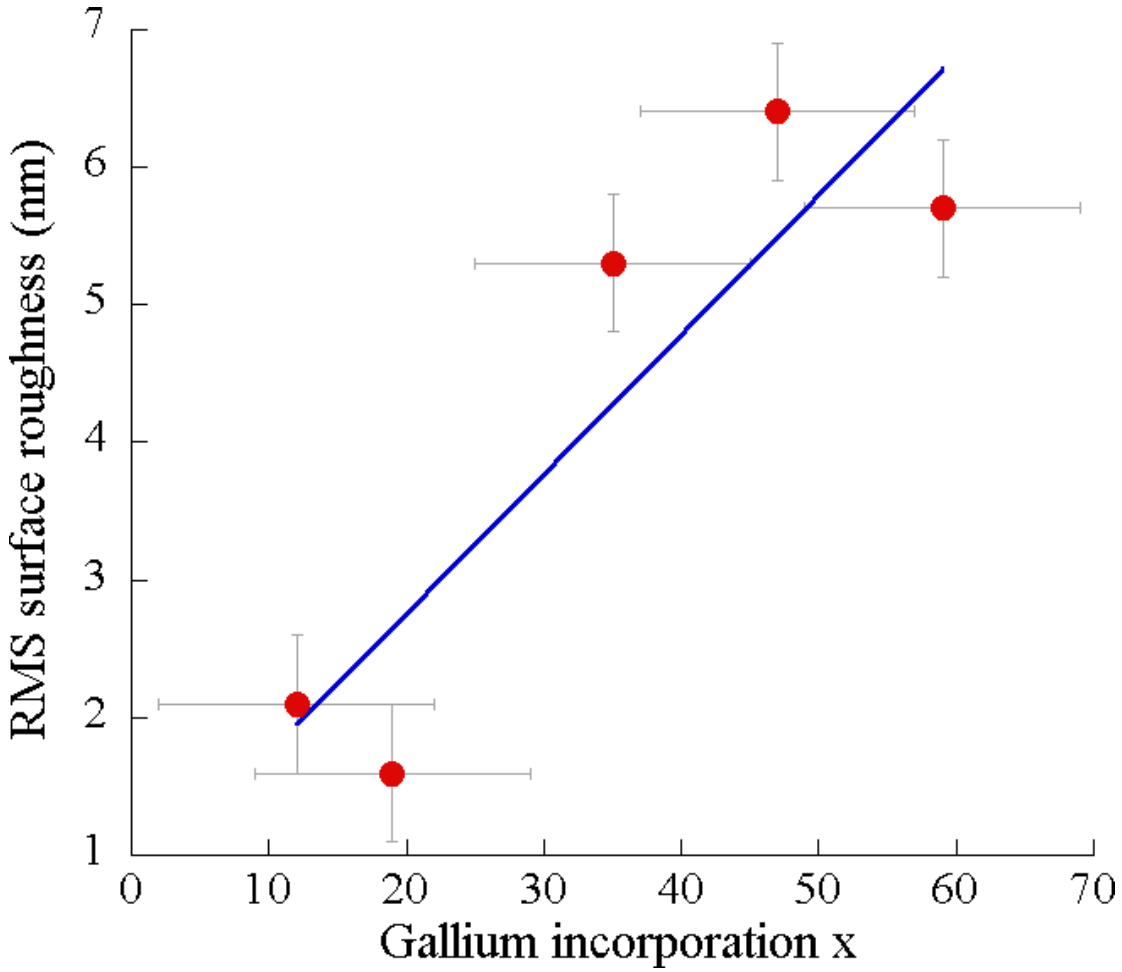

Figure 3.43 Surface roughness versus gallium incorporation in $In_{1-x}Ga_xN$ layers grown on GaN/Sapphire (0001) templates.

The results of this analysis suggest that increasing gallium incorporation results in surface roughening. This could be due to the strain effect introduced by incorporation of more gallium. The binary GaN system is processed at higher temperatures than InN. Therefore, increased gallium incorporation in $In_{1-x}Ga_xN$ could require variable growth temperature as a function of composition.

3.4.2.2 Effects of the group V/III molar ratio

The influence of the group V/III molar precursor ratio on the surface morphological and electrical properties of $In_{0.65}Ga_{0.35}N$ epilayers has been investigated. The layers studied have been grown by high-pressure Chemical Vapor Deposition, a growth technique that utilizes the reactor pressure as an additional processing parameter. The surface morphology analysis revealed that with the increasing V/III molar precursor ratio, the surface morphology degrades with increasing surface roughness and decreasing average grain areas. The free carrier concentration in the $In_{0.65}Ga_{0.35}N$ epilayers increased with the increased group V/III molar precursor ratios in the 700-3000 range.

Introduction

The ternary $In_{1-x}Ga_xN$ alloy system is being explored for advanced optoelectronics[188] and high–efficient photovoltaic[116,14,16,18] applications. Devices based on indium-rich and gallium-rich $In_{1-x}Ga_xN$ heterostructures have the potential to operate in a wide spectral range from UV (E_g^{GaN}=3.4 eV) to NIR (E_g^{InN}=0.7eV). However, the growth of $In_{1-x}Ga_xN$ alloys is challenging due to the low thermal disassociation temperature of InN compared to that of GaN, as well as the high lattice mismatch between the two binaries.

The high n-type background doping levels observed in most InN layers have been partially attributed to interstitial hydrogen atoms by the theoretical[189] and the experimental studies[190-192]. Ruffenach, et al.[192] showed that the thermal annealing of InN layers at 550 °C under NH_3 atmosphere resulted in an increased free carrier concentration, a process which was reversible. In order to study the influence of the group V/III molar precursor ratio on the surface morphological, structural and electrical properties of $In_{0.65}Ga_{0.35}N$ epilayers grown by High-

Pressure Chemical Vapour Deposition (HPCVD), a set of epilayers with different group V/III molar precursor ratios ranging from 700 to 3000 was grown and analyzed. The surface morphology and free carrier concentration of the epilayers have been studied by Atomic Force Microscopy (AFM) and Infrared Reflectance Spectroscopy (IRS).The HPCVD growth technique is explored in order to assess the stabilization of alloys with large differences in the partial pressures at higher processing temperatures. This is especially important for the InN-GaN ternary alloy system, where the different partial pressures lead to significant differences in growth temperatures between the two binaries.

Experimental details

The $In_{1-x}Ga_xN$ layers investigated were grown by HPCVD on ~5 μm thick GaN / c-plane sapphire templates. Active indium, gallium and nitrogen fragments were supplied to the growth surface via Trimethylindium (TMI), Trimethylgallium (TMG), and Ammonia (NH_3) precursors, respectively. As schematically illustrated in Figure 3.44, the precursors were temporally embedded in a nitrogen carrier gas stream, such that the total flow and pressure remained constant at any given time. The ammonia and (TMI, TMG) injection times were 1.5 sec and 0.8 sec, respectively, with pulse separations between TMI/TMG - ammonia and ammonia - TMI/TMG set to 1.4 sec and 2.3 sec, respectively. The $In_{0.65}Ga_{0.35}N$ epilayers were grown at a temperature of 1150 K, a reactor pressure of 15 bar, a main gas carrier flow (N_2) of 12 slm (standard liters per minute), and a growth time of 3 hrs. For the series presented here, all parameters were kept constant, while V/III molar precursor ratio was varied between 700 and 3000. The surface morphology of the layers was analyzed by AFM using a 'XE 100 Park'

system in non-contact mode. The AFM tips used in the AFM experiments had a resonance frequency of 300 kHz and a spring constant of 45N/m.

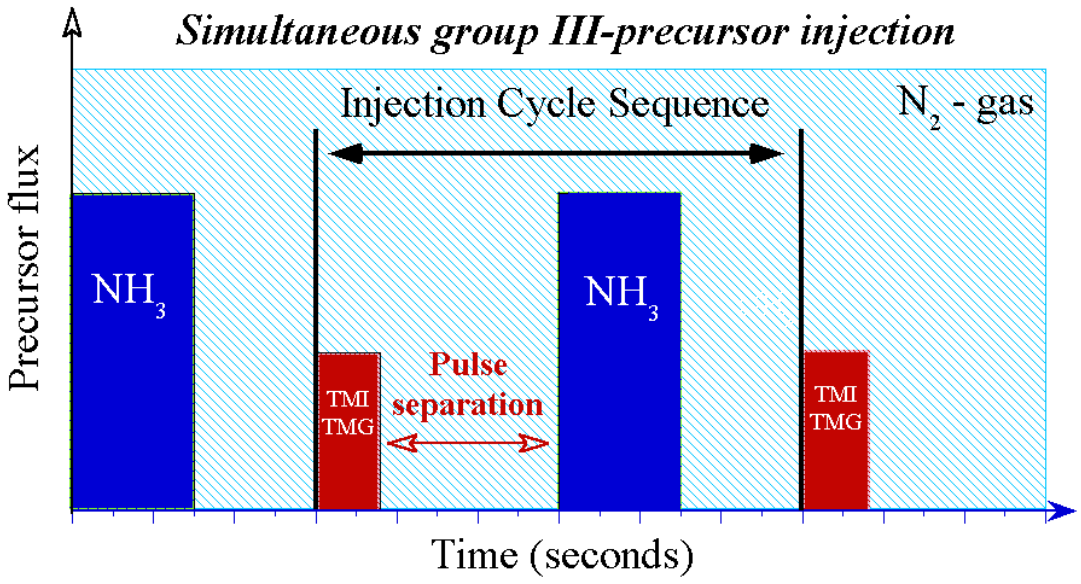

Figure 3.44 The pulsed injection sequence employed for $In_{1-x}Ga_xN$ growth.

For IR reflectance, a Perkin-Elmer 2000 system was used. The experiments were carried out at room temperature in the energy range of 0.062–0.744 eV in near normal incidence geometry. The plasma frequency and free carrier concentration of $In_{0.65}Ga_{0.35}N$ layers were obtained by fitting the simulated IR spectra to the experimental spectra. The simulated spectra were constructed by using optical transfer matrices and a four-layer stack model consisting of sapphire substrate, an i-GaN layer, a p-GaN interface layer, and an InGaN layer from bottom to top. The InGaN dielectric function employed in these calculations is based on coupled contributions from plasma oscillations by classical Drude model and phonons by Lorentzian type oscillator model [146,193]. The dielectric function for the sapphire substrate was calculated by using Sellmeier equation[194]. The effective electron mass used for the InGaN layer calculations was 0.15 m_o [195].

Results and discussion

Figure 3.45 a - d show 2µm x 2µm AFM images of the $In_{0.65}Ga_{0.35}N$ layers grown with group V/III molar precursor ratios of 700, 1000, 2000, and 3000, respectively. The statistical analyses for the surface roughness, average grain area, grain size distribution, and surface void fraction as function of the V/III molar precursor ratio are summarized in Table 3.14. The results show that the surface roughness increases with the increasing V/III molar precursor ratio, indicating a degradation of surface quality. The decrease in the average grain area with increased V/III molar precursor ratio suggests an increase in extended defects for higher V/III molar precursor ratios. The increased group V/III molar precursor ratio resulted in decreased amount of surface voids.

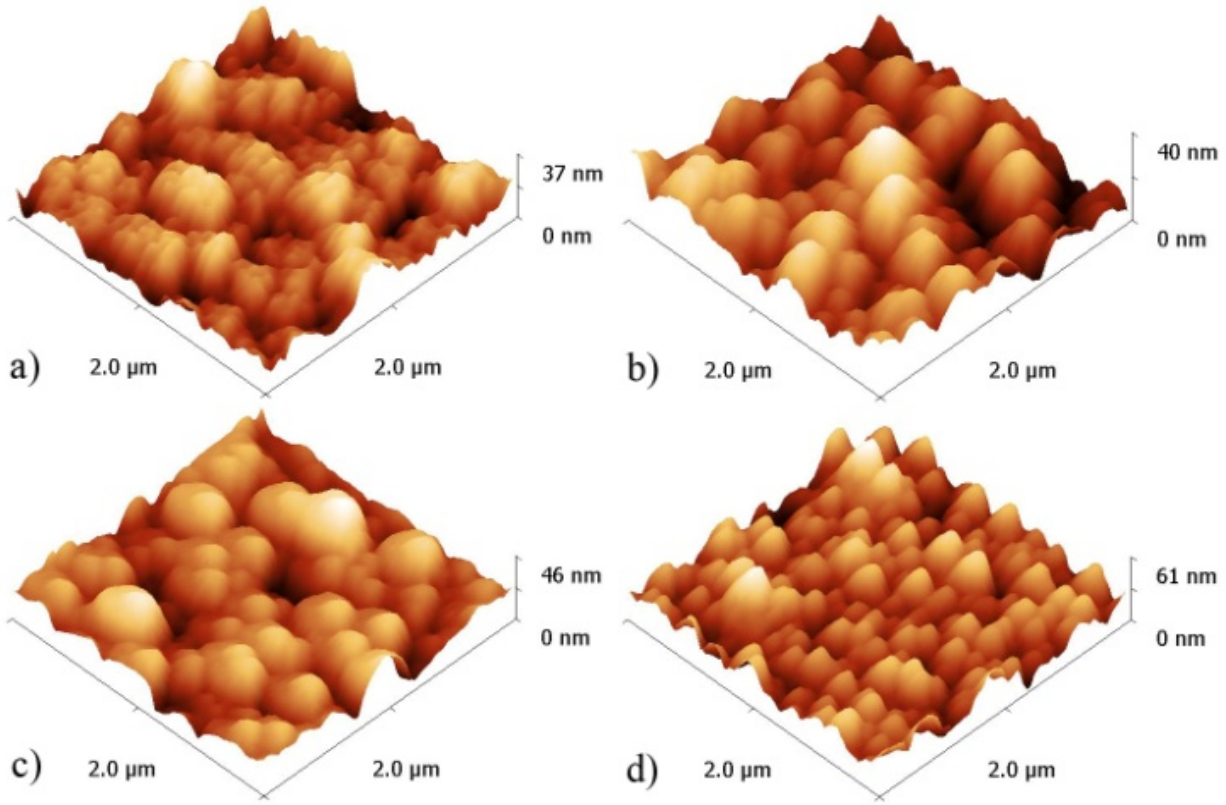

Figure 3.45 2µm x 2µm AFM images of $In_{65}Ga_{35}N$ layers on GaN/Sapphire (0001) templates. The layers were grown by V/III molar ratios of a) 700, b) 1000, c) 2000, d) 3000.

Table 3.14 Summary of the results obtained from AFM analysis of $In_{0.65}Ga_{0.35}N$ layers grown with different V/III molar ratios

V/III molar ratio	700	1000	2000	3000
Surface roughness (nm)	6.9	7.3	7.9	8.7
Ave. grain area (10^{-2} μm^2)	7.3	6.9	3.5	1.8
Standard deviation of grain size distribution (10^{-2} μm^2)	9.5	9.3	4.9	2.4
Surface void fraction (%)	37	42	36	32

The IR reflectance spectra obtained for the $In_{0.65}Ga_{0.35}N$ epilayers grown with group V/III molar precursor ratios ranging from 700 to 3000 are depicted in Figure 3.46. The IR reflectance spectra show a clear shift of the plasma frequency with increasing group V/III molar precursor ratio. The estimated free carrier concentrations from the IR simulation analyses are depicted in the inset of the figure.

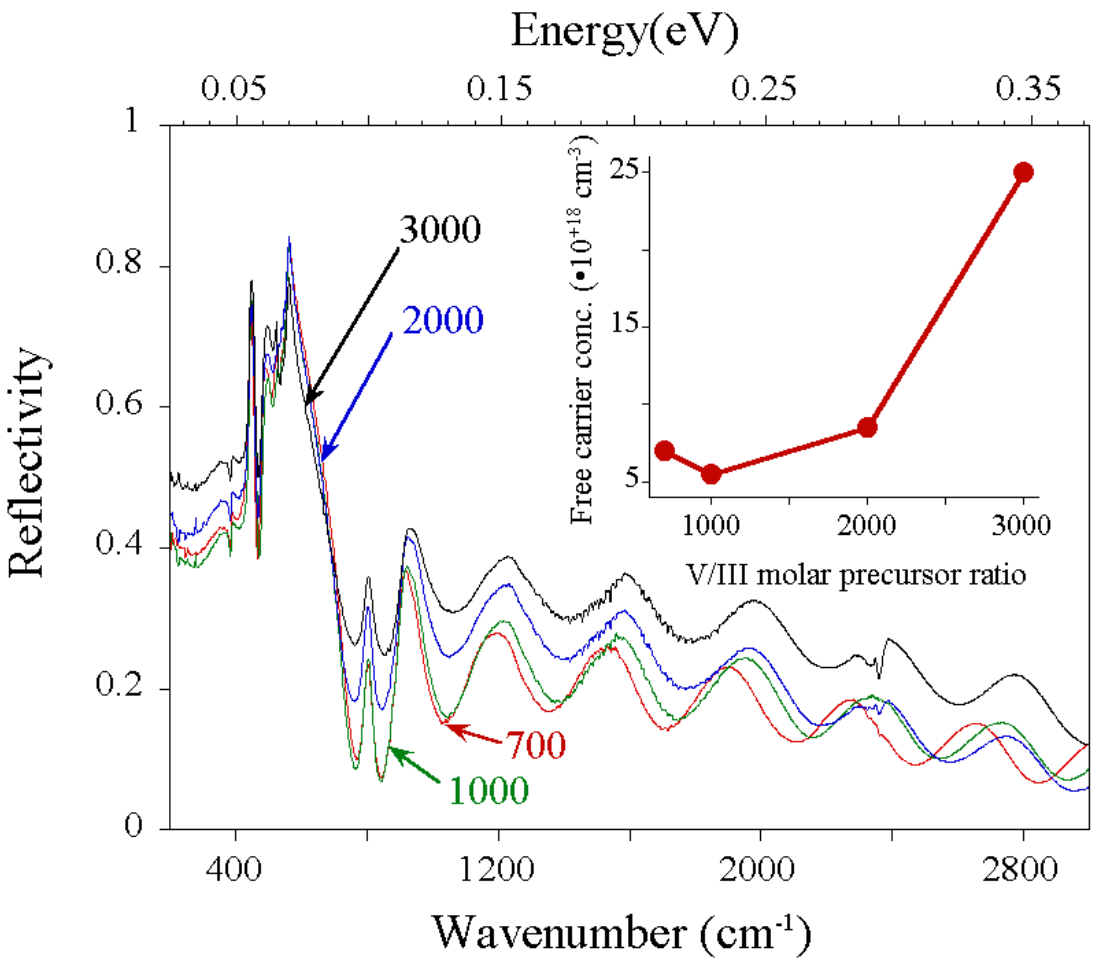

Figure 3.46 IR reflectance spectra of $In_{0.65}Ga_{0.35}N$ layers grown with different group V/III molar ratios varying between 700 and 3000. Inset plot shows free carrier concentration estimate as a function of the group V/III molar precursor ratio.

The analysis shows an increase in the free carrier concentration with increasing group V/III molar precursor ratio from 700 to 3000, a tendency that might be related to the increased hydrogen concentration at the growth surface, with potential incorporation in the layers as reported for InN [189-192]. A further potential contribution to the increased free carrier concentration with higher V/III molar precursor ratio (see Table 3.14) might be the decreased average grain area, since a higher concentration of grain boundaries may induce a higher density of edge-type threading dislocations that may contribute to a higher n-type doping as observed in MOCVD

grown InN layers [196]. The best fitting parameters obtained from simulations of the experimental IR spectra are summarized in Table 3.15.

Table 3.15 Summary of the results obtained from IR reflectance for $In_{0.65}Ga_{0.35}N$ layers grown with different V/III molar ratios

V/III molar ratio	700	1000	2000	3000
Plasma frequency (cm^{-1})	800	550	1050	1150
Free carrier concentr. (10^{18} cm^{-3})	7	5.5	8.5	25
High frequency dielectric const. ε_∞	4.8	4.7	4.8	6.0

The increase in the dielectric function ε_∞ with increasing V/III molar precursor ratio suggests the formation of a denser layer for higher group V/III molar ratios. According to Bruggeman's effective medium approximation[197], the inclusion of void components lowers the dielectric constant ε. As depicted in Table 3.14, a decrease in surface void fraction is observed with increasing group V/III molar precursor ratio. Assuming that the void component is completely related to the surface morphology, a direct correlation between effective dielectric constant ε_∞ and surface void fraction is observed. Further studies in a wider range of V/III molar precursor ratios are needed to improve the material quality in this composition regime.

Conclusions and summary

The influence of the group V/III molar precursor ratio on the surface morphological and electrical properties of the $In_{0.65}Ga_{0.35}N$ epilayers was studied. An increased group V/III molar precursor ratio from 700 to 3000 resulted in a higher free carrier concentration with a higher

surface roughness, a smaller average grain area, and a denser layer. The increase in the free carrier concentration is thought to be due to the higher hydrogen concentration at the growth surface, related to the increased amount of ammonia in the gas phase and/or increased amount of grain boundaries.

3.4.2.3 Effects of growth temperature on InGaN layers

The influence of the growth temperature on the phase stability and composition of single phase $In_{1-x}Ga_xN$ epilayers has been studied. The $In_{1-x}Ga_xN$ epilayers were grown by high-pressure Chemical Vapor Deposition with nominally composition of x = 0.6 at a reactor pressure of 15 bar at various growth temperatures. The layers were analyzed by x-ray diffraction, optical transmission spectroscopy, atomic force microscopy, and Raman spectroscopy. The results showed that a growth temperature of 925 °C led to the best single phase InGaN layers with the smoothest surface and smallest grain areas.

Introduction

The ternary $In_{1-x}Ga_xN$ alloy system attracts significant attention due to its unique physical properties such as direct band-gap, high carrier mobility, and strong chemical bonding[64,116]. The optical band gap of the $In_{1-x}Ga_xN$ alloy system can be tuned from ultraviolet (Eg GaN=3.4 eV) to near-infrared (Eg InN=0.7eV), spanning over more than 80% of the solar spectrum. This is of interest for the development of high-efficiency monolithic multijunction photovoltaic solar cells based on $In_{1-x}Ga_xN$ / $Ga_{1-x}In_xN$ heterostructures. However, the growth of the $In_{1-x}Ga_xN$ alloys and heterostructures is a challenge due to the lower disassociation temperature of InN compared to that of GaN. A further challenge is the large difference between the lattice constants of the

binaries InN and GaN [83] (~11%), which may induce lattice strain [127] and contribute to a potential solid-phase miscibility gap in the ternary $In_{1-x}Ga_xN$ system [126]. These facts contribute to the reported compositional inhomogeneity observed in InGaN layers [198,129,130,199-201], which reduces the device efficiencies of InGaN based optoelectronic structures.

The phase stability of InGaN epilayers has been studied for different growth temperatures with different growth techniques [129,200,201]. For instance, InGaN layers grown by RF-MBE show a linear correlation between gallium incorporationwith increased growth temperature between 600°C - 700°C [208]. MOVPE grown InGaN layers exhibited a similar behavior in the temperature range between 700°C - 850°C [86]. Pantha et al.[129] reported the growth of single phase InGaN layers by MOCVD and observed decreased indium incorporation with increasing growth temperature from 600°C - 750°C. This research effort explores the potential of high pressure Chemical Vapor Deposition (HPCVD) to improve the phase stability in InGaN layers, utilizing high pressures nitrogen gas to stabilize the $In_{1-x}Ga_xN$ growth surface and effectively suppressing the thermal decomposition process above the growth surface[141,142]. This contribution focuses on the characterization of a set of single-phase $In_{1-x}Ga_xN$ layers that were grown under identical growth conditions, varying the growth temperature only. X-Ray Diffraction (XRD), Optical Transmission Spectroscopy (OTS), and Raman spectroscopy were used to analyze the structural and optical properties of the epilayers. The findings were linked to the surface morphological properties of the $In_{1-x}Ga_xN$ layers.

Experimental details

The $In_{1-x}Ga_xN$ epilayers analyzed were grown by HPCVD on ~5 μm thick GaN/c-plane sapphire templates. Trimethylindium (TMI), Trimethylgallium (TMG) and ammonia (NH3)

precursors were used to provide active indium, gallium and nitrogen fragments respectively to the growth surface. As depicted in Figure 3.47, the precursors were provided to the growth surface via temporally controlled precursor pulses, which are embedded into the nitrogen main carrier gas stream. NH_3 and (TMI, TMG) injection times were 2.0 sec and 0.8 sec, respectively. The pulse separations between TMI/TMG - ammonia and between ammonia - TMI/TMG were set to 1.4 sec and 2.2 sec, respectively. The $In_{1-x}Ga_xN$ layers were grown at a reactor pressure of 15 bar, a nitrogen (N_2) main carrier gas flow of 12 slm (standard liters per minute), a group V-III molar precursor ratio of 1500, and a group III composition set value of x = 0.6. All experimental parameters were kept constant except the growth temperature, which was varied between 910°C and 960°C.

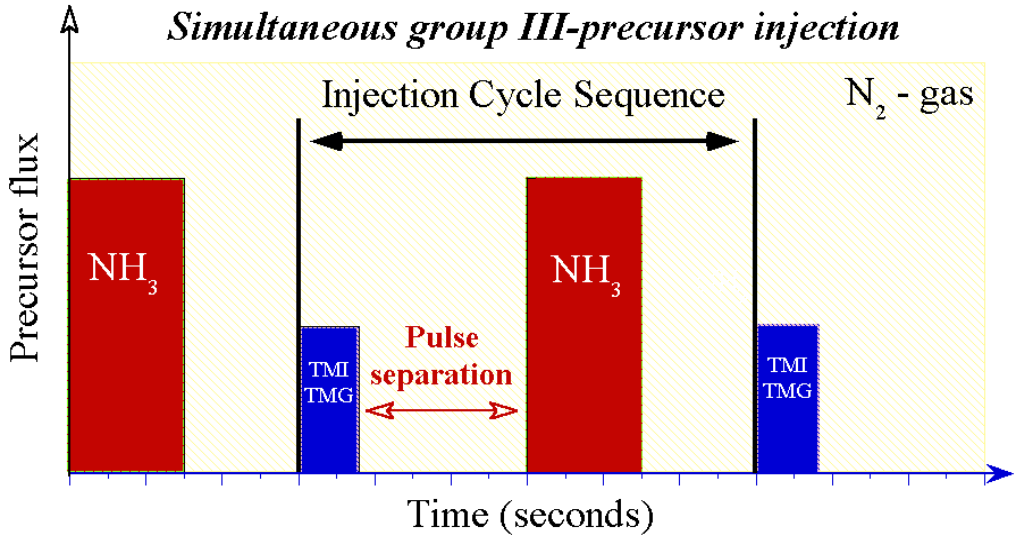

Figure 3.47. The pulsed injection sequence employed for $In_{1-x}Ga_xN$ growth.

XRD experiments were carried out utilizing an X`Pert PRO MPD (Philips) 4-circle diffractometer with a monochromatic X-ray (CuKα) source. XRD spectra were analyzed by Gaussian curve fitting to determine the position and Full Width Half Maximum (FWHM) of the

(0002) Bragg reflex. The position and corresponding miller indices of this Bragg reflex were evaluated together to calculate the lattice parameter '*c*' of the $In_{1-x}Ga_xN$ layers[83]. The composition of the $In_{1-x}Ga_xN$ epilayers were estimated using Vegard's law, which assumes a linear dependence of the ternary lattice parameters and their binaries alloys GaN and InN, respectively. Neglecting further any interfacial strain effects on XRD spectra, the lattice parameter 'c' can be expressed as

$$c_o^{\left(In_{1-x}Ga_xN\right)} = x \cdot c_o^{\left(GaN\right)} + \left(1-x\right) \cdot c_o^{\left(InN\right)} \tag{3.26}$$

In order to analyze the behavior of the absorption edge of $In_{1-x}Ga_xN$ layers for different growth temperatures, optical transmission experiments were carried out at room temperature using a UV-VIS-NIR spectrometer. The acquired optical transmission spectra were corrected for detector, monochromator and light source characteristics and normalized to the growth templates used. The optical absorption spectra (OAS) of the layers were calculated from the optical transmission spectra using Beer–Lambert's law in order to estimate the optical absorption edge of the $In_{1-x}Ga_xN$ alloys. The surface morphology of the layers was analyzed by Atomic Force Microscopy (AFM) using a 'XE 100 Park Systems' AFM in non-contact mode. The AFM tips used in the AFM experiments had a resonance frequency of 300 kHz and a spring constant of 45N/m. The phonon modes of the In1-xGaxN layers were studied by Raman spectroscopy in backscattering geometry (z(xx)z) using an excitation wavelength of 532nm. The Raman spectra were analyzed using a Lorentzian peak fitting algorithm in order to obtain peak positions and FWHM's values for the phonon modes.

Results and discussion

Figure 3.48.a shows 2Θ-ω scans for the $In_{1-x}Ga_xN$ layers with a nominally composition value x=0.60 grown at growth temperatures ranging from 910°C to 960°C. All epilayers exhibit single $In_{1-x}Ga_xN$ (0002) Bragg reflexes, indicating no macroscopic observable phase separations. The line-shapes and peak positions of the $In_{1-x}Ga_xN$ (0002) Bragg reflexes show a strong dependency with growth temperature. The line-shape and peak position analysis of these Bragg reflexes are summarized in Table 3.16. The $In_{1-x}Ga_xN$ layer grown at 925°C exhibited the most pronounced $In_{1-x}Ga_xN$ (0002) Bragg reflex. The estimated InGaN composition as a function of growth temperature is depicted in Figure 3.48.b. The red dashed line marks the experimental set-point, defined by the set values for the precursors TMI and TMG in the gas phase. Figure 3.48.b indicates a nonlinear correlation between the molar group III-ratio in the gas phase and bulk layer, with a closest match for 925°C for which the highest indium incorporation is observed.

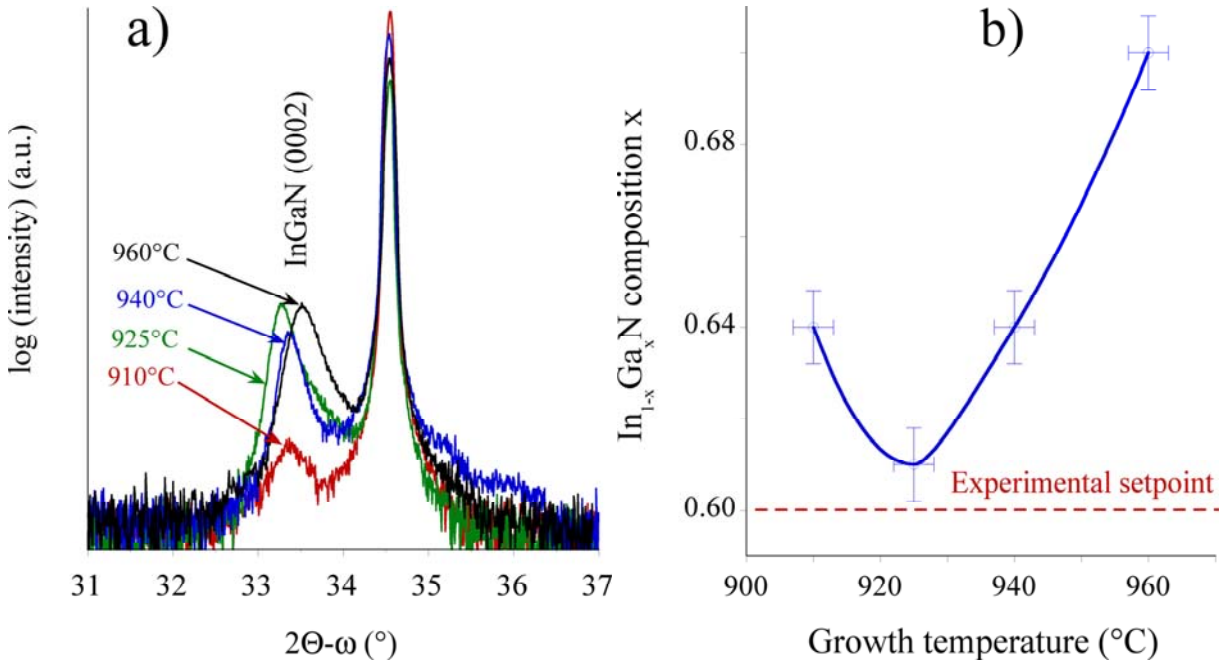

Figure 3.48. a)XRD patterns and b)optical absorption spectra of $In_{1-x}Ga_xN$ layers grown on GaN/c-sapphire templates with different growth temperatures varying from 910 °C to 960 °C.

The optical absorption spectra obtained for the $In_{1-x}Ga_xN$ epilayers grown at different temperatures are shown in Figure 3.49.a. As shown, the optical absorption edge changes as a function of the growth temperature. To quantify the absorption edge, a linear slope fit of the curves was used to obtain the intercept point with the energy axis. The calculated intercept values are plotted in Figure 3b as a function of the growth temperature. The estimate shows that the absorption-edge follows the indium composition behavior shown in Figure 3.48.b. The highest indium incorporation is observed for a growth temperature of 925°C with decreasing indium content as the growth temperature increases to 960°C.

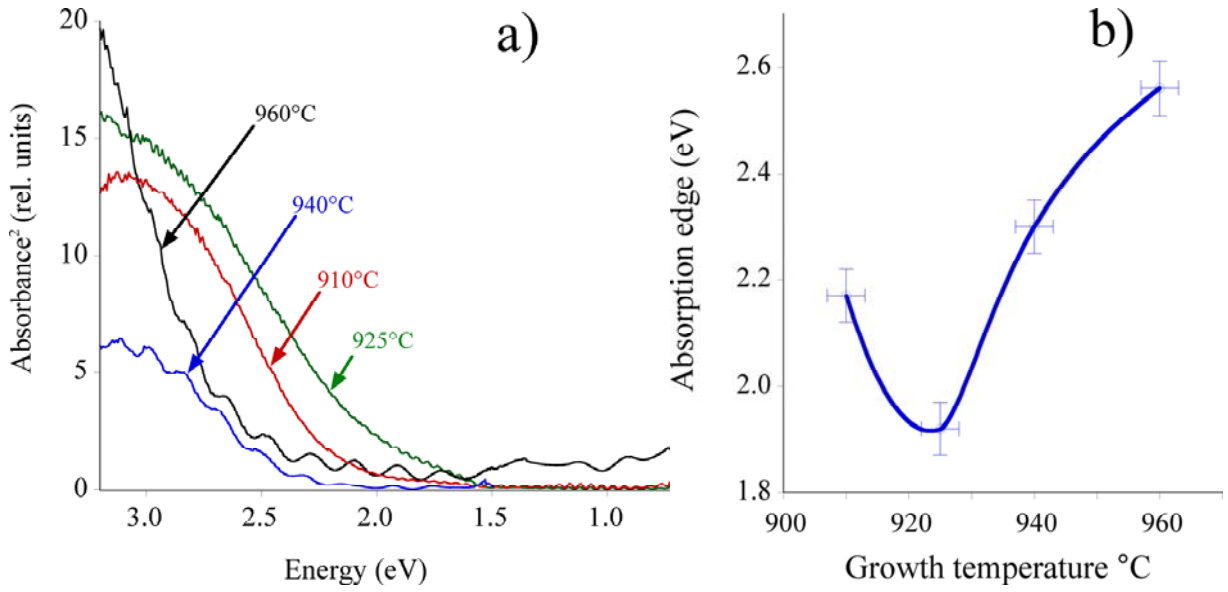

Figure 3.49. a) OAS spectra and b) calculated absorption edge of In1-xGaxN layers grown at different growth temperatures from 910 °C to 960 °C

Figure 3.50.a, b, c and, d depict 2µm x 2µm AFM images of the $In_{1-x}Ga_xN$ epilayers grown at 910°C, 925°C, 940°C, and 960°C, respectively. Statistical analysis techniques were used to calculate the surface roughness and average grain areas of these AFM images. The correlation of surface roughness and average grain area as function of growth temperature are

shown in the Figure 3.50.e. With increasing growth temperature from 910°C to 925° the surface roughness and average grain area decrease and then increase as the growth temperature increases to 960°C.

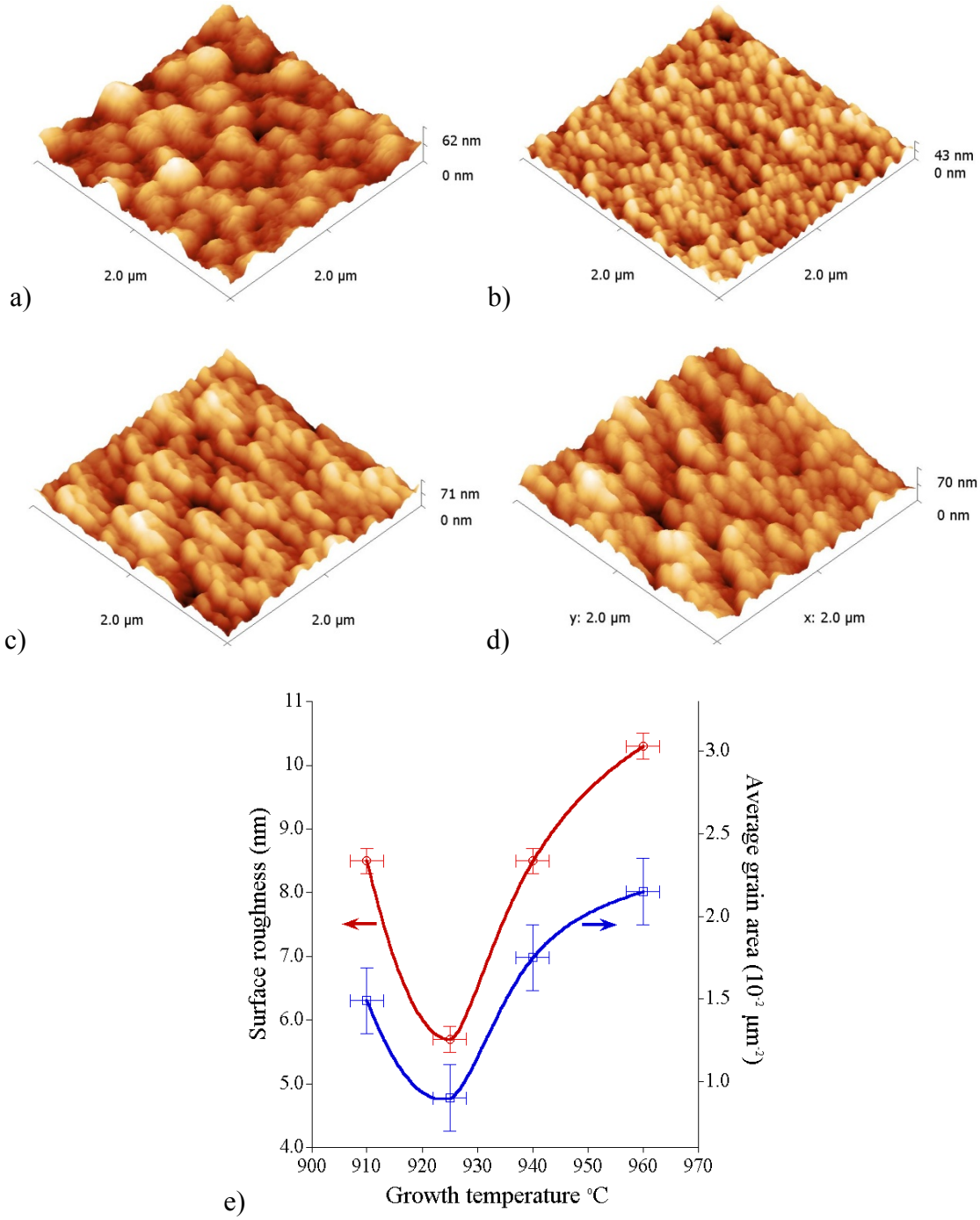

Figure 3.50 2µm x 2µm AFM images of $In_{1-x}Ga_xN$ layers grown at a) 910, b) 925, c) 940, d) 960 °C , e) Surface roughness and average grain area as a function of the growth temperature.

The Raman spectra for the $In_{1-x}Ga_xN$ epilayers are shown in Figure 3.51.a in the frequency region for the E_2 (high) and A_1 (LO) phonon modes. In wurtzite InN and GaN, the Raman phonon modes allowed in z(xx)z geometry along (0001) direction are A_1 (LO) and E_2 (high) [52]. The most distinct phonon mode observed in the Raman spectra is the A_1 (LO) mode, while the E_2 (high) mode is present, but not distinct enough to be statistically analyzed. The A_1 (LO) Raman line was fitted using two Lorentzian peaks side by side. The curve fitting results are summarized in Table 3.16 and variations in the peak positions as a function of growth temperature is depicted in Figure 3.51.b. As the growth temperature increases from 910°C to 925°C, both contributions in A_1 (LO) peak shift to lower wavenumbers. As the growth temperature increases further, both contributions in A_1 (LO) increase nonlinearly back to higher energies.

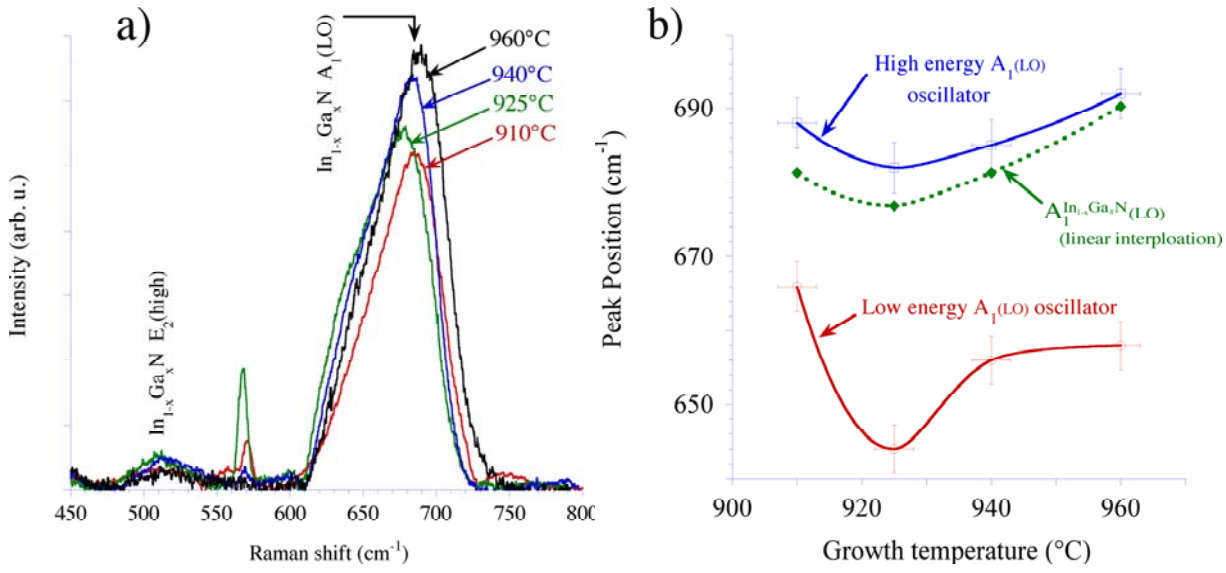

Figure 3.51 a) The results obtained from RS experiments on $In_{1-x}Ga_xN$ layers grown at changing growth temperatures from 910 °C to 960 °C, b) the position and FWHM of A_1(LO) phonon line of $In_{1-x}Ga_xN$.

Table 3.16 Summary of the results obtained from XRD, AFM, OAS, and Raman spectroscopy analyzing $In_{1-x}Ga_xN$ layers with a nominal set value of x = 0.6, as a function of growth temperature.

	Growth temperature	910°C	925°C	940°C	960°C
XRD (0002)	2-θ (in deg)	33.36	33.31	33.38	33.56
	FWHM (arcsec)	2160	1210	1510	2110
	Estimated composition x	0.64	0.61	0.64	0.70
OAS	Absorption edge (eV)	2.2	1.9	2.3	2.6
AFM	Surface roughness (nm)	8.5	5.7	8.6	10.3
	Ave. grain area (10^{-2} μm^2)	1.5	0.9	1.8	2.2
RAMAN	Low energy side position (cm^{-1})	666	644	656	658
	Low energy side FWHM (cm^{-1})	60	43	49	47
	High energy side position (cm^{-1})	688	682	685	693
	High energy side FWHM (cm^{-1})	33	38	32	34

The XRD analysis suggests that – under the set of chosen growth conditions - at the growth temperature of 925°C the highest amount of indium was incorporated in the $In_{1-x}Ga_xN$ (x=0.61) epilayers. Smaller and high growth temperatures led the less indium incorporation and reduced structural quality. The XRD (0002) Bragg reflex from the $In_{1-x}Ga_xN$ layer grown at 925°C showed an optimum, but is at least a factor 3 to 5 too high for device quality material. The same $In_{1-x}Ga_xN$ layer, showed the lowest optical absorption edge, the smoothest surface roughness and the smallest average grain area. The A_1 (LO) phonon line in Raman spectra had to be fitted using two contributions, which could be due either a two phonon mode behavior or due

to microscopic compositional fluctuations that are not observable in XRD spectra. The low energy side A_1 (LO) peak contribution was the sharpest at 925 °C, indicating strain relaxation while the higher energy side peak was the broadest. The results from Raman analysis are in good agreement with those reported by Hernandez et al.[202] in which the higher indium incorporation shifted the LO phonons to lower energies, while the spectral line-shape is broadened. Further studies in a wider range of growth temperatures and reactor pressures are needed to improve the phase stability and structural quality in this composition regime.

Conclusions

We have studied the compositional variations in single-phase $In_{1-x}Ga_xN$ (x=0.6) epilayers grown by HPCVD in the temperature range of 910°C - 960°C. XRD analysis revealed single phase epilayers with a local structural optimum at growth temperature of 925°C, which coincide with the smoothest surface morphology and the smallest average grain area as analyzed by AFM analysis. The line shape analysis of the A_1 (LO) phonon mode observed in Raman spectroscopy indicates the highest strain component for a growth temperature of 925°C, at which the indium incorporation was closest to the set molor group III ratio in the gas phase.

Chapter 4

4. Summary and conclusions

Atomic Force Microscopy (AFM) has been used to study the nano-scale surface morphological properties of the neural growth cones, and InGaN semiconductor epilayers.

The neural growth cones:

We investigated the surface morphology of neural growth cones of identified neurons from the buccal ganglion of the pond snail Helisoma trivolvis using AFM. While AFM studies have been performed on a variety of growth cones from other species, this is, to the best of our knowledge, the first report detailing the nano-scale structure of growth cones of Helisoma neurons B5 and B19. The evaluation of PCM with AFM images provides a method to link internal properties of growth cones to their structure. In addition to providing high-resolution topographical information on two types of growth cones, we describe in detail the two-dimensional (height and width) tapering of B19 and B5 filopodia. The tapering mechanisms in B5 and B19 filopodia was observed to be function of $(filopodium\ length)^{-1/2}$ and $(filopodium\ length)^{-1}$, respectively. The volumetric analysis of filopodium revealed that relatively low number of Ca^{2+} ions would be sufficient to exhibit up to 10 fold increase in the free Ca^{2+} concentration. Furthermore, this increase in the concentration is different for B5 and B19 filopodia. The here presented surface morphological studies on filopodium provide a basis for future modeling studies of Ca^{2+} signaling events in filopodia and their growth cones.

The InN and InGaN semiconductor materials

The surface topography of InGaN epilayers has been studied by AFM. The results are correlated with the characterization data obtained by XRD, Raman, IR and PARS in order to gain a better understanding on how the various growth processing parameters influence the physical properties of the grown InN and InGaN epilayers.

The correlation between surface roughness and InN XRD (0002) Bragg reflection has shown that there is a linear dependence between the surface roughness and the FWHM of the InN (0002) Bragg reflex, suggesting a direct correlation between the disturbance in crystalline quality and the surface roughening. InN epilayers grown on GaN/Sapphire (0001) templates have shown a higher surface roughness than epilayers grown on Sapphire (0001). The correlation between the average grain area and FWHM of (0002) Bragg reflection indicates that InN layers grown on GaN/Sapphire (0001) templates move in the decomposition-regime earlier than InN layers grown on Sapphire (0001) templates.

The correlation between surface roughness and the InN Raman E_2(high) vibrational mode showed that InN layers grown on GaN/Sapphire (0001) have better localized crystalline micro-structures than those grown on Sapphire (0001) templates. When a partial decomposition (etching) during growth was observed, the etch process decreased the average grain areas of the layer grown on GaN/Sapphire (0001) templates more than those grown on Sapphire (0001) substrates. The effects of decomposition on the InN layer were also observed in the real-time LLS traces as an increase in the scattering intensity. InN layers grown on Sapphire (0001) substrate and GaN/Sapphire (0001 templates grew epitaxial single phase. However, the onset of material decomposition was observed earlier for InN on Sapphire (0001) than for InN on

GaN/Sapphire (0001). XRD studies revealed that InN layers grown on GaN/Sapphire (0001) templates had better (0002) lattice plane crystalline arrangement.

The studies on the growth modes of InN layers showed that InN layers grown on GaN/Sapphire (0001) templates at temperatures of the lower heater at 800 °C and the upper heater at constant 820 °C revealed 2D-like growth mode. As the lower heater is decreased to 800°C and upper heater was lowered from 820°C to 800°C, the growth mode shifted to Stranski-Krastanov mode[76] in which the growth started 2D; however, it advanced towards 3D in terms of hexagonal columns. The temperature settings where the columnar InN growth was observed were the transition region for InN growth modes. As the lower and the upper heater temperatures were kept constant at 800 °C and 820 °C, respectively, the growth processes promoted 3D growth resulting in large hexagonal pyramids. The set points around 800°C provided the lowest surface adatom mobility, limiting the lateral growth to a minimum and resulting in the growth of hexagonal columns in vertical dimension. Any temperature gradient approach between these temperature settings can be used to adjust the geometry of these structures such as, transition from hexagonal columns to hexagonal pyramids. Depending on the direction and the range of the temperature gradients, embedded or free-standing nanostructures might be engineered.

The investigation of the coalescence behavior of InN revealed that surface roughness was the largest at about 40 nm for InN layers grown on GaN/Sapphire (0001) templates. Further film growth resulted in decreased surface roughness.

The characterization results from the InN nucleation studies on GaN/Sapphire (0001) templates and Sapphire (0001) substrates indicate that a small molar group V-III ratio during the nucleation period improves the nucleation on both types of the growth templates. The results

provide useful information for the development of self organized InN nanostructures with tailored nano-scale morphology.

The effect of the NH_3 exposure time on the surface morphological and the structural properties of InN layers showed that the average steady-state growth rate increased almost linearly with the increased NH_3 pulse injection time. This indicates that at the end of the each cycle sequence, indium fragments on the growth surface are carried over to the next injection cycle, leading to the buildup of an indium adlayer on the growth surface. For a NH_3 pulse injection time, of 2500 ms, the average steady-state growth rate was about half a monolayer per cycle. With increasing NH_3 pulse injection time, the surface roughness decreased and the average grain area increased. The local crystalline quality, analyzed by Raman spectroscopy, showed that the Raman E_2(high) mode improved for extended NH_3 pulse injection times. The A_1(LO) phonon mode did not show a significant dependence to the variation of the NH_3 pulse injection time. Although there was a slight dependence of this phonon line shifting downward, there was no clear correlation to extract due to the A_1(LO) phonon-plasmon coupling which needs further investigations. Simulations on the line-shape of the A_1(LO) phonon mode showed that the A_1(LO) line broadening provides an estimate on the free electron concentration in the InN layers, which can be cross-verified with IR-reflectance analysis results.

The lattice strain effect on the crystalline quality of the InN layers for different substrate templates has been investigated by analyzing the E_2(high) phonon line position. Since the lattice mismatch between InN and Sapphire is larger compared to lattice mismatch between InN and GaN, the E_2(high) phonon line position is higher for InN on GaN/Sapphire (0001) compared to InN on Sapphire (0001), indicated a smaller crystal strain component in InN layers grown on GaN/Sapphire (0001).

Analyzing the effects of the gallium incorporation in the $In_{1-x}Ga_xN$ layers on the surface morphology showed that the surface roughness increases linearly with increasing gallium content. The surface morphological analysis also indicates that the surface roughness increases with the increasing group V/III molar ratio. The increase in surface roughness with increasing group V-III molar ratio was higher in the layers grown on Sapphire (0001) templates. The free carrier concentration analysis of the $In_{1-x}Ga_xN$ layers with x larger than 0.35 showed reduced free carrier concentrations, a phenomenon not understood at present. The IR reflectance analysis showed that the free carrier concentration increases with increasing V/III molar ratio from 700 to 3000, a phenomenon thought to be related to the increased hydrogen amount present at the growth surface and/or the increased amount of grain boundaries. XRD analysis revealed single phase $In_{1-x}Ga_xN$ (x=0.6) epilayers with a local structural optimum at a growth temperature of 925°C, which coincides with the growth temperature that gave the smoothest surface morphology and the smallest average grain area as analyzed by AFM. The line shape analysis of the A_1(LO) phonon mode observed in Raman spectroscopy indicates the highest strain component at 925°C.

REFERENCES

[1] Kater, S. B. and V. Rehder, Curr. Opin. in Neurobiology 5(1): 68-74, (1995).

[2] S. Bradbury, P.J. Evennett, *Contrast Techniques in Light Microscopy,* (BIOS Scientific Publishers Limited, (1996).

[3] N. C. Santos, M. A. R. B. Castanho, Biophysical Chemistry, 107, 133–149, (2004).

[4] G. Kaupp, Atomic Force Microscopy, *Scanning Nearfield Optical Microscopy and Nanoscratching,* (Springer, 2006).

[5] S.A.C. Gould, B. Drake, C.B. Prater, A.L. Weisenhorn, S. Manne, H.G. Hansma, P.K. Hansma, J. Masse, M. Longmire, V. Elings, B. Dixon Northern, B. Mukergee, C.M. Peterson, W. Stoeckenius, T.R. Albrecht, and C.M. Quate, J. Vac. Sci. Techn. A8, 386 (1990).

[6] J.H. Hoh and P.K. Hansma, Trends in Cell Biology 2, 208 (1992).

[7] F. Zernike, Physica 9 (7), 686-698 (1942).

[8] B. Herman, *Flourescence Microscopy,* (Springer Verlag, 1998).

[9] Binnig, G., C. F. Quate, et al., Phys. Rev. Lett. 56(9) 930, (1986).

[10] K. Goslin, E. Birgbauer, G. Banker, and F. Solomon, The J.of Cell Biol., 109, 1621-163, (1989)

[11] T. Williamson, P. R. Gordon-Weeks, M. Schachner, and J. Taylor, Proc. Natl. Acad. Sci. USA, 93, 15221–15226, (1996)

[12] A. W. Schaefer, N. Kabir, and P. Forscher, The J.of Cell Biol., 158, 139–152, (2002).

[13] S. Nakamura, M. Senoh, S-I. Nagahama, N. Iwasa, T. Yamada,T. Matsushita, H. Kiyoku, Y. Sugimoto, Jap. J. of Appl. Phys. 35, L74 (1996).

[14] O. Jani, I. Ferguson, C. Honsberg, S. Kurtz, Appl. Phys. Lett. 91(13), pp. 132117-3 (2007).

[15] J. Wu, W. Walukiewicz, K. M. Yu, W. Shan, J. W. Ager III, E. E. Haller, H. Lu, W. J. Schaff, W. K. Metzger, S. Kurtz, J. Appl. Phys. 94(10), pp. 6477-6482 (2003).

[16] R. Dahal, B. Pantha, J. Li, J. Y. Lin, H. X. Jiang, Appl. Phys. Lett. 94(6), pp. 063505-3 (2009).

[17] H. Morkoc, *Nitride semiconductors and devices*, Springer-Verlag, (1999).

[18] T. Matsuoka, H. Okamoto, M. Nakao, H. Harima, E. Kurimoto, Appl. Phys. Lett. 81(7), pp. 1246-1248. (2002).

[19] J. Wu, W. Walukiewicz, K. M. Yu, J. W. Ager III, E. E. Haller, H. Lu, W. J. Schaff, Y. Saito, Y. Nanishi, Appl. Phys. Lett. 80(21), pp. 3967-3969, (2002).

[20] F.K. Yam, Z. Hassan, Superlatt. and Microstr., 43 1–23, (2008).

[21] http://rredc.nrel.gov/solar/spectra/am1.5/

[22] S. Yu. Karpov, MRS Internet J. Nitride Semicond. Res. 3, 16, (1998).

[23] I. Ho, G.B. Stringfellow, Appl. Phys. Lett. 69, 2701-2703, (1996).

[24] R. Singh, D. Doppalapudi, T. D. Moustakas, and L. T. Romano, Appl. Phys. Lett. 70, 1089, (1997)

[25] B. N. Pantha, J. Li, J. Y. Lin, and H. X. Jiang, Appl. Phys. Lett. 93, 182107 (2008)

[26] N. A. El-Masry, E. L. Piner, S. X. Liu, and S. M. Bedair, Appl. Phys. Lett. 72, 40 (1998).

[27] C.A. Chang, C. F. Shin, N. C. Chen, T. Y. Lin, and K. S. Liu, Appl. Phys. Lett. 85, 6131, (2004)

[28] K. Kushi, H. Sasamoto, D. Sugihara, S. Nakamura, A. Kikuchi and K. Kishino, Mater. Sci. Eng. B,59 (1999).

[29] W. Van der Stricht, I. Moerman, P. Demeester, L. Considine, E.J. Thrush and J.A. Crawley, MRS Internet J. Nitride Semicond. Res. 2 (1997).

[30] T. Inushima, V. V. Mamutin, V. A. Vekshin, et al, J. of Crys. Grow. 227-228 pp. 481-485 (2001)

[31] J. Wu, W. Walukiewicz, W. Shan, et al, Physical Review B 66 pp. 201403 (2002)

[32] R. A. Oliver, C. Norenberg, M. G. Martin, et al, Surf. Sci. 532-535 pp. 806-810 (2003)

[33] J. Aderhold, V. Y. Davydov, F. Fedler, et al, J. of Crys. Grow. 222 pp. 701-705 (2001)

[34] Z. X. Bi, R. Zhang, Z. L. Xie, et al, Materials Letters 58 pp. 3641-3644. (2004)

[35] J. McChesney, P. M. Bridenbaugh, and P. B. O'Connor, Mater. Res. Bull. 5, 783, (1970).

[36] N. Dietz, in "*III-Nitrides Semiconductor Materials*", Ed. Z.C. Feng, Imperial College Press, ISBN 1-86094-636-4, pp. 203-235 (2006).

[37] John A. Venables, *Introduction to Surface and Thin Film Processes*, (Cambridge University Press, 2000).

[38] F. Bechstedt,*Principles of Surface Physics*, (Springer, 2003).

[39] L. de Broglie, Ph.D. Thesis (Paris), (1924).

[40] E.H. Synge, Phil. Mag. 6: 356, (1928).

[41] A. Lewis, M. Isaacson, A. Harootunian and A. Murray, Ultramicroscopy 13, 227 (1984).

[42] D.W. Pohl, W. Denk and M. Lanz, APL 44, 651 (1984)..

[43] Y. Oshikane, T. Kataoka, M. Okuda, S. Hara, H. Inoue, M. Nakano, Sci. Technol. Adv. Mater. 8: 181 (2007).

[44] G. Binnig, H. Rohrer, Ch. Gerber, and E. Weibel, Phys. Rev. Lett. 49, 57 - 61 (1982).

[45] A. Goswami, *Quantum Mechanics,* (Waveland Press, 2003).

[46] K. Oura, V. G. Lifshits, A. A. Saranin, A. V. Zotov, and M. Katayama, *Surface science: an introduction,* Springer-Verlag Berlin (2003)

[47] P. Dedecker, J. Hofkens and J. Hotta, Materialstoday, 11- 1, pp.12-21, (2008).

[48] Gould, S. A. C., B. Drake, et al., J. of Vacuum Sci. & Tech. A: Vacuum, Surfaces, and Films 8(1): 369-373, (1990).

[49] Fotiadis, D., S. Scheuring, et al., Micron 33(4) 385-397, (2002).

[50] Santos, N. C. and M. A. R. B. Castanho, Biophys. Chem. 107(2) 133-149, (2004).

[51] Gaczynska, M. and P. A. Osmulski, Curr. Opin. in Colloid & Interface Science 13(5) 351-367, (2008).

[52] Parpura, V., P. Haydon, et al., J. Cell. Sci. 104(2) 427-432, (1993).

[53] Tojima T., Hatakeyama D., et al. Jpn. J. Appl. Phys 37, 5, (1998).

[54] Tojima, T., Y. Yamane, et al., Neuroscience 101(2) 471-481, (2000).

[55] Melling, M., D. Karimian-Teherani, et al., NeuroImage 20(2) 795-801, (2003).

[56] Ricci, D., M. Grattarola, et al., Methods in Molec. Biol. 242: 15, (2004).

[57] McNally, H. A. and R. B. Borgens, J. of Neurocytology 33(2) 251-258, (2004).

[58] McNally, H. A., B. Rajwa, et al. J. of Neurosci. Methods 142(2) 177-184, (2005).

[59] Grzywa, E. L., A. C. Lee, et al. J. of Neurobiology 66(14) 1529-1543, (2006).

[60] Heredia, A., C. C. Bui, et al., NeuroImage 37(4) 1218-1226, (2007).

[61] Xiong, Y., A. C. Lee, et al., Biophys. Journal 96(12) 5060-5072, (2009).

[62] Kondra, S., J. Laishram, et al. J. of Neurosci. Methods 177(1) 94-107, (2009).

[63] Laishram, J., S. Kondra, et al. J.of Struct. Biol. DOI:10.1016/j.jsb.2009.09.005, (2009).

[64] H. Morkoc, *Nitride semiconductors and devices* (Springer-Verlag, 1999).

[65] O. Madelung, U. Rössler and M. Schulz, *Group IV Elements, IV-IV and III-V Compounds. Part b - Electronic, Transport, Optical and Other Properties* (Springer-Verlag, (2002).

[66] Flewitt, P. E. J. And Wild, R. K. *Grain Boundaries*, (Wiley, 2001).

[67] V. Y. Davydov, A. A. Klochikhin, R. P. Seisyan, V. V. Emtsev, S. V. Ivanov, F. Bechstedt, J. Furtmuller, H. Harina, A. V. Mudyri, J. Aderhold, O. Semchinova, and J. Graul, Phys. Status Solidi b **229** (2002).

[68] Y. Nanishi, Y. Saito, and T. Yamaguchi, J. Appl. Phys. **42,** 2549 (2003).

[69] M. Higashiwaki and T. Matsui, J. Cryst. Growth **162,** 269 (2004).

[70] Matsuoka, T., H. Okamoto, et al. Applied Physics Letters 81(7): 1246-1248 (2002).

[71] Wu, J., W. Walukiewicz, et al. Appl. Physics Letters 80(21): 3967-3969 (2002).

[72] T. L. Tansley and C. P. Foley, J. of Applied Physics 59, Issue 9, pp. 3241-3244 (1986).

[73] A. Wakahara, T. Tsuchiya, and A. Yoshida, Vacuum **41** (4-6), 1071-1073 (1990).

[74] K. S. A. Butcher and T. L. Tansley, Superlattices and Microstructures **38,** 1 (2005).

[75] A. G. Bhuiyan, A. Hashimoto, and A. Yamamoto, J. Appl. Phys. 94, 2779 (2003).

[76] V. Y. Davydov and A. A. Klochikhin, Semiconductors 38, 861 (2004).

[77] Z. Dridi, B. Bouhafs and P. Ruterana, Semicond. Sci. Technol. 18 9 850-856 (2003).

[78] R. Juza and H. Hahn, Z. Anorg. Alleg. Chem. **239,** 282 (1938).

[79] H. J. Hovel and J. J. Cuomo, Appl. Phys. Lett. **20,** 71 (1972).

[80] C. P. Foley and T. L. Tansley, Applications of Surface Science 22-23 (Part 2), 663-669 (1985).]

[81] T. L. Tansley and C. P. Foley, Electron. Lett. **20,** 1066 (1984).

[82] V. W. Chin, T. L. Tansley, and T. Osotchan, J. Appl. Phys. **75,** 7365 (1994).

[83] C. H. Swartz, R. P. Tomkins, T. H. Myers, H. Lu, and W. J. Schaff, Phys. stat. sol. (c) **2,** 2250-2253 (2005).

[84] P. A. Anderson, R. J. Kinsey, S. M. Durbin, A. Markwitz, V. J. Kennedy, A. Asadov, W. Gao, R. J. Reeves, J. of Appl. Phy. 98, 043903 (2005)

[85] R. Izaki, N. Kaiwa, M. Hoshino, T.Yaginuma, S. Yamaguchi, A. Yamamoto, Appl. Phys. Lett. 87, 243508 (2005).

[86] A. Ney, R. Rajaram, E. Arenholz, J.S. Harris Jr., M. Samant, R.F.C. Farrow, S.S.P. Parkin, J. of Mag. and Mag. Mat. 300 7–11 (2006)

[87] X.Wang, A. Yoshikawa, Prog.in Cry. Grow. and Charac. of Mat. 48/49 42-103 (2004)

[88] I. Mahboob, T. D. Veal, L. F. J. Piper, C. F. McConville, Hai Lu, W. J. Schaff, J. Furthmuller, F. Bechstedt, Phys. Rev. B 69, 201307 (R) (2004).

[89] T.D. Veal, L.F.J. Piper, W.J. Schaff, C.F. McConville, J. of Cry. Grow. 288 268–272 (2006)

[90] I. Mahboob, T.D. Veal, C.F. McConville, H. Lu and W.J. Schaff, *Phys. Rev. Lett.* **92** 036804 (2004)

[91] T. D. Veal, L. F. J. Piper, I. Mahboob, Hai Lu,W. J. Schaff, and C. F. McConville, Phys. stat. sol. (c) 2, No. 7, 2246–2249 (2005).

[92] L.F.J. Piper, T.D. Veal, I. Mahboob, C.F. McConville, H. Lu and W.J. Schaff, *Phys. Rev. B* **70** 115333 (2004)

[93] H. Lu, W. J. Schaff, L. F. Eastman, and C. E. Stutz, Appl. Phys. Lett. 82, 1736 (2003)

[94] C. Stampfl, C. G. Van de Walle, D. Vogel, P. Kruger, and J. Pollmann, Phys. Rev. B 61, R7846 - R7849 (2000)

[95] G. Pettinari, F. Masia, M. Capizzi, A. Polimeni, M. Losurdo, G. Bruno, T. H. Kim, S. Choi,A. Brown, V. Lebedev, V. Cimalla, O. Ambacher, Phys. Rev. B 77, 125207 (2008)

[96] S. N. Mohammad and H. Morkoc, Prog. Quantum Electron. **20,** 361 (1996).

[97] Tyagai, V.A., Evstigneev A.M., Krasiko A.N., Andreeva A.F., Malakhov V.Ya., *Sov. Phys. Semicond.* **11** (1977)

[98] Lambrecht, W.R., Segall B., Phys. Rev. B 47 9289-9296 (1993).

[99] Zubrilov A., *Properties of Advanced SemiconductorMaterials GaN, AlN, InN, BN, SiC, SiGe* . 49-66, (John Wiley & Sons, 2001).

[100] Tansley, T.L. in *Properties of Groupe III Nitrides*, ed. Edgar J.H., INSPEC, London p.39 (1994).

[101] V. Cimalla, U. Kaiser, I. Cimalla, G. Ecke, J. Pezoldt, L. Spiess, O. Ambacher, H. Lub, W. Schaff, Superlatt. and Microstr. 36 487–495 (2004)

[102] Fritsch, D., Schmidt, H., Grundmann, M.: Phys. Rev. B 69 165204 (2004)

[103] P Schley, R Goldhahn, C Napierala, G Gobsch, J Schormann, D J As, K Lischka, M Feneberg and K Thonke, Semicond. Sci. Technol. 23 055001 (2008)

[104] A. Kasic, E. Valcheva, B. Monemar, H. Lu, and W. J. Schaff, Phys. Rev. B 70, 115217 (2004).

[105] I. Akasaki and H. Amano, *Jpn. J. Appl. Phys.* **36**: 5393-5408, (1997)

[106] A. A. Klochikhin, V. Y. Davydov, V. V. Emtsev, A. V. Sakharov, V. A. Kapitonov, B. A. Andreev, H. Lu, and W. J. Schaff, Phys. Rev. B. **71,** 195207 (2005).

[107] H. Lu, W. J. Schaff, and L. F. Eastman, in *Mater. Res. Soc. Symp. Proc.*; *Vol. 9* (2002), p. 693.

[108] S. C. Jain, M. Willander, J. Narayan, and R. V. Overstraeten, J. Appl. Phys. **87,** 965 (2000).

[109] V. Y. Davydov and A. A. Klochikhin, Semiconductors **38,** 861-898 (2004).

[110] V. Bougrov, M.E. Levinshtein, S.L. Rumyantsev, A. Zubrilov, *Properties of Advanced SemiconductorMaterials GaN, AlN, InN, BN, SiC, SiGe* . Eds. M.E. Levinshtein, Rumyantsev S.L., Shur M.S., John Wiley & Sons, Inc., New York, (2001)

[111] M. Suzuki, T. Uenoyama, A. Yanase, Phys. Rev. B 52, 11 8132-8139 (1995)

[112] H.P. Maruska and J.J. Teitjen, Appl. Phys. Lett. 15-367 (1969)

[113] H. Amano, M.Kito, K. Hiramatsu, I Akasaki, *Jpn. J. Appl. Phys.* **28**: 2112 (1989)

[114] Nakamura, S., M. Senoh, et al. Jap. J. of Appl. Phys. 35 (Part 2, No. 1B): L74 (1996)

[115] Jani, O., Ferguson I., et al. Appl. Phys. Lett. 91(13): 132117-3 (2007).

[116] Wu, J., W. Walukiewicz, et al., J. of Appl. Phys. 94(10): 6477-6482 (2003).

[117] Dahal, R., B. Pantha, et al., Appl. Phys. Lett. 94(6): 063505-3 (2009).

[118] T. Inushima, V. V. Mamutin, V. A. Vekshin, et al, J. of Crys. Grow. **227-228** pp. 481-485 (2001)

[119] J. Wu, W. Walukiewicz, W. Shan, et al, Physical Review B **66** pp. 201403 (2002)

[120] R. A. Oliver, C. Norenberg, M. G. Martin, et al, Surf. Sci. **532-535** pp. 806-810 (2003)

[121] J. Aderhold, V. Y. Davydov, F. Fedler, et al, J. of Crys. Grow. **222** pp. 701-705 (2001)

[122] Z. X. Bi, R. Zhang, Z. L. Xie, et al, Materials Letters **58** pp. 3641-3644. (2004)

[123] S. Nakamura, Diam. Relat. Mater. 5 496 (1996).

[124] X.Q. Shen, T. Ide, M. Shimizu, H. Okumura, J. Cryst. Growth 237–239 1148 (2002).

[125] S. Mahajan and K. S. S. Harsha, *Principles of growth and processing of semiconductors,* (WCB/McGraw-Hill, 1998).

[126] I. Ho and G. B. Stringfellow, Appl. Phys. Lett. 69, 2701 (1996)

[127] S. Y. Karpov, MRS Inter. J. Nitride Semicond. Res. 3, 16 (1998).

[128] J. Adhikari and D. A. Kofke, J. Appl. Phys. 95, 4500 (2004).

[129] B. N. Pantha, J. Li, J. Y. Lin, and H. X. Jiang, Appl. Phys. Lett. 93, 182107 (2008)

[130] N. A. El-Masry, E. L. Piner, S. X. Liu, and S. M. Bedair, Appl. Phys. Lett. 72, 40 (1998).

[131] K.S.A. Butcher, M. Winttrebert-Fouquet, P.P.-T. Chen, T.L. Tansley, H. Dou, S.K. Shrestha, H. Timmers, M. Kuball, K.E. Prince and K.E. Bradby, *J. Appl. Phys.* **95** p. 6124. (2004).

[132] Q.X. Guo, T. Tanaka, M. Nishio, H. Ogawa, X.D. Pu and W.Z. Shen, *Appl. Phys. Lett.* **86** p. 231913 (2005).

[133] D. C. Look, J. R. Sizelove, J. Jasinski, Z. Liliental-Weber, K. Saarinen, S. S. Park, and J. H. Han, in *Mater. Res. Soc. Symp. Proc.*, (2003), p. 575-590.

[134] Z. C. Feng, *III-Nitride Semiconductor Materials* (Imperial College Press, 2006).

[135] O. Igarashi, Jpn. J. App. Phys. **31,** 2665-2668 (1992).

[136] N. Takahashi, J. Ogasawara, and A. Koukitu, Jpn. J. App. Phys. **172,** 298-302 (1997).

[137] N. Takahashi, R. Matsumoto, A. Koukitu, and H. Seki, Jpn. J. App. Phys. **36,** L743-L745 (1997).

[138] O. Ambacher, J. Phys. D: Appl. Phys **31,** 2653-2710 (1998).

[139] Z. G. Qian, W. Z. Shena, H. Ogawa, and Q. X. Guo, Journal of Applied Physics **92,** 3683-3687 (2002).

[140] S. Zhoua, M.F. Wua, S.D. Yaoa, J.P. Liub and H. Yangb, Superlatt. and Microstruct. 39, (2006).

[141] N. Dietz, V. Woods, S. McCall, and K. J. Bachmann, in *Proc. Microgravity Conf.*, 2002, p. 169-181.

[142] N. Dietz, in *III-Nitrides Semiconductor Materials*, edited by Z. C. Feng (Imperial College Press, 2006), p. 203-255.

[143] M. C. Johnson, K. Poochinda, N. L. Ricker, J. W. Rogers, and T. P. Pearsall, J. Cryst.

[144] J. McChesney, P. M. Bridenbaugh, and P. B. O'Connor, Mater. Res. Bull. **5,** 783 (1970).

[145] N. Dietz, M. Strassburg, and V. Woods, J. Vac. Sci. Technol. A 23, 1221(2005)

[146] M. Alevli, G. Durkaya, W. Fenwick, A. Weerasekara, V. Woods, I. T. Ferguson, A. G. U. Perera, and N. Dietz, Appl. Phys. Lett. 89, 112119 (2006)

[147] M. Alevli et al., Mater. Res. Soc. Symp. Proc. 955E, 1 (2007).

[148] N. Dietz, V. Woods, S. McCall, and K. J. Bachmann, Proc. of the Microgr. Conf., NASA/CP-2003–212339 pp. 169–181 (2003)

[149] B. H. Cardelino, C. E. Moore, C. A. Cardelino, and N. Dietz, Proc. SPIE 5912, 86 (2005)

[150] B. H. Cardelino, C. E. Moore, C. A. Cardelino, S. McCall, D. O. Frazier, and K. J. Bachmann, J. Phys. Chemistry **A107,** 3708-3718 (2003).

[151] V. T. Woods, PhD. Thesis, Atlanta (2006).

[152] G. A. Hebner, K. P. Killeen, and R. M. Biefeld, J. Cryst. Growth **98(3),** 293-301 (1989).

[153] J. Senawiratne, PhD. Thesis, Atlanta (2006).

[154] F. H. Pollak: In: Analytical Raman Spectroscopy, edited by J. G. Grasselli, B. J. Bulkin p 137. (Wiley, New York 1991)

[155] Hernandez, S., R. Cusco, et al. Journal of Applied Physics 98(1): 013511-5. (2005).

[156] F. Demangeot, C. Pinquier, J. Frandon, M. Gaio, O. Briot, B. Maleyre, S. Ruffenach, and B. Gil, Phys. Rev. B **71,** pp.104305-11 (2005).

[157] N. D. Mermin, Phys. Rev. B **1,** 2362 (1970).

[158] J. Linhard and K. Dan, Vidensk. Selsk. Mat. Fys. Medd. **28,** 881 (1954).

[159] A. B. Weerasekara, PhD. Thesis, Atlanta (2007).

[160] M. V. Klein and T. E. Furtac, *Optics* (Wiley, NY, 1986).

[161] C. C. Katsidis and D. I. Siapkas, Appl. Optics **41,** 3978 (2002).

[162] M. Alevli, PhD thesis, Atlanta (2008)

[163] http://www.unipress.waw.pl/fityk/

[167] X.L. Zhu, L.W. Guo, N.S. Yu, J.F. Yan, M.Z. Peng, J. Zhang, H.Q. Jia, H. Chen and J.M. Zhou, J. of Cryst. Grow. 306,292–296 (2007)

[168] H. Morkoc, B. Sverdlov, G. B. Gao, Proc. IEEE 81, 493, (1993)

[169] K. M. Asif, M. S. Shur, G. Simin, Phys. Stat. Sol. A, 155, (2003)

[170] Zhang R. Q., Liu X. L., Kang T. T., Hu W. G., Yang S. Y., Jiao C. M., ZHU Q. S. Chin. Phys. Lett., 25-1, 238, (2008)

[171] C. Meissner, S. Ploch, M. Pristovsek, M. Kneissl, Phys. Stat. Sol. C, 6-S2, 545, (2009)

[172] M.C. Johnson, S.L. Konsek, A. Zettl, E.D. Bourret-Courchesne, Journal of Crystal Growth 272, 400–406, (2004)

[172] F. H. Yang, J. S. Hwang, Y. J. Yang, K. H. Chen and J. H. Wang, Jpn. J. Appl. Phys. Vol. 41, L 1321, (2002)

[173] Y. F. Ng, Y. G. Cao, M. H. Xie, X. L. Wang, and S. Y. Tong, Appl. Phys. Lett **81**, 21 (2002).

[174] F. Bechstedt, *Principles of Surface Physics.* (Springer, 2003).

[175] Y. Huang, H. Wang, Q. Sun, J. Chen, D.Y. Li, J.C. Zhang, J.F. Wang, Y.T. Wang and H. Yang, J. of Crys. Grow. 293. 269, (2006)

[176] Z. X. Bi, R. Zhang, Z. L. Xie, X. Q. Xiu, Y. D. Ye, B. Liu, S. L. Gu, B. Shen, Y. Shi, Y. D. Zheng, J. Mater. Sci. 42:6377–6381, (2007)

[177] H. Wang, L. L. Wang, X. Sun, J. H. Zhu, W. B. Liu, D. S. Jiang, J. J. Zhu, D. G. Zhao, Z. S. Liu, Y. T. Wang, S. M. Zhang and H. Yang, Semicond. Sci. Technol. 24 075004 (2009)

[154 -178] V. Lebedev, V. Cimalla, F.M. Morales, J.G. Lozano, D. González, Ch. Mauder and O. Ambacher, J. of Crys, Grow, 300 50–56 (2007)

[179] B. Lewis and J. C. Anderson, *Nucleation and Growth of thin films,* (Academic Press, 1978).

[180] B. B. Varga, Phys. Rev. **137,** A1896 (1965).

[181] A. Mooradian and G. B. Wright, Phys. Rev. Lett. **16**, 999 (1966).

[182] E. Burstein, A. Pinczuk, and S. Iwasa, Phys. Rev. **157**, 611 (1967).

[183] P. Perlin, J. Camassel, W. Knap, T. Taliercio, J. C. Chervin, T. Suski, I. Grzrgory, and S. Porowski, Appl. Phys. Lett. **67**, 2524 (1995).

[184] M. Ramsteiner, O. Brandt, and K. H. Ploog, Phys. Rev. B **58**, 1118 (1998).

[185] J. S. Thakur, D. Haddad, V. M. Naik, R. Naik, G. W. Auner, H. Lu, and W. J. Schaff Phys. Rev. B **71**, 115203 (2005).

[186] R. Collazo, S. Mita, R. Schlesser, and Z. Sitar, Phys. Status Solidi C 2, 2117 (2005)

[187] M. Alevli, G. Durkaya, R. Kirste, A. Weesekara, A.G.U. Perera, W. Fenwick, V. T. Woods, I. T. Ferguson, A. Hoffmann, and N. Dietz, Mater. Res. Soc. Symp. Proc. Vol. 955-I08-04, (2007)

[188] S. Nakamura, M. Senoh, S-I. Nagahama, N. Iwasa, T. Yama-da, T. Matsushita, H. Kiyoku, Y. Sugimoto, Jap. J. of Appl. Phys. 35, L74 (1996).

[189] A. Janotti, and C. G. V. de Walle, Appl. Phys. Lett. 92(3), pp. 032104-3 (2008).

[190] V. Darakchieva, N.P. Barradas, M.-Y. Xie, K. Lorenz, E. Alves, M. Schubert, P.O.A. Persson, F. Giuliani, F. Munnik, C.L. Hsiao, L.W. Tu, W.J. Schaff, Physica B 404(22) pp.4476-4481 (2009).

[191] G. Pettinari, F. Masia, M. Capizzi, A. Polimeni, M. Losurdo, G. Bruno, T. H. Kim, S. Choi, A. Brown, V. Lebedev, V. Cimalla, O. Ambacher, Phys. Rev. B (Cond. Matt.and Mat. Phys.) 77(12), pp. 125207-6 (2008)

[192] S. Ruffenach, M. Moret, O. Briot, B. Gil, Appl. Phys. Lett. 95(4), pp. 042102-3 (2009)

[193] K. Kurihara, T. Yanagawa, N. Nakagawa, K.Fukui, A. Ya-mamoto, Inf. Phys. & Tech. 51, pp. 482-3 (2008).

[194] M. Schubert, T. E. Tiwald, C. M. Herzinger, Phys. Rev. B, 61(12), pp. 8187-14, (2000).

[195] S.-Y. Kwon, M.-H. Cho, P. Moon, H. J. Kim, H. Na, H.-C. Seo, H. J. Kim, Y. Shin, D. W. Moon, Y. Sun, Y.-H. Cho, E. Yoon, Phys. Stat. Sol. (a) 201, pp. 2818-2822 (2004).

[196] H. Wang, D. S. Jiang, L. L. Wang, X. Sun, W. B. Liu, D. G. Zhao, J. J. Zhu, Z. S. Liu, Y. T. Wang, S. M. Zhang, and H. Yang, J. Phys. D: Appl. Phys., 41, 135403, (2008).

[197] D. A. G. Bruggeman, Ann. Phys. (Leipzig) 24, 636 (1936).

[198] R. Singh, D. Doppalapudi, T. D. Moustakas, and L. T. Romano, Appl. Phys. Lett. 70, 1089 (1997)

[199] C.A. Chang, C. F. Shin, N. C. Chen, T. Y. Lin, and K. S. Liu, Appl. Phys. Lett. 85, 6131, (2004)

[200] K. Kushi, H. Sasamoto, D. Sugihara, S. Nakamura, A. Kikuchi and K. Kishino, Mater. Sci. Eng. B, 59 (1999).

[201] W. Van der Stricht, I. Moerman, P. Demeester, L. Considine, E.J. Thrush and J.A. Crawley, MRS Internet J. Nitride Semicond. Res. 2 (1997).

[202] S. Hernández, R. Cuscó, D. Pastor, L. Artús, K. P. O'Donnell, R. W. Martin, I. M. Watson, Y. Nanishi, and E. Calleja. J. of Appl. Phys. 97 013511 (2005).